

Thesis for the Degree of Doctor of Philosophy

Mechanical Characterization of Protein Materials at Multiple Spatial Scales

Advisor : Professor Sungsoo Na

by

Gwonchan Yoon

Thesis submitted in partial fulfillment of requirements
for the Degree of Doctor of Philosophy

Department of Mechanical Engineering
Graduate School of the Korea University

February, 2012

© 2012 Gwonchan Yoon

Mechanical Characterization of Protein Materials at Multiple Spatial Scales

Gwonchan Yoon

Department of Mechanical Engineering, Korea University
Anam-Dong, Seoungbuk-Gu, Seoul, 136-713, Korea

Thesis advisor : Professor Sungsoo Na

Abstract

Proteins are designed to perform mechanical functions for maintain the life of livings, and it can be possible to design the biomaterials through mimicking the protein function. Moreover, the protein causes some fatal disease when the proteins are mis-produced in the phenomenological condition, so it is important to understand the protein's function, which is related to the structure and property of proteins. Recently the characterization methods help to investigate the structure-property relation of proteins in the multiple length scale form atomic to macro scale, and it can help to understand diverse functions of proteins. In this dissertation, the state-of-art of the characterization methodology for biomaterial is introduced, and the structure-property-function relationship of the protein materials is investigated in multiple hierarchical structures of proteins such as single bond, protein domain, and protein fibrils. Furthermore, diverse *in silico* characterization methodologies are suggested which are proper to each hierarchy of protein materials. It is believed that the result from mechanics-based studies about the protein materials in this dissertation can positively inspire engineers who participate to the interdisciplinary fields.

To my Lord, Jesus Christ

Contents

Abstract	i
Contents	iii
List of Figures	vi
List of Tables.....	x
Chapter 1. Introduction	1
1.1. Backgrounds	1
1.1.1. Mechanical Functions of Proteins.....	1
1.1.2. Protein-Based Biomimetic Materials.....	6
1.1.3. Role of Protein Mechanics on Disease Expression.....	11
1.1.4. Structure-Property-Function Relation	15
1.2. Mechanical Characterization of Protein Materials.....	20
1.2.1. Experimental Techniques.....	20
1.2.1.A. Atomic Force Microscopy (AFM) Experiments	20
1.2.1.B. Optical Tweezers Experiments	25
1.2.1.C. Micro/Nano-Indentation Experiments	27
1.2.2 Computational Techniques.....	29
1.2.2.A. Molecular Dynamic Simulations.....	29
1.2.2.B. Steered Molecular Dynamic Simulation.....	34
1.2.2.C. Normal Mode Analysis	35
1.2.2.D. Coarse-Grained (CG) Modeling and Simulations	37
1.3. Structure of Dissertation	39
Chapter 2. Characterization of Bond Rupture Mechanics	41
2.1. Introduction	41
2.2. Theory and Methods	45
2.2.1. Theory: Kramer's Theorem	45
2.2.1.A. Bell's Model: Conventional Bond Rupture Model	45

2.2.1.B. Bond Rupture Model: Kramers Theory	46
2.2.1.C. Mechanical Rupture of Chemical Bond Described by Linear-Cubic Potential Using Kramers Theory	48
2.2.2. Numerical Method: Brownian dynamics	51
2.3. Results	52
2.3.1. Theoretical Predictions on the Role of Loading Device in the Bond Rupture Mechanism	52
2.3.2. Brownian Dynamics Simulations on Bond Ruptures: Loading-Device Stiffness vs. Rupture Forces	55
2.3.3. Comparison of the theoretical model with others	58
2.4. Summary	60

Chapter 3. Mechanical Behavior of Secondary Structure of Proteins 61

3.1. Introduction	61
3.2. Method: Gō Model	62
3.3. Results: Unfolding Mechanics	63
3.3.1. Case Study I: α -helix and β -hairpin	63
3.3.2. Case Study II: Ubiquitin	70
3.3.3. Anisotropic Unfolding Mechanics.....	73
3.4. Summary	76

Chapter 4. Mechanical Properties of Protein Crystals 77

4.1. Introduction	77
4.2. Methods	78
4.2.1. Micromechanics model	78
4.2.2. Inter-atomic potential	80
4.3. Results.....	80
4.3.1. Elastic Properties of Protein Crystals	81
4.3.2. Role of Folding Topology in Mechanical Properties of Protein Crystals	85

4.4. Summary	88
Chapter 5. Mechanical Characterization of Disease-Related Protein Fibers.....	89
5.1. Introduction	89
5.2. Theory and Methods	91
5.2.1. Continuum Mechanics Model.....	91
5.2.1.A. Euler-Bernoulli Beam Model.....	91
5.2.1.B. Timoshenko Beam Model.....	94
5.2.2. Coarse-Grained Model.....	95
5.2.2.A. Structure Model of Protein Fibers	95
5.2.2.B. Elastic Network Model.....	96
5.3. Results.....	97
5.3.1. Vibration Characteristic of Protein Fibrils	97
5.3.2. Mechanical Properties of Protein Fibrils.....	99
5.3.3. Bending Vs. Torsion	102
5.3.4 Effect of Polymorphism in Mechanical Properties	104
5.3.5. Geometric Effects on Mechanical Properties: Role of Twisted Structure	106
5.4. Discussion: Limitation of the Model	108
5.5. Summary	108
Chapter 6. Conclusion	110
References	112

List of Figures

Fig. 1.1. The β -crystallite of spider silk protein.(PDB ID: 2slk, generated by Visual Molecular Dynamics (VMD)). The hydrogen bond is colored as magenta.

Fig. 1.2. (A) Hierarchical structure of muscle fiber. (B) Molecular structure Ig domain of titin (PDB ID : 1tit, 89 residues) which is generated by VMD.

Fig. 1.3. (A) The Structural hierarchy of amyloid fibrils. (B) The Bottom-up approach for fabrication of biomimetic materials. (C) Bio-film (left) and nanowire (middle) made by amyloid fibrils and titin-mimicking artificial elastomeric proteins (right).

Fig. 1.4. Eight class of steric zipper.

Fig. 1.5. (A) The mechanical properties of materials in conventional materials science. (B) The structure-property relationship of materials including biomaterials.

Fig. 1.6. (A) Cartoon of single molecule force spectroscopy. (B) Force-extension curve of titin Ig domain fitted with WLC model.

Fig. 1.7. The optical tweezers experiment. (A) The unbinding/binding experiment between two protein using optical tweezers. (B) Force-extension curve by the experiment.

Fig. 1.8. The simulaton technology in the various hierarchical structure with the time scale and length scale.

Fig. 1.9. Internal coordinates for bonded interactions of covalent bond, bond angle, dihedral angle (from up to down).

Fig. 1.10 (A) The unfolding trajectory of titin Ig domain. (a, extension 10 Å; b, 17 Å; c, 150 Å; d, 285 Å) (B) The unfolding force-displacement curve for unfolding of titin Ig domain. (I, preburst; II, major burst; III, post burst; IV, fully extended)

Fig. 1.11. The illustration of coarse-grained modeling method in the hierarchical structure of protein.

Fig. 2.1 (a) Dimensionless free energy landscape with mechanical perturbation by a loading device with different stiffness. Inset shows the free energy barriers with respect to dimensionless pulling rates $\bar{\lambda}$ and the dimensionless stiffness ε of loading device. (b) Normalized kinetic rate \bar{k} for bond rupture as a function of dimensionless pulling rate and the dimensionless stiffness of loading device. Here, the dimensionless temperature is given as $\bar{T} = 0.105$. (c) Probability distributions of bond rupture forces with respect to the stiffness sL of a loading device. Here, the model parameters are described in the text. (d) Mean rupture forces as a function of loading rate as well as the stiffness of a loading device.

Fig. 2.2 (a) Force exerted by a loading device (with loading rate of $\dot{F} = 1 \text{ nN/s}$) is shown with respect to stiffness of loading device. (b) Probability distributions of bond rupture forces are presented as a function of loading rate and the stiffness of a loading device. (c) Mean bond rupture forces with respect to stiffness of loading device and loading rate. Here, solid line shows the fitting to the theoretical model.

Fig. 2.3 Comparison between kinetic rates for bond ruptures predicted by our theoretical model, Hummer-Szabo model, and Freund's model as a function of the stiffness of a loading device: (a) $s_L = 0.1 \text{ N/m}$, and (b) $s_L = 1 \text{ N/m}$.

Fig. 3.1. The Cartoon of α -helix (A) and β -hairpin (B) which is generated by Visual Molecular Dynamics (VMD).

Fig 3.2. (A) The force-extension curve obtained by constant velocity pulling simulation. (B) The displacement-time curve obtained by constant force pulling simulation.

Fig. 3.3 (A) The force-extension curve of β -hairpin obtained by constant velocity pulling condition with two kinds of loading device stiffness. (B) The unfolding

trajectory according the force-extension curve (The silver is $s_L = 0.05$ N/m, and the red is $s_L = 0.01$ N/m.).

Fig 3.4. The unfolding forces with respect to loading rate and stiffness of loading device for β -hairpin unfolding. Here, solid line indicates the fitting to the theoretical model.

Fig 3.5 (A) N to C pulling condition for unfolding simulation of ubiquitin. The blue is β_5 , red is β_1 , and yellow is β_3 (B) The unfolding force-displacement curve of ubiquitin

Fig 3.6 The unfolding pathway of ubiquitin corresponding to the force curve at Fig. 3.5 (B)

Fig 3.7 (A) 48 to C pulling condition for unfolding simulation of ubiquitin (B) The unfolding force-displacement curve of ubiquitin

Fig 3.8 The unfolding pathway of ubiquitin corresponding to the force curve at Fig. 3.7 (B)

Fig. 4.1. The hierarchical structure of protein fibril represented periodically repeated unitcell.

Fig. 4.2. The stress-strain relation of various protein crystals. Here, titin distal is distal Ig domain of titin, titin prox. is the proximal Ig domain of titin, TTR is transthyretin, and α -lac is α -lactalbumin.

Fig. 4.3. Relationship between Young's modulus of biological protein materials and degree-of-fold Q.

Fig. 4.4. Relationship between maximum hydrostatic stress of protein materials and degree-of-fold Q

Fig. 5.1. Four cases of cross- β hIAPP fibril.

Fig. 5.2. (a) Four fundamental deformation modes of hIAPP fibril when the cross- β structure is antiparallel/hetero and one pitch length. Soft bending, stiff bending, twisting and stretching mode from left. (b) The mode indices (left axis)

and natural frequencies (right axis) of the fibril.

Fig. 5.3. (a) Soft bending elastic modulus, stiff bending elastic modulus, torsional shear modulus and axial elastic modulus of the antiparallel hetero fibril varying fibril length (L) to 280 nm. (b) The bending rigidity of the fibril varying fibril length (L) (c) Mode index of soft bending, stiff bending, torsion and axial

Fig. 5.4. Twist/bend ratio of antiparellel hetero hIAPP fibril about fibril length.

Fig. 5.5. Mechanical properties of four cross- β configuration of the hIAPP fibril varying fibril length. (a) The soft bending elastic modulus (b) The stiff bending elastic modulus (c) The torsional shear modulus (d) The axial elastic modulus

Fig. 5.6. Soft and stiff bending rigidity of untwisted hIAPP fibril (Antiparallel hetero, $L = 17.045$ nm) about fibril length.

List of Tables

Table 4.1. Elastic property of protein crystals

Table 5.1. Comparison the elastic modulus among the result from different method.

Chapter 1. Introduction

1.1. Background

1.1.1. Mechanical Function of Protein

Proteins are designed to perform their mechanical function, which plays a critical role in biochemical processes in living objects ranging from cells, tissues, bones, and even to organs. Spiders can drag their body using dragline silk and are able to capture prey using vicid silk which absorbs the flying insect's kinetic energy when it impacts a spider web [1-3]. This indicates that the biological function of spider silk (*e.g.* capturing a prey) is attributed to the remarkable mechanical properties of spider silk. Specifically, it was found that the elastic modulus of spider silk is in the order of 10 GPa [1], and that the fracture toughness of spider silk excels that of an engineering material, even a composite material such as Kevlar [1]. For a last decade, it has been believed that the remarkable properties of spider silk may be ascribed to the molecular architecture of spider silk; spider silk is composed of amorphous chains and crystal-like β -sheets. The extreme extension of spider silk induced by abseiling of spider is due to the amorphous chain that can be elastically stretched. The high strength of a spider silk may be ascribed to crystal-like β -sheet that can bear the mechanical load without fracture [4]. Thus, in order to understand the mechanical function of a protein, it is essential to gain insights into a protein's structure-property relationship as has been already established in conventional engineering materials [5] (see also Section 1.1.4). In particular, recent experimental techniques such as X-ray crystallography and/or nuclear magnetic resonance (NMR) have allowed the visualization of the three-dimensional structure of a folded protein domain. Moreover, recent experimental tools such as atomic force microscopy (AFM) and/or optical tweezer have provided an

insight into the mechanical behavior of a folded protein in response to mechanical force (see Section 1.2.1). Recent studies have reported that the crystallites of a spider silk protein are formed of β -sheet structures, which is a ladder-like shape consisting of a unit structure called β -strand. This β -sheet structure is one of the elementary structures of mechanical proteins which can exert a mechanical loading in physiological condition as in muscle protein [6]. The origin of remarkable mechanical properties of β -crystallites is attributed to hydrogen bond acting as chemical glue between β -strands (Fig. 1.1), which has recently been highlighted in a recent study using atomistic simulation [7]. However, though experimental techniques have provided an insight into the mechanical behavior of a folded protein domain (at single-molecule level) and/or spider silk (at macroscopic scale) [4], it is still challenging to establish the structure-property relationship for protein materials at multiple length scales; it has been still remained elusive how the combination of secondary structures (e.g. β -strand, α -helic, loop, etc.) controls the mechanical properties of protein materials at various length scales.

Another excellent example of a mechanical protein is a giant muscle protein titin. A muscle is composed of the bundle of muscle fibers, called *sarcomere*, which consists of titin, actin, and myosin filament. In particular, titin connects the actin and myosin filament (Fig. 1.2. (A)). The biological function of muscle fiber (*i.e.* muscle contraction or relaxation) is closely related to the molecular architecture of a sarcomere. When muscle contracts and extends, the myosin filament moves along the actin filament, while the titin acts as a molecular spring to protect a muscle from overstretching in sarcomere [8]. The actin and myosin generate force through a power stroke mechanism by conformational change of myosin, which is hinge-like motion via binding to and/or detaching from actin filament. [9] In this moment, the motion of myosin looks like walking on the

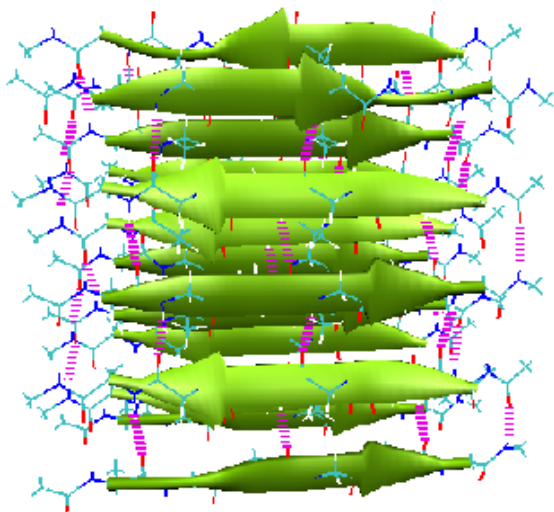


Fig. 1.1. The β -crystallite of spider silk protein.(PDB ID: 2slk, generated by Visual Molecular Dynamics [10] (VMD)). The hydrogen bond is colored as magenta.

actin filament through converting chemical energy into mechanical energy. A protein that converts chemical energy into mechanical motion is called motor protein. There are other types of motor proteins, *e.g.* kinesin and dynein which walk on microtubules [11]. Titin responsible for the elasticity of muscle, has a chain-like shape which connects multiple domains linearly [12]. There are mainly two kinds of domains in titin, the one is globular protein, *i.e.* immunoglobulin (Ig) domain, while the other is flexible segments, *i.e.* PEVK domain (rich in proline (P), glutamate (E), valine (V) and lysine (K), which are amino acid sequences among 20 kinds of different amino acids). When small pulling force is applied to titin, the structurally flexible PEVK segment is unraveled after straightening of the multiple Ig domains [8]. According to *in silico* single-molecule simulation, the pulling force is in the order of a few tens of pico-Newtons for arrangement of multiple Ig domains. When a force of ~100pN is applied to titin individual Ig domain, it starts to be unfolded, which has been found from AFM single-molecule experiments and/or *in silico* single-molecule simulations. The force-displacement curve of a titin, which is obtained from single-molecule experiments, resembles saw-tooth-like graph, where each peak in the force curve correspond to the force at which an individual Ig domain for a titin is unfolded [13,14]. The details of AFM single-molecule experiments are delineated later in Section 1.2.1.A. Titin Ig domain is mostly composed of β -strands, especially the parallel β -strands that are the origin of high strength for Ig domain (Fig 1.2. (B)). These special proteins are called elastomeric protein, which exhibits the excellent elastic properties, such as titin Ig domain, titin FnIII domain and ubiquitin [15]. As a conclusion, an individual Ig domains (secondary structure) buffer large forces, whereas multiple Ig domains (tertiary structure) and flexible PEVK region resist small forces when external force is applied to titin. So it is evident that the structure of the muscle protein titin is directly related to

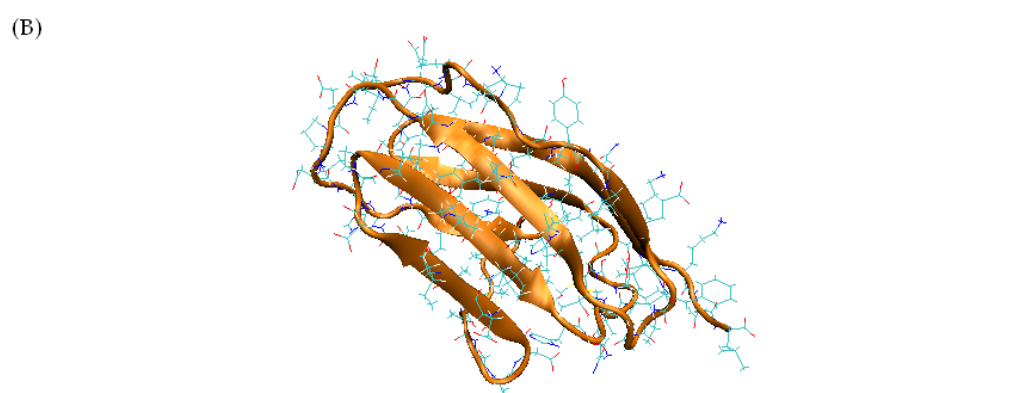
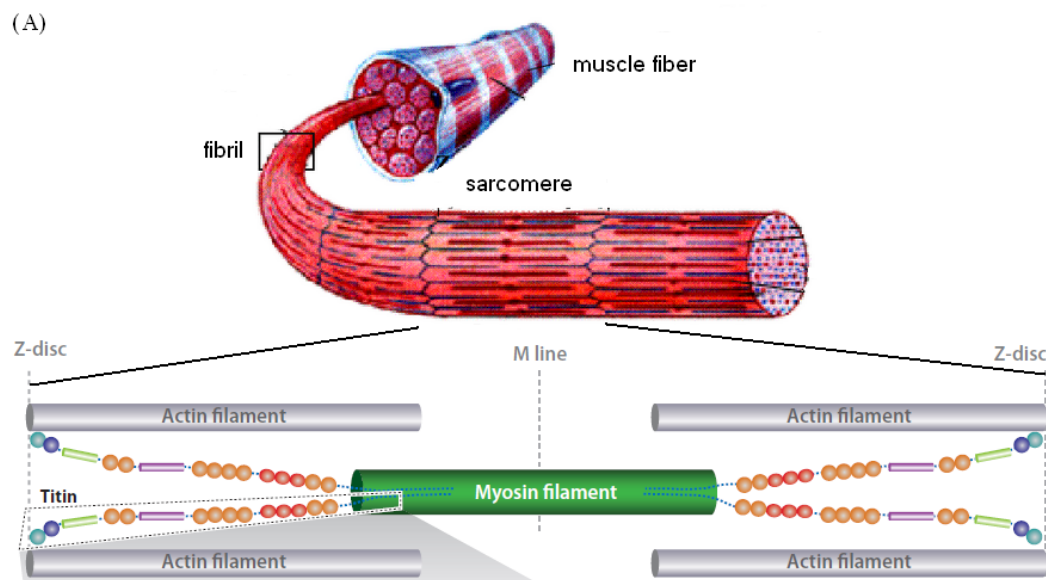


Fig. 1.2. (A) Hierarchical structure of muscle fiber. (B) Molecular structure Ig domain of titin (PDB ID : 1tit, 89 residues) which is generated by VMD [10].

its mechanical function.

Except two aforementioned proteins, there are many kinds of proteins that can perform mechanical function protein, which allows for maintaining the inner life of the cell [16]; for instance, these proteins are spectrin (scaffold to maintain cell shape [17,18]), tubulin (acting as a road for transportation biological substances [19]), and chaperonin (the barrel-shaped facility to make three-dimensional structure of protein [20]). In extracellular environment, selectin and integrin performs their biological function using mechanics; in particular, they help the leukocyte rolling and arresting on vascular surface [21]. Moreover, von Willebrand factor (VWF) is able to sense a shear stress change in blood stream at injury sites to induce blood clotting [22]. To the best of the author's knowledge, the experimental and computational observation of the mechanical function of various proteins, which governs the function of cells, are still at premature stage; it is still poorly understood how proteins can perform mechanical functions using chemical stimulus (*e.g.* pH change, temperature, ion concentrations, etc.). Moreover, structure-property relationship has not been well established for protein materials, while this relationship has played a significant role in materials science for engineering material design [5].

1.1.2. Protein-Based Biomimetic Materials

Several proteins possess the remarkable mechanical properties such as super-elasticity, high yield-strength, and high fracture toughness [13,23]. This may prompts researchers to develop a novel materials, with which one can replace an engineering material (*e.g.* composite), being able to perform anomalous functions; for instance, based on the insight into the mechanical function of spider silk (as described in Section 1.1.1), a spider silk-inspired material exhibits both super-extensibility (even up to 100% strain) and high yield strength and

fracture toughness (even higher than those of Kevlar). In general, these two contradictory properties (super-extensibility and high fracture toughness) cannot be achieved in a conventional engineering material such as steel. Specially, spider silk protein possesses the yield strength comparable to that of high-tensile steel and fracture toughness better than that of Kevlar, which may be useful in developing a *de novo* material that can be used for bulletproof jacket [24]. Recently, there is an effort that has been made to improve the mechanical properties of spider silk by adding inorganic impurities such as zinc (Zn), titanium (Ti), aluminum (Au) [25]. They have also proposed that to use inorganic impurities for improving the mechanical properties would be also useful for other biomaterials such as collagen membranes from avian eggs. But it is still challenging to synthesize bio-inspired materials at large scales (*e.g.* milli-meter scales) using information of bottom-up biological protein materials at nanoscales. Recently, in order to develop bio-inspired large-scale materials, researchers have attempted to mimic the mechanism of spinning techniques that spider use; secreted proteins pass through the tapering spinning duct of a spider, usually accompanied by changes in biochemical environment, extensional flow, and shear forces [26]. Furthermore, the molecular mechanism of spider silk formation from soluble protein suggests two models; the one is liquid crystal theory and the other is micelle theory. The liquid crystal theory demonstrates that soluble protein forms rod-like amphiphilic block copolymer to be aligned by β -sheet rich structure, while micelle theory describes that soluble protein forms sphere-shaped micelle [27].

Another excellent candidate for developing bio-inspired materials is amyloid fibrils due to their unanticipated excellent mechanical properties. These remarkable mechanical properties may be correlated to the molecular structures of amyloid fibrils; amyloid fibrils exhibit long and twisted β -sheet rich molecular

structure that is similar to β -crystallite of spider silk protein, which leads to the remarkable mechanical properties [28,29]. The amyloid fibrils are formed by denatured proteins that are found in the patients' organ of neurodegenerative diseases [30,31] such as Alzheimer's disease, Parkinson's disease and degenerative diseases as type II diabetes [32], cataract [33] and cardiomyopathy [34]. The amyloid fibrils are generally organized by β -strands that are oriented perpendicularly to the fibril axis, and connected through a dense hydrogen-bonding network, which results in supramolecular β -sheets [35,36] (Fig. 1.3.A). A recent experimental study has reported that the Young's modulus of various amyloid fibrils (*e.g.* A β , insulin, lysozyme, β -lactoglobulin, etc.) is in the order of tens of giga-pascal, which is comparable to that of spider dragline silk [37]. Especially, it has been found that the Alzheimer's A β amyloid fibrils exhibit the Young's modulus of \sim 30 GPa, which is predicted from atomic tensile simulation [38] and/or normal mode analysis [39]. The AFM nano-indentation experiment has been performed to obtain the elastic properties of β -lactoglobulin amyloid fibril; such an experiment has shown that the Young's modulus of β -lactoglobulin amyloid is in the order of 3.7 GPa, and that this property is dependent on the thickness of fibrils [40]. The β -lactoglobulin is helical fibril consisting of the twisting multi-stranded ribbons with the number of fibrils between 1 and 5. The more the number of fibrils, the higher the thickness and helical pitch of the fibrils [41]. Recently, due to the excellent mechanical properties of amyloids, there has been an effort to design and develop a thin film using self-assembly of amyloid fibrils (Fig. 1.3.B); this thin film exhibits the Young's modulus of 5 - 7 GPa, which is comparable to that of proteinaceous materials found in nature such as collagen, keratin, silk, and so forth [42]. The fabrication process is successive bottom-up approach, which uses characteristic of hierarchical protein structure; a protein monomer at angstrom scale composes

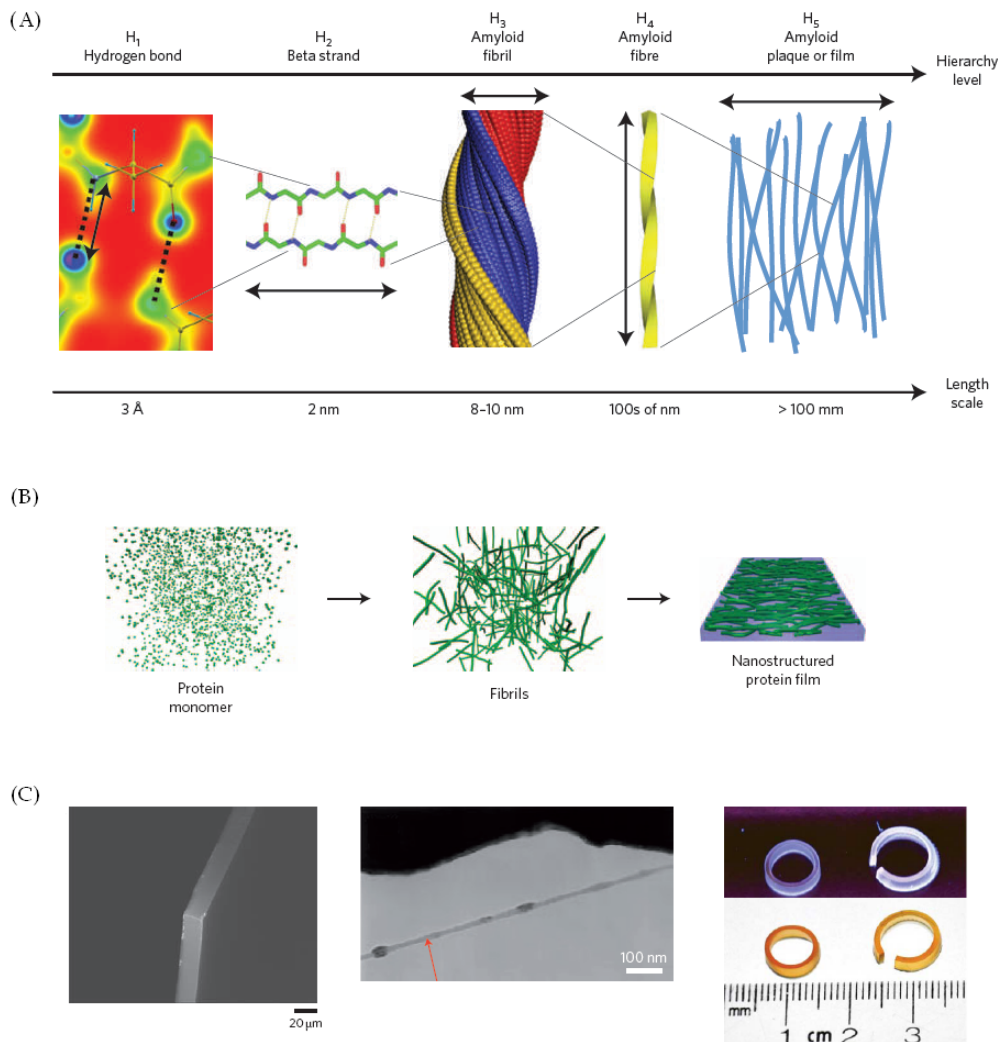


Fig. 1.3. (A) The Structural hierarchy of amyloid fibrils. (B) The Bottom-up approach for fabrication of biomimetic materials. (C) Bio-film (left) and nanowire (middle) made by amyloid fibrils and titin-mimicking artificial elastomeric proteins (right). Figure reproduced with permission from: (A), Ref. [35], © 2010 NPG; (B), ref. [43], © 2011 NPG; (C), ref. [44], © 2011 NPG and ref. [15], © 2010 NPG

lysozyme fibrils at nanoscale, and then they are stacked into films at mico-scales (Fig. 1.3.B). In addition, these amyloid-inspired materials may be useful for future applications in developing conducting nanowires, surface coatings, light-harvesting nanostructures, and hollow nanotubes that can act as nanoscale antenna (Fig. 1.3.C) [43].

Titin-mimicking artificial elastomeric protein (see Fig. 1.3.C) is produced for applications in tissue engineering as scaffold and matrix for artificial muscle that has mechanical properties such as softness (*e.g.* Young's modulus close to 100 kPa). In addition, the muscle has viscoelastic properties, which is an increase in energy dissipation due to tensile loading and stress relaxation at a constant strain [45]. Artificial protein materials are used for developing a biomimetic material, which mimics the passive elastic (viscoelastic) properties of a muscle; the one is GB1 domain mimicking folded titin immunoglobulin domain, whereas the other is random-coil-like protein resilin that imitates PEVK region of titin [15]. The nanoscale tensile characteristics obtained by AFM single-molecule experiment are sensitively dependent on to the manner of a combination of these two building blocks, which can provide a design principle to synthesize biomimetic materials at macroscopic scales. The Young's modulus of such a muscle-inspired materials is in the range of 50~70 kPa, which is comparable to that of a sarcomere in a physiological condition. Researchers [13] have provided the design principle, which describes that a resilin can bear the highest maximum strain without breaking under dynamic loading condition. In summary, an insight into the mechanical function of protein will be useful in underlying design principles for developing biomimetic or biologically inspired materials that can perform anomalous functions, which a conventional engineering material is unable to perform.

1.1.3. Role of Protein Mechanics on Disease Expression

Over a last decade, it has been observed that formation of unanticipated protein fibrils is ubiquitous in disease expressions such as Alzheimer's, Parkinson's, Huntington's, type II diabetes, and so forth [46]. In particular, the formation of a protein fibril (known as "amyloidosis") is attributed to several denatured proteins, which are a significant factor in neurodegenerative and degenerative disease expression, deposited on the normal organs and uncontrollably growing as plaques [28,30,47]. For instance, in the brain tissue of patients experiencing Alzheimer's disease, β -sheet filamentous structure aggregates due to self-assembly and self-propagation characteristics, and this filamentous structure is called $A\beta_{1-42}$ fibril [48]. Moreover, even though the amyloid fibril is formed based on stacking of a small secondary structure such as β -strand, researchers have found the diversities of the molecular structures of amyloid fibrils. For example, the $A\beta_{1-42}$ fibrils have found to exhibit two kinds of cross-sectional shapes; one is a rectangular shaped two-fold symmetry, while the other is a triangular shaped three-fold symmetry. Moreover, it has recently been reported [37] that amyloid fibrils can possess the excellent mechanical properties such that the elastic modulus of amyloid fibril is comparable to that (*i.e.* ~ 10 GPa) of stiff protein materials such as actin filament and/or spider silk. It has recently been suggested that the mechanical properties of protein materials (*e.g.* amyloid) are highly correlated with their biological functions such as disease expressions [49]. This indicates that it is *a priori* requisite to understand the mechanical properties of disease-related protein materials (*e.g.* amyloid) for further insights into their roles in disease expressions. Furthermore, since amyloid fibrils can have diverse conformations as described above, it is also necessary to study the effect of the conformational diversity of amyloids in their mechanical properties. It has been reported that the mechanical properties of amyloid fibrils are

significantly governed by the conformational diversity of amyloids [39]. Specifically, the normal mode analysis shows that the amyloid fibril possessing the three-fold symmetry exhibits the lower elastic modulus than that exhibiting two fold symmetry. There is one more example to demonstrate the conformational diversity and/or polymorphism of amyloid fibril; TTR₁₀₅₋₁₁₅ fibril, which is formed by the denatured transthyretin found in the heart of patients undergoing cardiomyopathy, has cross-section like four-folded symmetry [50]. It is still unclear how the amyloid fibril can be formed with different cross-sectional shape, and how this diverse shapes can affect the mechanical properties of amyloid fibrils and also their functions such as disease expressions.

In a recent decade, there are efforts that have been made to unveil the molecular structures of amyloid fibrils using various experimental techniques [51-53] and/or theoretical/computational techniques [43,54-56]. These efforts have shown that the conformational diversity of amyloid fibril can be sorted into the eight classes of steric zippers through different arrangement of β -strands in the supramolecular structure of peptide [55]. For instance, the molecular structures of hIAPP₂₀₋₂₉ (human islet amyloid polypeptide) fibril, which is the fibrillation core domain of fibrils in the pancreas of type II diabetes patients, have recently been found such that hIAPP₂₀₋₂₉ fibrils can exhibit two kinds of steric zipper conformations; (i) antiparallel hetero zipper, that is antiparallel configuration of β -strands along fibril axis and across to fibril axis [32], and (ii) parallel hetero zipper, that is parallel configuration of β -strands along fibril axis and accross to fibril axis [57]. There are more classes of steric zipper such as homo, side chain configuration of face-to-face between front and back ladder, and co-aligned/anti-aligned, up-up/up-down configuration between of front and back ladder, in Fig. 1.4 recent study has been directed towards the characterization of the 8 classes of steric zippers using enthalpy difference

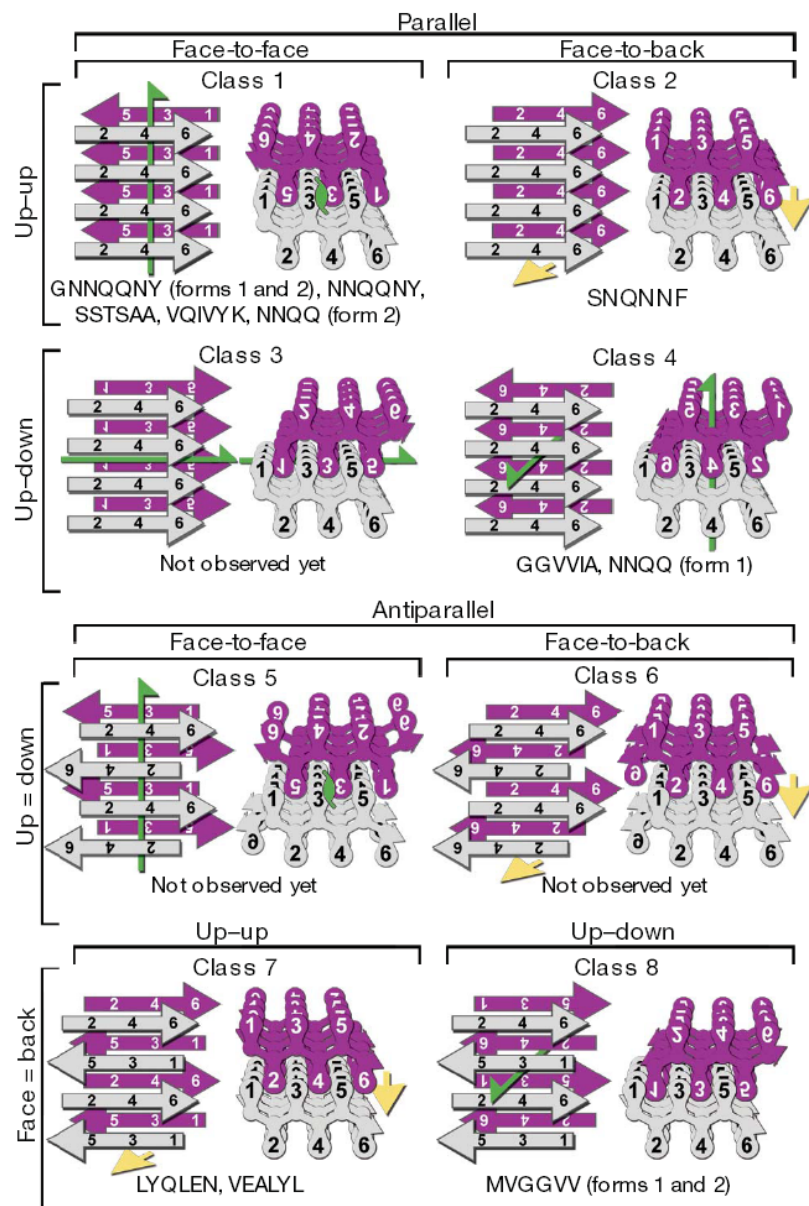


Fig. 1.4. Eight class of steric zipper. Figure reproduced with permission from Ref. [55], © 2007 NPG

between different polymorphic forms of GNNQQNY (that is amino acid sequence of a β -strand of amyloid fibril) calculation by molecular dynamic (MD) simulation [58]. After 25 ns heating at 300K, the amyloid fibril is twisted with different helical pitches that 157 Å at parallel configuration and 174 Å at antiparallel one. They found that the origin of these structural differences between parallel and antiparallel configurations is attributed to the number of hydrogen bond difference and the electrostatic potentials difference at the inner surfaces of the steric zippers. Moreover, they found that the importance of the amino acid sequence in the polymorphism whether they hold stable structure or not [59]. For example, GNNQQYY is stable when it has parallel homo co-aligned and SSTSAA is stable at antiparallel hetero anti-alligned. Despite recent attempts to characterize the molecular structures of amyloid fibrils, it is still unclear how the conformational diversity of amyloid fibrils is correlated with their mechanical properties and related biological functions.

Mechanical characterization has played a crucial role in the diagnosis of diseases and/or development of novel therapeutics [49]. For instance, the measurement of elastic modulus has recently been used as a signature that is useful in separation of cancerous cells from normal cells, which implies an early diagnosis of cancers. In this sense, it is reported that the tumor cells taken from the body fluids of patients with suspected lung, breast, and pancreas cancer are softer than normal cells. [60] In other cases, The HCC (hepatocellular carcinoma cells), which are the most common type of liver cancer, exhibit greater stiffness when compared with normal hepatocytes [61]. Moreover, the effect of lamin mutation in progeria can affect to the mechanical property of the nucleus such that the progeria nucleus can be fractured under large mechanical loading, whereas the healthy nucleus is just deformed under same loading condition. These cases illustrate that the measuring mechanical properties can offer an

opportunity to detect disease expressions even at early stage. Furthermore, understanding the structure-property-function relationship of the protein in disease expression could bring a new paradigm in drug design. Over a last decade, computer-based *de novo* drug design has been introduced to overcome long development time and high cost of conventional drug design method [62]. Because of the limitation of existing chemical compounds and increasing new diseases due to change of environment [63], the bottom-up drug design has recently been highlighted against traditional “Top-down” approaches [64]. Top-down approaches often involve less efficient physiology-based approach, but bottom-up strategy is a target-based paradigm; it is based on the molecular structural information of protein as well as the mechanical properties of proteins, where such mechanical properties are generally encoded in the molecular structure of a protein. This bottom up approach is also called molecular therapeutics. The typical example of product from *de novo* drug design is Gleevec developed by Novartis [65], which has been used to cure and treat chronic myeloid leukemia (CML). In the case of Alzheimer’s disease, the molecular therapeutic strategies for protein misfolding and aggregation have recently been considered using a molecular agent that serves as stabilizer of normal protein folding, β -sheet breakers, and so forth [46]. In summary, we believe that mechanical characterization of various disease-related proteins, sub-cellular materials (*e.g.* cytoskeleton, microtubule, lamin, etc.), and cells would play a leading role in developing a *de novo* molecular therapeutics and/or early diagnostics.

1.1.4. Structure-Property-Function Relation

The fundamental understanding of structure-property-function relationship has been pursued and played a central role in materials science. In particular, a

priori knowledge of structure-property-function relationship has provided the insight into how to optimally design the structure that can perform the desirable functions. For instance, since the emergence of *micromechanics* theory [66] in 1980s, there is an effort that has been made to establish theoretical framework that suggests the relationship between microstructure and macroscopic behavior for various materials. This effort has endowed an idea of how to tailor the macroscopic behavior (*e.g.* elastic, plastic, and fracture behaviors) of various materials [5,67] such as metals, ceramics, glass, polymers, and even cellular solids through controlling the microstructure of materials. As an example, Hall and Petch studied how the microstructure governs the fracture behavior of a material. The relationship between microstructure and fracture behavior for a material was renowned as “Hall-Petch” relationship, and it is very useful in designing a material’s microstructure for its desired mechanical performance. Specifically, the Hall-Petch relation delineates a relation between the yield strength (σ_y) and the grain size for a material, and such relation is represented in the form $\sigma_y \propto 1/\sqrt{d}$, where σ_y is the yield strength of a material, and d is the grain size of a material. The useful structure-property-function relation in material design can be rigorously utilized in design of engineering material such as metal alloys. The fracture toughness of Ni-Al alloy can be tailored by manipulating an alloy’s grain boundaries that are typically affected by amount of Ni, quenching temperature, or cooling temperature.

As described above, the structure-property-function relationship has played a central role in material design for decades. The detailed picture of such a relationship is provided in Fig. 1.5.A, which presents the properties of various materials, particularly the density and elastic modulus of various materials. Here, the density of a material is highly correlated with the microstructure of a material, so that the density can be regarded as a parameter that represents the structure.

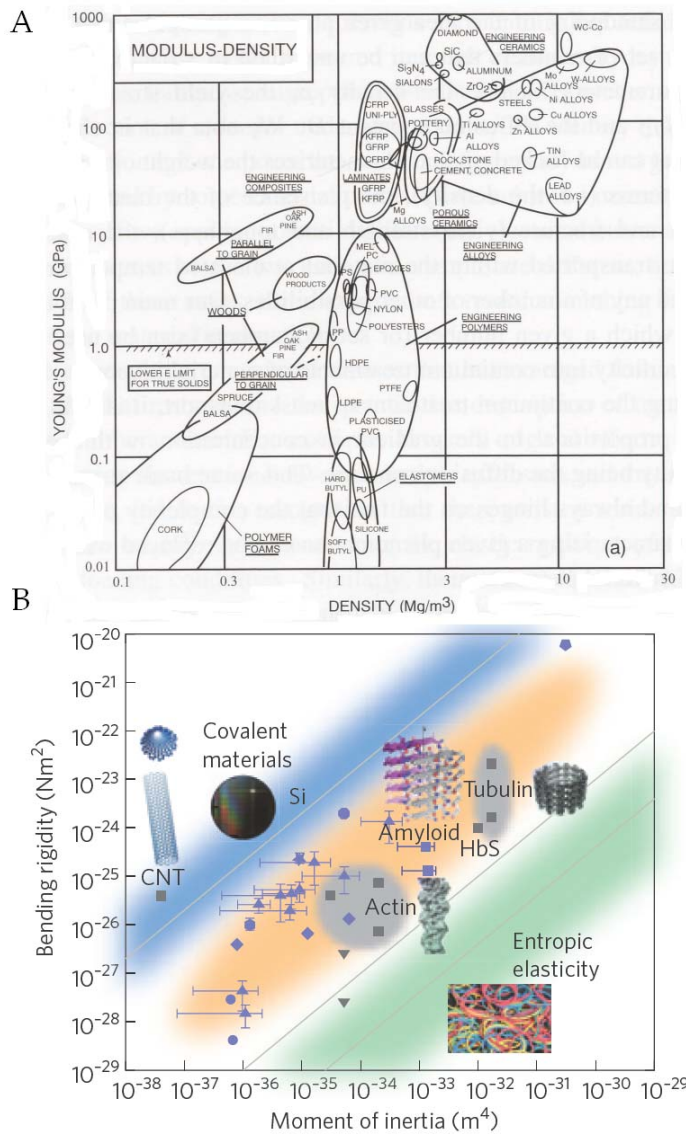


Fig. 1.5. (A) The mechanical properties of materials in conventional materials science. (B) The structure-property relationship of materials including biomaterials. Figure (B) reproduced with permission from ref. [43], © 2011 NPG

The relationship between density (representing the microstructure) and elastic modulus (property) as shown in Fig. 1.5.A provides the fundamental principles of how to utilize a material for designing an engineering structure that can bear the mechanical load as designed for its functions. For instance, if one uses polymer for development of engineering structure, polymer's density related to the structure of polymer is in the range of 1 to 2 Mg/m³, and it exhibits the elastic modulus of 0.1 – 10 GPa. In a recent decade, there has been attempted to construct the structure-property-function relationship for nanoscale materials such as carbon nanotubes, protein materials, and polymer chains in order to provide an insight into how to design nanoscale engineering structures for their own purposed functions. Among various nanoscale materials, the most popular nanomaterial is a one-dimensional material (*e.g.* carbon nanotube or protein filament) that can be chemically synthesized or found in nature. For one-dimensional material, a cross-sectional shape that is a representative parameter for the structure of one-dimensional nanomaterial, may determine the mechanical (*i.e.* bending) behavior of such nanomaterial. As shown in Fig. 1.5. (B), it is easily noted that protein filaments exhibit a relationship between moment of inertia and bending modulus, which is very different from that for carbon nanotubes and any other one-dimensional nanomaterials such as silicon nanowires. The significant differences in structure-property relationship between protein filaments and carbon nanotubes are attributed to the different atomic structures, particularly different types of inter-atomic interactions that determine the mechanical properties. Specifically, the mechanical behavior of protein materials is originated from the extension (and fracture) of non-covalent bonds such as hydrogen bonds and/or hydrophobic cores. On the other hand, the mechanical behavior of carbon nanotubes is ascribed to the extension (and fracture) of covalent bonds such as carbon-carbon bonds. Here, the non-covalent

bonds do not play any role in the mechanical behavior of carbon nanotubes. This indicates that the atomic structural feature determines the mechanical behavior of nanomaterials as is similar to conventional structure-property relationships, which demonstrates that the micromechanical structure governs the mechanical behavior of materials. Despite recent efforts, it is still lacking in generic structure-property-function relationship for various nanoscale materials ranging from one-dimensional nanomaterials (*e.g.* carbon nanotubes, metal nanowires, and/or metal nanotubes), two-dimensional nanomaterials (*e.g.* graphene sheets, metal nanosheets), to three-dimensional nanomaterials (*e.g.* fullerene). We believe that there will be significant efforts that would be made to develop the structure-property-function relationship of generic nanomaterials for engineering purposes such as biomimetic design.

1.2. Mechanical Characterization of Protein Materials

As described earlier, it is essential to characterize the mechanical behavior of protein materials in order to understand how they can perform the biological functions through the mechanical deformation (*e.g.* force-driven unfolding of folded domain) of proteins. Mechanical characterization of protein materials has recently been available due to the recent experimental and computational techniques that can probe the mechanical response of protein materials to a mechanical load. This Section is dedicated to the demonstration of currently available techniques that allow for mechanical characterization of biological materials such as proteins, DNA, RNA, and even sub-cellular materials such as viral capsids.

1.2.1. Experimental Techniques

Among various experimental techniques that are able to probe the mechanical behavior of biological materials, we would like to focus in experimental characterizations based on atomic force microscopy (AFM) and/or optical tweezers. In particular, we have presented the single-molecule force spectroscopy experiments, which enable the mechanical characterization of single biomolecules such as proteins, RNA, and DNA, based on AFM or optical tweezer. Furthermore, we have overviewed the AFM nanindentation that provides the detailed information of the elastic properties of biological materials.

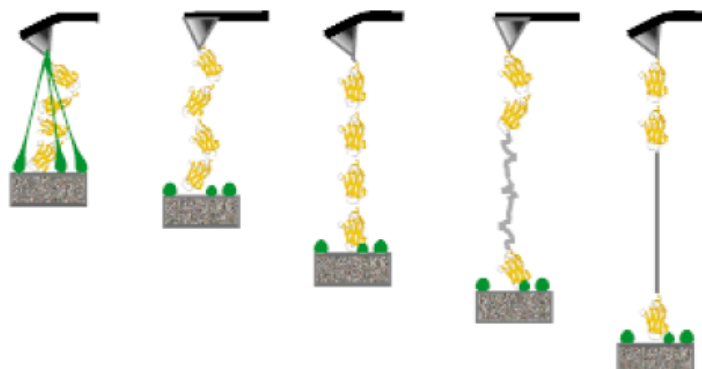
1.2.1. A. Atomic force microscopy (AFM) experiments

AFM was first developed in order to probe the characteristic of surface at nanoscale resolution using the interaction between tip and the surface [68]. In 1990s, AFM has been taken into account for probing the mechanical stretching of

a biomolecule [69-72] such as DNA, RNA, and proteins. In particular, as shown in Fig. 1.6.A, an end of a biomolecule is covalently bonded to an AFM tip while the other end is covalently linked to a substrate. When the substrate is moved with a constant velocity, the biomolecule starts to be stretched; the force acting on a biomolecule due to the mechanical extension is measured from the optical apparatus that estimates a cantilever's bending deflection, which can be converted into the amount of force using Hooke's law. This AFM-based single-molecule mechanics has allowed the fundamental insight into the elasticity of biomolecules such as DNA. It was shown that the elastic behavior of DNA molecule is well dictated by entropic elasticity [73-75], which was widely used theory in polymer physics [76,77]. Over the last decade, there is an effort that has recently been made to induce the unfolding of a protein domain using a mechanical force [13,14,78] for gaining insight into protein folding [79,80]. The force-extension profile is obtained by pulling serially connected protein domains (see Fig. 1.6.B). In particular, when serially connected protein domains are stretched with a constant velocity, the force-displacement curve for such protein domains resemble the saw-tooth pattern, where the force peaks are believed to be force that is required to induce the unfolding of each protein domain. Before the unfolding of a protein domain occurs, the force-displacement curve is well fitted to *worm like chain (WLC) model*, which was widely utilized to analyze the entropic elasticity of polymer molecules including DNA. WLC model presents the force-displacement relationship for a polymer chain in the form [81]

$$F(x) = \frac{k_B T}{b} \left[\frac{1}{4} \left(1 - \frac{x}{L} \right)^{-2} - \frac{1}{4} + \frac{x}{L} \right], \quad (1.1)$$

A



B

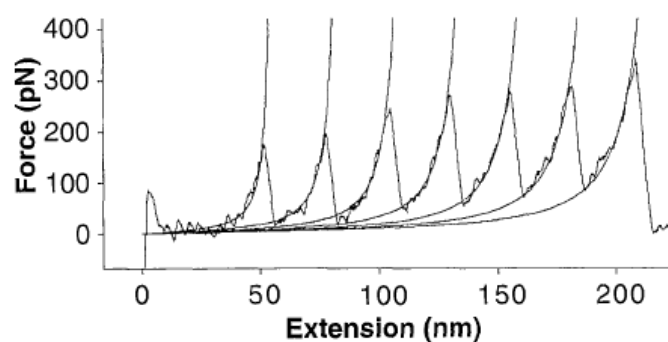


Fig. 1.6. (A) Cartoon of single molecule force spectroscopy. (B) Force-extension curve of titin Ig domain fitted with WLC model. Figure reproduced with permission from: (A), Ref. [78], © 2000 NPG; (B), ref. [13], ,© 1997 AAAS

where F is a force, x is an extension, k_B is Boltzmann's constant, T is an absolute temperature, b is the persistence length and L is contour length of a polymer chain, respectively. When the WLC model is fitted to a force-extension curve for titin Ig domain (Fig 1.6. B), the contour length of titin Ig domain is obtained to 28–29 nm, which is consistent with the length (*i.e.* 30 nm) of a fully extended polypeptide chain that consists of 89 amino acids [13].

For fundamental understanding of the biological functions (or malfunctions) of a protein, it is *a priori* requisite to develop a theoretical framework that presents the insights into protein folding processes, because the folded structure of a protein is highly correlated with its functions. The folding process is the change of random coil of amino acid sequences to the folded three-dimensional structure like the restoration to its original shape of the deformed shape memory alloy. Moreover, proteins are assembled from amino acids at a very high rate. For example, *E. coli* cells can make a complete, biological active protein molecule containing 100 amino acid residues in about 5 seconds at 37 °C [82]. It is impossible to find all possible conformations of the protein such rapidly, it can be estimated that proteins folds by a stepwise process. Therefore, there are partially folded structures, it is often referred to as a molten globule, of protein with folded and unfolded protein in the folding process, and the pulling experiment and simulation of protein can show the existence of molten globule and the relation of the structure and free energy of the molten globules. Also, the folding process of protein is reversible, that is, the unfolded state of protein can be restored to the folded state when pulling force is reduced [13].

To the best of our knowledge, protein folding process is not fully understood but it is conjectured that protein folding processes are critically dependent on a rugged free energy landscape, which determines the chemical reactions. This suggests that if one is able to probe the free energy landscape, then it may be

possible to predict the protein folding processes. Hence, it is significant to establish theoretical frameworks that probe the free energy landscape. In a last decade, there has been an attempt [79,80,83] to unveil the free energy landscape using AFM single-molecule force spectroscopy. The fundamental principle of the mechanical probe of the free energy landscape is based on Kramers' transition theory [84-86]. Kramers' transition theory demonstrates that the kinetic rate for a chemical transition between two states (*e.g.* folded and unfolded states) is determined by a one-dimensional free energy profile, which is dictated by two parameters such as energy barrier (denoted as E_b) and the distance between two states (denoted as x_b). In particular, the kinetic rate v is represented in the form [84,87,88]

$$v = \omega_0 \exp\left(-\frac{E_b - Fx_b}{k_B T}\right), \quad (1.2)$$

where v is a kinetic rate for chemical transition, ω_0 is the natural frequency of a folded state, F is a mechanical force applied to a protein domain, k_B is the Boltzmann constant, and T is an absolute temperature.

Based on Kramers' transition theory depicted in Eq. (1.2), the mean unfolding force is linearly proportional to the logarithm of pulling velocity. The fitting of mean unfolding force vs. pulling speed to the Kramers' transition theory allows for quantitatively probing a one-dimensional free energy landscape related to protein folding. For instance, AFM single-molecule mechanics of titin Ig domain with Kramers' transition theory provides a free energy landscape related to the folding of titin Ig domain such that the energy barrier E_b is measured as 2 - 4 kcal/mol, and that the barrier width x_b is estimated as $x_b = 0.3$ nm [13], which are comparable to the result of chemical unfolding experiments [89]. In addition,

AFM single-molecule experiment is also able to probe the effect of genetic mutation in Ig domain on the free energy landscape related to the folding of Ig domain [90,91]. Furthermore, AFM single-molecule experiments has provided the existence of the intermediate states of Ig domain by observing a “hump” in a force-extension curve, which implies the possibility in multiple pathways for protein folding process [92].

AFM single-molecule experiments have also envisaged the anisotropic mechanical properties of a protein domain. For instance, a recent study [93] has revealed that the mechanical response of a ubiquitin domain in response to a force applied in the direction of a vector connecting N and C termini is different from that in response to a force acting in different direction. When the ubiquitin is extended by stretching N-C termini, the unfolding force is 203 ± 35 pN. On the other hand, when the ubiquitin is mechanically stretched in the direction of a vector connecting a residue 48 and C terminus, the unfolding force is measured as 85 ± 20 pN. This indicates that the unfolding pathway of ubiquitin is dependent on the loading direction, which implies that there may be many accessible pathways for protein folding processes. In other words, the protein folding process is not purely determined by a one-dimensional free energy landscape as described above, but the insight into protein folding may be gained when a multi-dimensional free energy landscape [94] is taken into account.

1.2.1. B. Optical Tweezers Experiments

Even though AFM single-molecule experiments have allowed for understanding the mechanical behavior of biomolecules related to their biological functions, laser optical tweezer (LOT) has recently been also taken into account due to their ability to access the mechanics of biomolecules in different time scales [95]. In particular, LOT has envisaged the mechanical stretching of

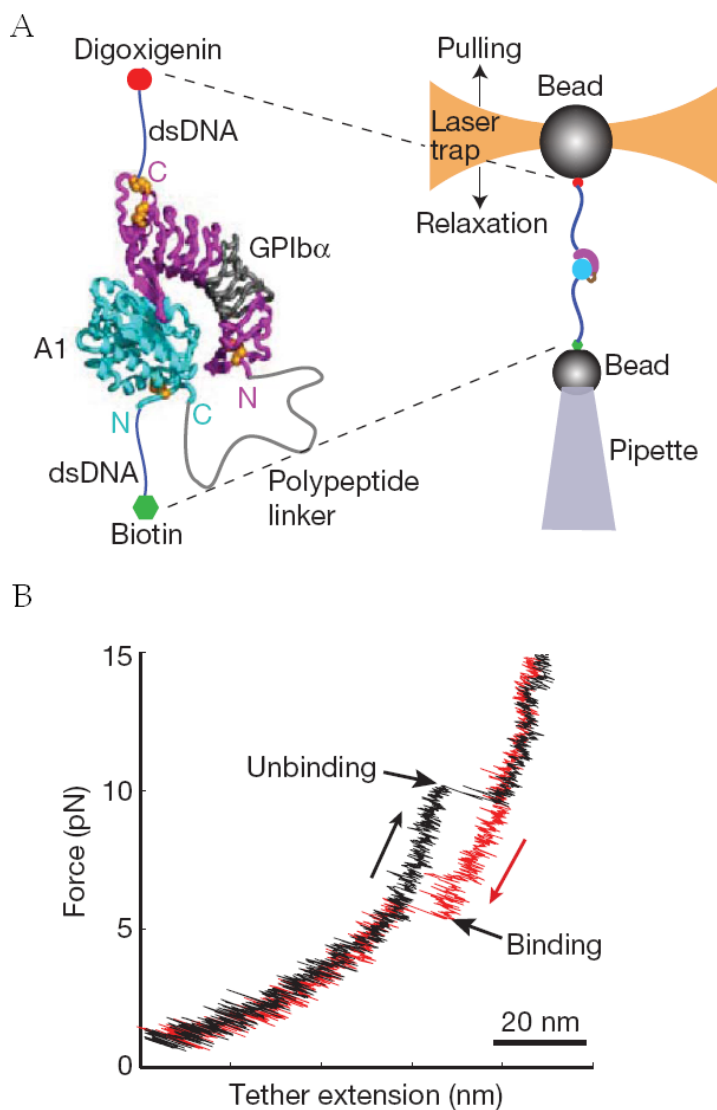


Fig. 1.7. The optical tweezers experiment. (A) The unbinding/binding experiment between two protein using optical tweezers. (B) Force-extension curve by the experiment. Figure reproduced with permission from Ref. [96], © 2010 NPG.

biomolecules in a timescale of 10^{-4} sec, which is much smaller than the timescale (*i.e.* 10^{-3} sec) available for AFM experiment. Moreover, the force resolution of LOT experiment is in the range of 1 pN (*e.g.* see Fig. 1.8), while the minimum resolution of AFM experiment is in the order of 10 pN. This indicates that LOT may allow for probing the quasi-equilibrium processes of single-molecule mechanics, which indicates that the free energy required to protein folding can be directly measured from the work done during the mechanical unfolding [97].

The principle of LOT experiment is to mechanically extend a single-molecule, whose ends are attached to two beads, where one bead is optically trapped while the other bead is pulled by using gradient force field of focused laser (see Fig. 1.7.A) [95]. The loading device of optical trap is well approximated as a linear spring (with its stiffness of 0.005 - 1 pN/nm) that is softer than AFM cantilever (whose stiffness is in the order of $10 - 10^5$ pN/nm). This leads to the conclusion that an accessible force resolution for LOT experiment is much smaller than that for AFM experiment as stated above [96]. The allowable force and time resolutions of LOT experiment is suitable to probe the mechanical work of molecular motors such as kinesin. A recent study [19] has reported the imaging-based observation of a kinesin walking on a microtubule by measuring the friction force between kinesin and microtubule using LOT experiment. In summary, LOT experiments are able to observe the mechanical behavior of various biomolecules in the unprecedented resolution of timescale and force resolution, which are appropriate to probe the biological functions of proteins.

1.2.1.C. Micro/Nano-Indentation Experiments

AFM-based indentation has been inspired from conventional mechanical testing techniques such as indentation and/or three-point bending test. AFM-based indentation has enabled the mechanical characterization soft materials at

nanoscale such as proteins (*e.g.* viral capsid, microtubule, amyloid fibril, etc.). In this Section, we only review two types of AFM experiments such as indentation and bending test.

The bending test is implemented by indenting a protein material (whose longitudinal dimension is much larger than other transverse dimension) that is deposited on a trenched substrate. When a force is applied at the mid-point of a protein fiber, the bending deflection at that point due to a force can be obtained from beam theory (*e.g.* Timoshenko beam model) as [98]

$$\begin{aligned}\delta &= \delta_B + \delta_S \\ &= \frac{FL^3}{192EI} + f_s \frac{FL}{GA} = \frac{FL^3}{192E_b I},\end{aligned}\quad (1.3)$$

where δ is the total deflection of a protein fiber, δ_B and δ_S represent the displacements driven by purely bending deformation and shear deformation, respectively, F is a mechanical load, L , E , I , and G indicate the length, bending elastic modulus, cross-sectional moment of inertia, and shear modulus of a protein fiber, respectively, and E_b is an effective elastic modulus for a protein fiber. The effective elastic modulus (or bending elastic modulus) for a protein fiber can be obtained by fitting Eq. (3) to a force-displacement curve obtained from AFM bending experiment. Based on Timoshenko (or Euler-Bernoulli) beam model, AFM bending experiments provides the measured elastic moduli of various protein materials such as insulin (with its modulus of 3.3 ± 0.4 GPa [99]), collagen fibril (with its modulus of 1 - 3.9 GPa [100]), and microtubule (whose modulus is in the range of 20 to 80 MPa [101]).

Even though AFM bending experiment provides the elastic properties of various protein materials as described above, it is inadequate to characterize the

mechanical behavior of protein materials whose longitudinal dimension is comparable to other transverse dimensions. For example, viral capsid looks like a sphere so that mechanical characterization of viral capsid cannot be made using AFM bending experiments. For such a case, AFM indentation is very useful in deciphering the mechanical properties of protein materials such as viral capsid [102]. The mechanical properties can be extracted from a force-displacement curve obtained from AFM indentation. In particular, the force-displacement relationship can be depicted based on Hertz theory [103]

$$F = \frac{4ER^{\frac{1}{2}}}{3(1-\sigma^2)} \delta^{\frac{3}{2}}, \quad (1.4)$$

where F is a mechanical load, δ is displacement due to indentation, R is the effective radius of curvature given as $1/R = 1/R_s + 1/R_L$ with R_s and R_L being the radii of curvature for sample and indenting tip, respectively, E and σ indicate the Young's modulus and Poisson's ratio of a protein material, respectively. AFM indentation has recently allowed for measuring the elastic modulus of protein materials such as β -lactoglobulin amyloid fibril (with its elastic modulus of 3.7 ± 1.1 GPa [40]), insulin amyloid fibril (whose elastic modulus is estimated as 7 – 41 MPa [104]), insulin crystal (with its elastic modulus of 150 – 180 MPa, and microtubules (with its elastic modulus of ~ 1 GPa [105].).

1.2.2. Computational Techniques

Even though experimental techniques such as AFM (or LOT) experiments are able to probe the mechanics of various biomolecules, they do not provide the detailed (atomic) structure of proteins. In order to construct structure-property-function relationship, it is required to have the information of a detailed (atomic)

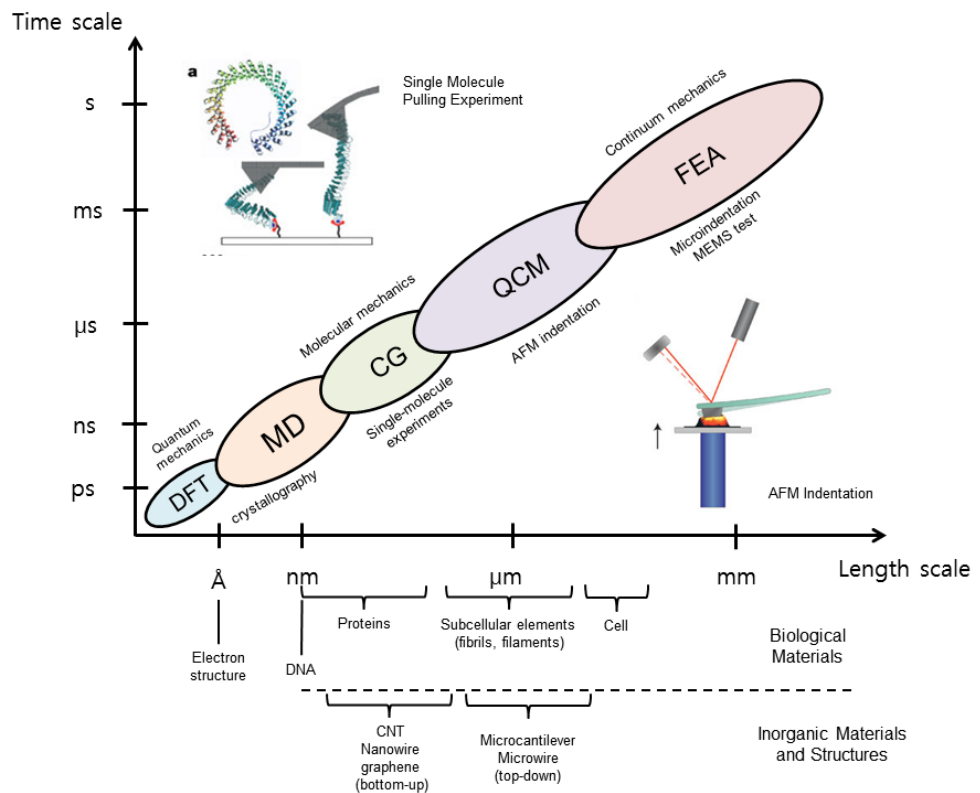


Fig. 1.8. The simulation technology in the various hierarchical structure with the time scale and length scale. [106]

structure of a protein material. Moreover, experimental techniques suffer from the difficulties in gaining detailed insight into the force-driven structural changes of a protein (*e.g.* force-induced unfolding of a folded domain). These restrictions can be overcome by considering the computational simulation techniques that allow for providing the detailed picture of the (atomic) structural changes of a protein in response to stimuli such as a load, temperature, etc. This implies that computational simulation techniques may be suitable for establishing the structure-property-function relationship of a protein. In this Section, we would like to briefly review the principles of various computational simulations techniques at multiple spatial and temporal scales (*e.g.* Fig. 1.8)

1.2.2.A. Molecular Dynamic Simulation

The fundamental principle of molecular dynamics (MD) simulation is to solve the equation of motion for all atoms that comprise an atomic structure such as protein structures. The equation of motion can be easily described by Newton's second's law such as

$$m_i \frac{\partial^2 \mathbf{x}_i(t)}{\partial t^2} + \gamma \frac{\partial \mathbf{x}_i(t)}{\partial t} = -\frac{\partial E(\mathbf{x}_1, \dots, \mathbf{x}_N)}{\partial \mathbf{x}_i} + \mathbf{R}_i(t). \quad (1.5)$$

where $\mathbf{x}_i(t)$ is the position vector of an i^{th} atom at time t , E is the potential energy of an atomic structure (*e.g.* protein structure), N is the total number of atoms, m_i is the atomic mass of an i^{th} atom, γ is a friction coefficient between an atomic structure and environment (*e.g.* solvent), and $\mathbf{R}_i(t)$ is a Gaussian white noise due to friction between an atomic structure and environment. The equation of motion depicted in Eq. (1.5) can be numerically integrated, for example, Verlet algorithm and Gear's fifth-order predictor-corrector method [107]. It should be noted that,

for simulating a protein structure, energy minimization to determine the equilibrium configuration of a protein has to be implemented before solving the equation of motion, since the experimentally available protein structure generally is not identical to the equilibrium configuration. This energy minimization process is equivalent to cooling of the protein structure. The numerical implementation of energy minimization has been now available such as steepest descent method, conjugate gradient method, and Newton-Raphson method [107].

As delineated in Eq. (1.5), the dynamics of a protein structure is governed by the potential field $E(\mathbf{x}_1, \dots, \mathbf{x}_N)$, which can be represented in the form [10]

$$E = E_{bond} + E_{angle} + E_{dihedral} + E_{vdW} + E_{el}. \quad (1.6)$$

The first three terms (*i.e.* E_{bond} , E_{angle} , and $E_{dihedral}$) describe the strain energies related to stretching, bending, and torsion of a covalent bond, respectively (see Fig. 1.9).

$$E_b = \sum_i k_b (r_i - r_{i+1})^2, \quad (1.7)$$

$$E_\theta = \sum_i k_\theta (\theta_i - \theta_{i+2})^2, \quad (1.8)$$

$$E_\phi = \sum_i |k_\phi| - k_\phi \cos n\phi_i, \text{ where } n = 1, 2, 3, 4, 5, 6, \quad (1.9)$$

where k_b , k_θ and k_ϕ represent the force constants for covalent bond stretch, bending of covalent bond, and torsion of covalent bond, respectively, r_i is the position vector of an i -th atom, θ_i is the i -th bending angle, and ϕ_i is the i -th dihedral angle.

The final two terms in Eq. (1.6) indicates the interaction energy between

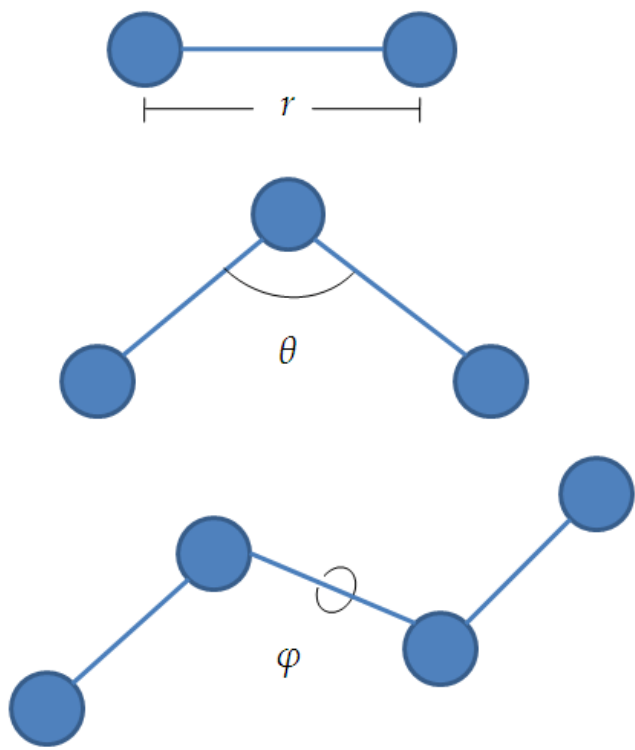


Fig. 1.9. Internal coordinates for bonded interactions of covalent bond, bond angle, dihedral angle (from up to down).

native contacts; this interaction energy consists of van der Waal's interaction and electrostatic (Coulombic) interaction such as

$$E_{vdW} = \sum_i \sum_{j>i} 4\epsilon_{ij} \left[\left(\frac{\sigma_{ij}}{r_{ij}} \right)^{12} - \left(\frac{\sigma_{ij}}{r_{ij}} \right)^6 \right], \quad (1.10)$$

$$E_{el} = \sum_i \sum_{j>i} \frac{q_i q_j}{4\pi\epsilon_0 r_{ij}}, \quad (1.11)$$

where ϵ_{ij} , and σ_{ij} indicate the energy well and equilibrium distance of van der Waal's interaction, respectively, r_{ij} is a distance between i^{th} and j^{th} atoms, ϵ_0 is electrical permittivity and q is electric charge of atom. The potential field suitable to describe the protein dynamics is available in codes such as CHARMM [108] and AMBER [109].

1.2.2.B. Steered Molecular Dynamic Simulation

Since a conventional MD simulation is not able to mimic the single-molecule force spectroscopy (based on AFM or LOT) that allows for mechanical extension of a single biomolecule, a steered MD simulation was suggested in 1990s in order to provide an insight into the single-molecule mechanics.

In these days, a steered MD simulation is provided in molecular dynamics packages such as NAMD [10]. The principle of steered MD simulation is to include the strain energy of a loading device (*e.g.* AFM or LOT) that is used to extend the single-molelcule. The strain energy of a loading device during mechanical stretching of a molecule is represented in the form [110]

$$E_L = \frac{k}{2}(vt - x)^2 \quad (1.12)$$

where k is the spring constant of a loading device, v is pulling speed, and x is the end-to-end distance of a molecule. As shown in Fig. 1.10 A, a steered MD simulation is able to capture the mechanical behavior of a protein molecule, particularly the force-driven unfolding of a protein domain. In particular, a steered MD simulation provides the detailed information of how a mechanical force is propagated to chemical bonds and drives the breakage of a chemical bond (see Fig. 1.10 B).

1.2.2.C. Normal Mode Analysis

Despite its ability to suggest the detailed, microscopic characteristics of protein dynamics, MD simulation is unable to provide the longtime simulation of protein dynamics, which is essential to gaining an insight into the biological functions of proteins at timescale of microseconds to milliseconds. In order to resolve the restrictions in timescales accessible with MD simulation, the normal mode analysis (NMA) has been taken into account due to its capability of analysis at longer timescale. It is attributed to the theoretical hypothesis that the global dynamics of a protein near a native state may be approximated as a harmonic motion, while the local dynamics of a protein is critically dependent on the detailed potential field as in MD simulation. There are two approaches in NMA-based analysis of the global dynamics of a protein; one is the essential dynamics, which applied NMA to the fluctuation matrix that can be computed based on MD trajectory. The other approach is to approximate the complicated potential as a harmonic potential. For more details, please refer to the literatures [111-114]. In this Section, we would like to review the latter case (*i.e.* harmonic approximation of a potential field). One may define the stiffness (Hessian) matrix

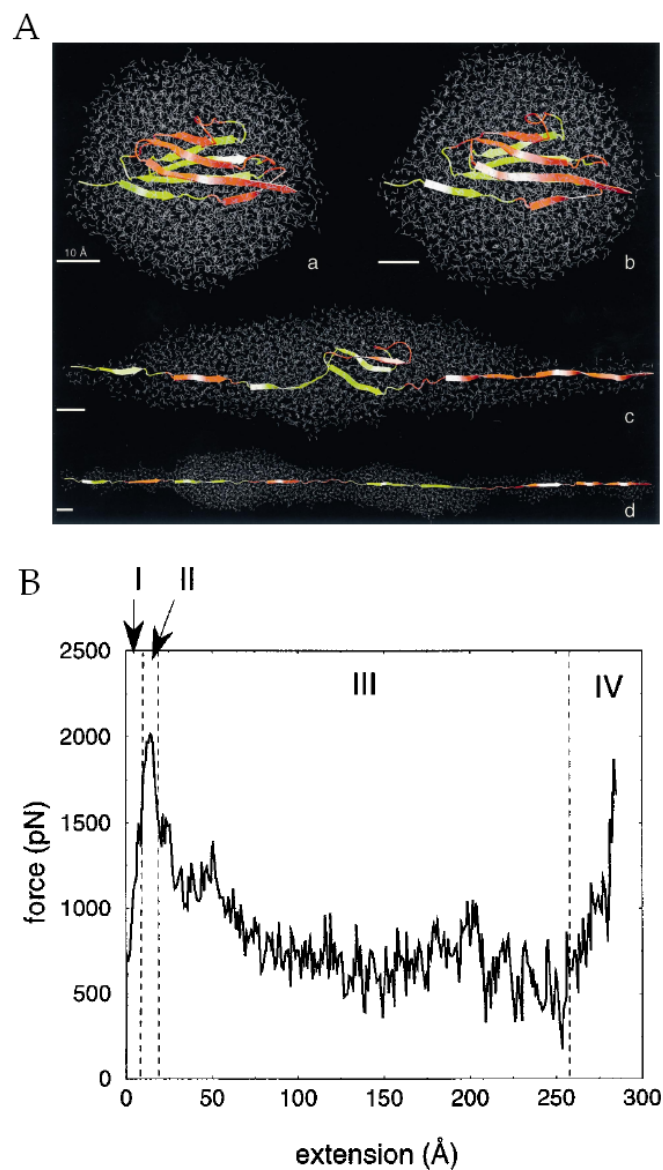


Fig. 1.10 (A) The unfolding trajectory of titin Ig domain. (a, extension 10 Å; b, 17 Å; c, 150 Å; d, 285 Å) (B) The unfolding force-displacement curve for unfolding of titin Ig domain. (I, preburst; II, major burst; III, post burst; IV, fully extended)
Figure (B) reproduced with permission from Ref. [110], © 1998 Cell Press.

of a protein by using Taylor series expansion of a potential field given by Eq. (1.6). The stiffness matrix (or Hessian matrix) K_{ij} is represented in the form

$$K_{ij} = \left. \frac{\partial^2 E}{\partial x_i \partial x_j} \right|_{x_0}, \quad (1.13)$$

where i, j indicates the indices of atoms. The vibrational behavior of a protein can be obtained by solving an eigenvalue problem given as

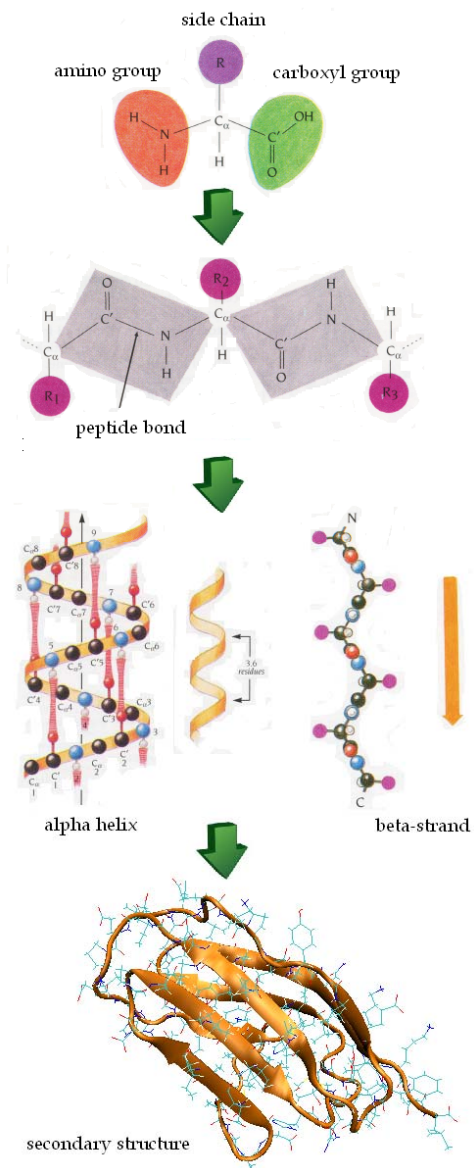
$$K_{ij} v_j = \omega_j^2 v_j. \quad (1.14)$$

Herein, v_j is eigenvector for j^{th} mode, and ω_j is j^{th} natural frequency. It has been remarkably found that the low frequency modes, except for six rigid body modes, are useful to describe the collective motion of protein [115].

1.2.2.D. Coarse-Grained (CG) Modeling and Simulations

As described earlier, atomistic simulations such as MD simulation and/or NMA are useful in deciphering the detailed microscopic dynamics of a protein. However, these simulations encounter the computational limitations such that the dynamics of large macromolecules (composed of $>10^6$ atoms) is still inaccessible with conventional atomistic simulations. This has led researchers to develop a novel modeling based on reduction of atomistic model. In particular, since protein dynamics is well dictated by a collective dynamics, researchers have attempted to build a coarsened model such that instead of using all atoms, a protein structure is described by pseudo atoms, which represent a group of

all-atom model



coarse-grained model

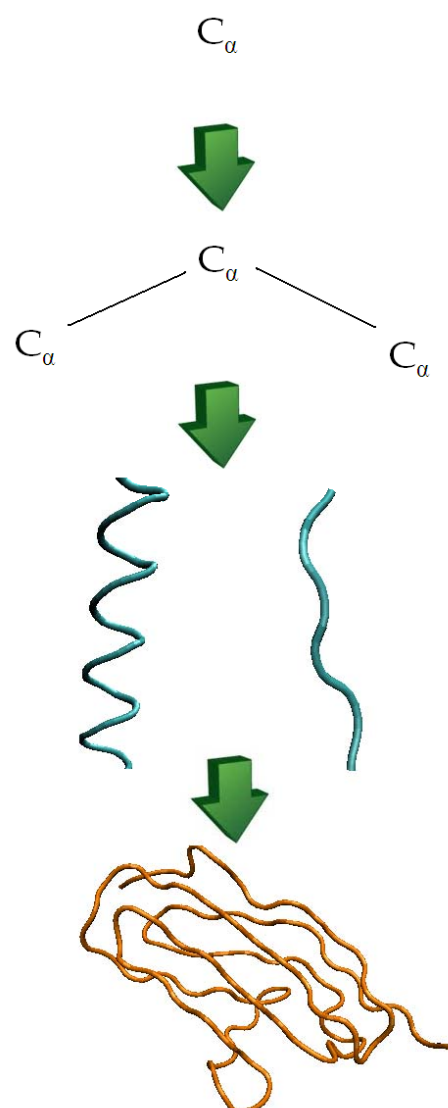


Fig. 1.11. The illustration of coarse-grained modeling method in the hierarchical structure of protein.

several atoms. There are two ways to determine a pseudo atom in a coarse-grained model; (i) the pseudo atom is located at the mass center of a group of atoms, or (ii) the pseudo atom is located at the position of a heavy atom that may govern the dynamics. Fig. 1.11 illustrates how one can construct a coarse-grained model of a protein structure. As an example, an amino acid consisting of N, C, O, H atoms is represented only by alpha carbon atoms. The coarse-graining allows for substantial reduction of the degrees of freedom of a protein structure, and consequently alleviating computational burden in simulating protein dynamics.

Once the degrees of freedom of a macromolecule are reduced in the coarse-graining, it is very important to construct an empirical potential field that is prescribed to the pseudo atoms of a coarse-grained model. One may construct the empirical potential field as in the case of MD simulation; for instance, an empirical potential field consists of strain energies related to stretching, bending, and twist of a covalent bond that connects two consecutively neighboring pseudo atoms, as well as interaction energy (*e.g.* van der Waals interaction, electrostatic repulsion, etc.) between pseudo atoms. The force constants can be empirically determined based on comparison between the trajectories obtained from classical atomistic simulation (*e.g.* MD simulation) and coarse-grained simulation. With the information of pseudo atoms and empirical potential field, one can numerically solve an equation of motion as in MD simulations.

1.3. Structure of Dissertation

This dissertation is aimed at providing the insight into the mechanical behavior of protein materials (and their relevant functions) at multiple scales using computational simulations and theories. Chapter 2 describes the force-driven chemical bond rupture at atomic scale using atomistic simulation as well as transition state theory. In Chapter 3, we have presented the mechanical

unfolding of a protein, particularly secondary structures (such as α helix) and a small protein domain (such as ubiquitin). It is found that the mechanical unfolding characteristic is dependent on the stiffness of a loading device, which indicates the significant role of a loading device in the mechanical characterization of protein molecules. Chapter 4 presents the mesoscopic modeling that allows for providing the mechanical properties (such as elastic modulus) of protein materials composed of protein crystals. It is shown that the folding topology of a protein crystal plays a critical role in the mechanical properties of protein materials. In Chapter 5, we have studied the mechanical behavior of protein filament (whose length scale is > 10 nm), particularly amyloid fibrils using coarse-grained model along with NMA. It is remarkably shown that the pattern of protein aggregation determines the mechanical properties of amyloid fibrils, which are related to disease expressions such as type II diabetes. This dissertation is concluded in Chapter 6, which presents the future outlook of simulation-based mechanical characterization of protein materials.

Chapter 2. Characterization of Bond Rupture Mechanics

2.1. Introduction

Single-molecule mechanical manipulation has been conceived as one of important nanomechanical tools that allow the characterization of biochemical reactions [13,116-120]. Over a last decade, single-molecule mechanical manipulation using a loading device such as atomic force microscopy (AFM) [13,116,117] and/or optical tweezer (OT) [118-120] has provided the mechanisms of bond rupture and/or protein unfolding, which plays a critical role on the biological function. The principle of single-molecule mechanical manipulation is that a single-molecule exhibiting a chemical bond or a folded domain is mechanically stretched via a loading device, which leads to ruptures of chemical bonds such as hydrogen bonds in a folded domain. In general, this mechanical unfolding process is usually non-equilibrium process [121], so that single-molecule mechanical manipulation does not provide the direct insights into free energy landscape relevant to a chemical bond or a folded domain.

There have been current attempts [71,79,80,122,123] to extract kinetic parameters, relevant to describe free energy landscape, from the single-molecule mechanical manipulation based on theoretical models for bond rupture kinetics. For instance, Bell [87] has introduced the simple, theoretical model of a bond rupture with assuming that bond rupture is well depicted by diffusion-like process like in Eq. (1.2). In a similar spirit, Evans and Ritchie [84] developed the theoretical model of bond ruptures based on Kramers theory [124] and Bell's model. Bell's model and Evans-Ritchie model have been successful in characterization of the free energy landscape extracted from single-molecule mechanical experiments [79,122]. However, Bell's model and Evans-Ritchie

model are only appropriate for a case, where a molecule is slowly stretched. In other words, if a molecular is pulled fast enough that stretching processes quickly reaches the non-equilibrium process, Bell's model and also Evans-Ritchie model are not suitable to describe the bond rupture mechanism in fast pulling regime, because of an assumption that energy barrier width Δx is constant and independent of mechanical force, which is unacceptable for fast pulling regime. In a recent decade, in order to overcome the restrictions of Bell's model and Evans-Ritchie model, there have been theoretical approaches that are able to explain the non-equilibrium process of bond rupture. For example, Hummer and Szabo [85] provided the theoretical framework that enables the interpretation of protein unfolding mechanics in the context of non-equilibrium experiment. In the similar spirit, Dudko et al. [125] had employed the Garg's argument [126] on escape field theory based on Kramers theory [124] in order to understand the bond rupture mechanism under non-equilibrium process. Moreover, with presumed free energy landscape, Dudko et al. [86] have found the theoretical model, referred to as DHS (Dudko-Hummer-Szabo) model, using Kramers theory to describe the rate constant for mechanical bond rupture under both nearly equilibrium and fully non-equilibrium processes. Further, theoretical models relevant to non-equilibrium process, such as Jarzynski's inequality [127] and/or Crooks' theorem [128], have been considered to extract the free energy landscape for a chemical bond or a protein folding from single-molecule mechanical experiments [119,129].

Extraction of free energy landscape from single-molecule experiments has been considered using theoretical models as described above. Here, theoretical models have been developed with assumption of soft loading devices [86,130,131], since loading device used in single-molecule mechanical manipulation usually exhibits the force constant of $< 0.1 \text{ N/m}$ [71,132]. In general,

mechanical behavior of a single-molecule depends on the loading devices. For example, AFM possesses the force constant of < 0.1 N/m and the available loading rate for AFM is usually in the range of 10^5 pN/s to 10^6 pN/s. On the other hand, the force constant of OT is much less than that of AFM by three orders, and the accessible loading rate is ~ 1 pN/s, much less than that available for AFM. This implies that single-molecule stretching by OT is almost the equilibrium process [97], whereas AFM-driven single-molecule experiment is very close to non-equilibrium process. This indicates that extraction of free energy landscape from single-molecule mechanical manipulation has to be carefully taken into account by considering the effect of loading device.

Recently, there have been current attempts to gain insights into the critical role of loading device in the mechanically induced bond ruptures. Evans [122] theoretically showed that the mean forces associated with a bond rupture are dependent on the stiffness of a loading device. This theoretical prediction has recently been validated by a recent study [133] that considers the experiments of bond ruptures using chemical force microscopy, especially the bond rupture mechanism under near-equilibrium pulling regime. Hummer and Szabo [85] developed a theoretical model including the effect of loading device in order to interpret the force-extension curves corresponding to protein unfolding experiments. Freund [134] provided the theoretical framework, which is able to depict the kinetic rate for bond rupture as a function of the stiffness of a loading device, based on assumed harmonic energy to describe a bond strength and Kramers theory. Maitra et al. [130] developed the theoretical model based on Kramers theory and DHS model for bond rupture kinetics in order to quantitatively describe the bond rupture kinetics with respect to the stiffness of a loading device. Tshiprut et al. [135] have employed Garg's argument for development of theoretical model to depict the bond rupture kinetics with

respect to the loading device effect. Van Vliet and coworkers [136] have experimentally showed the role of a loading device in the bond rupture mechanism using chemical force microscopy.

As stated above, the role of a loading device in the mechanical perturbation of free energy landscape has been validated by considering a simple bond rupture models and their related simulations and/or experiments. To our best knowledge, the role of a loading device in the protein unfolding mechanics has not been extensively considered elsewhere, albeit the protein unfolding experiment has been analyzed with a theoretical model including the effect of loading device [85]. However, a theoretical model in a recent study is inappropriate to interpret the protein unfolding mechanism driven by a stiff loading device. In this study, we have investigated the effect of loading device in the single-molecule manipulation of free energy landscape, related to bond rupture as well as protein unfolding. In particular, we have computationally studied the bond rupture mechanisms and the protein unfolding mechanics with respect to the stiffness of a loading device. We have also developed a theoretical model based on Kramers theory and presumed energy landscape such as linear-cubic potential in order to gain insights into role of loading device in the kinetics of bond rupture and/or protein unfolding. It is shown that not only the kinetic rate but also the mean forces (and also probability distributions of forces) associated with chemical bond rupture and/or protein unfolding mechanics are dependent on the stiffness of a loading device. Our simulation results on bond rupture have been validated by our theoretical model. Moreover, we have compared our theoretical model with other theoretical models such as Hummer-Szabo model [85] and Freund's model [134]. Our study sheds light on the importance of a loading device in interpretation of single-molecule experiments to extract the information of kinetics and free energy landscape.

2.2. Theory and Methods

2.2.1. Theory: Kramer's Theorem

2.2.1.A. Bell's Model: Conventional Bond Rupture Model

Here, we have showed that Bell's model is unable to describe the role of loading-device stiffness on the bond rupture mechanism. Let us consider a single chemical bond whose free energy landscape is assumed as simple, harmonic energy. In this case, the effective potential energy for a mechanically stretched chemical bond is given by $V_{eff} = (1/2)s_m x^2 + (1/2)s_L(x - \lambda)^2$, where s_m , s_L , x , and λ indicate the force constant of a chemical bond, the force constant of a loading device, a reaction coordinate, and a control parameter defined as $\lambda = vt$ with v being pulling rate, respectively. For soft loading device and weak force, the energy barrier becomes $\Delta V \approx -(\partial V / \partial \lambda) |_{eq} \Delta \lambda = -F \Delta \lambda$, where F is the force acting on a chemical bond, which can be measured at equilibrium such as $F = s_{eff} \lambda$ with s_{eff} being an effective force constant defined as $s_{eff} = (1/s_m + 1/s_L)^{-1}$, and $\Delta \lambda$ represents the difference in λ between bonded and denatured states. Here, $\Delta \lambda$ can be treated as a constant, that is, energy barrier width Δx . Consequently, the rate constant for bond rupture under nearly equilibrium process is given by Bell's theory.

$$k(t) = k_0 \exp\left(s_{eff} v t \Delta \lambda / k_B T\right) = k_0 \exp\left(\dot{F} t \Delta x / k_B T\right) \quad (2.1)$$

where \dot{F} is the loading rate defined as $\dot{F} = s_{eff} v$, and k_0 is the rate constant at zero force. Bell's model dictated in Eq. (2.1) is consistent with previous study by Tshiprut et al. [135]. This shows that the kinetic rate for a bond rupture is independent of force constant for a loading device. The rate equation for bond

rupture is described as $-dQ(t)/dt = k(t)Q(t)$, where $Q(t)$ is a survival probability, that is, a probability to have an intact chemical bond at time t . While a probability distribution for rupture force $p(F)$ is given by $p(F)dF = k(t)Q(t)dt$, the mean bond rupture force asymptotically approaches to $\langle F \rangle = (k_B T / \Delta x) \ln(\dot{F} e^{-\gamma} k_0^{-1} \Delta x)$ [for details, see Ref. [137]]. This indicates that mean rupture force is independent of force constant of loading device, as is anticipated from the fact that the kinetic rate given by Eq. (2.1) is uncorrelated with the force constant of a loading device. Therefore, Bell's model is unable to capture the effect of loading device on the bond rupture mechanism.

2.2.1.B. Bond Rupture Model: Kramers Theory

In order to understand the bond rupture mechanism, we would like to consider the simple, theoretical model that describes a chemical bond whose free energy landscape is represented with respect to reaction coordinate x . Here, free energy landscape for a chemical bond is depicted as $U_0(x)$, and the potential energy for a loading device to perturb the free energy landscape leading to bond rupture is given by $V_L(x) = (s_L/2)(x - \lambda)^2$, where λ is a control parameter, for a loading device, defined as $\lambda = vt$ with v being a pulling rate and t being the time. The probability density to have an intact chemical bond is well described by Smoluchowski equation [138].

$$\frac{\partial \psi}{\partial t} = \frac{\partial}{\partial x} D \left[k_B T \frac{\partial \psi}{\partial x} + \psi \frac{\partial V_{eff}}{\partial x} \right] \equiv \wp \psi \quad (2.2)$$

where $\psi(x, t; x_0)$ is the probability density to possess an intact bond at time t and reaction coordinate x under the initial position of x_0 , D is the diffusion coefficient, $k_B T$ is the thermal energy, $V_{eff}(x)$ is an effective potential field for a mechanically

stretched molecule such as $V_{eff}(x) = U_0(x) + V_L(x)$, and a symbol \wp indicates the differential operator defined as $\wp = (\partial/\partial x)[D\{k_B T(\partial/\partial x) + (\partial V_{eff}/\partial x)\}]^{1/2}$. The probability for an intact bond at time t , i.e. $Q(t; x_0)$, is given by

$$Q(t; x_0) = \int dx \cdot \psi(x, t; x_0) = \int dx \cdot \exp[t\wp] \cdot \delta(x - x_0) \quad (2.3)$$

where $\delta(x)$ is the Dirac delta function. Consequently, the probability distribution for a bond rupture time, $p(t; x_0)$, is represented as $p(t; x_0) = -dQ(t; x_0)/dt$, and then the mean unfolding time, $\tau(x_0)$, is given by

$$\tau(x_0) = \int_0^\infty dt \cdot t \cdot p(t; x_0) = \int_0^\infty dt \int dx \cdot \delta(x - x_0) \cdot \exp[t\wp^\dagger(x)] \quad (2.4)$$

Here, the integration of parts was used, and a symbol \wp^\dagger represents an adjoint to a differential operator \wp . The rate constant for a bond rupture, k , is thus obtained as

$$k(t) \equiv \frac{D\omega_b(t)\omega_{ts}(t)}{2\pi k_B T} \exp\left[-\frac{\Delta V(x; t)}{k_B T}\right] \quad (2.5)$$

This formula is renowned as Kramers' theory [139] that was revisited by Evans and Ritchie [84]. Here, $\omega_b(t)$ and $\omega_{ts}(t)$ represent the natural frequencies at an equilibrium for bonded state and a local equilibrium at which barrier crossing (that is, bond rupture) occurs, and $\Delta V(x; t)$ is the energy barrier defined as $\Delta V(x; t) = V_{eff}(x_{ts}; t) - V_{eff}(x_b; t)$, where x_b and x_{ts} indicate the reaction coordinates at an equilibrium for bonded state and a local equilibrium at which bond rupture

happens, respectively. It should be recognized that Kramers' theory [139] is a generic model to describe the bond rupture over the entire regime of pulling rates. In general, Bell's model [140] only captures the bond rupture event when a mechanical stretching of a chemical bond is almost equilibrium process (i.e. very slow pulling rate), while Garg's escape field theory [126] is only appropriate to describe the bond rupture when a chemical bond is stretched by a critical loading rate at which energy barrier instantaneously disappears [141].

2.2.1.C. Mechanical Rupture of Chemical Bond Described by Linear-Cubic Potential Using Kramers Theory

We consider the one-dimensional free energy landscape for a chemical bond (or equivalent to folded protein domain) represented in the form of $U_0(x) = (3/2)\Delta G_0(x/\Delta x_0) - 2\Delta G_0(x/\Delta x_0)^3$, where ΔG_0 is an energy barrier at zero force, and $\Delta x_0 = x_{ts}^0 - x_b^0$, where x_{ts}^0 and x_b^0 indicate the reaction coordinates at equilibrium for bonded (folded) state and at transition state (at which bond rupture occurs) with zero force, respectively. Here, it should be noticed that free energy landscape $U_0(x)$ is able to capture the free energy landscape for a folded protein domain with respect to reaction coordinate [86]. In order to introduce the effective force constant s_{eff} (as shown above), the free energy $U_0(x)$ has to be simplified using harmonic approximations: $U_0(x) \approx (1/2)s_m x^2$, where $s_m = 6\Delta G_0/(\Delta x_0)^2$. Subsequently, the effective force constant is given as $s_{eff} = (1/s_m + 1/s_L)^{-1} = 6\Delta G_0 s_L / [6s_L(\Delta x_0)^2 + 6 \Delta G_0]$. The effective potential for a mechanically stretched bond is given by $V_{eff} = U_0(x) + V_L(x, t)$, where $V_L(x, t)$ is the harmonic potential corresponding to a loading device such as $V_L(x, t) = (s_L/2)[vt - (x + \Delta x_0/2)]$. With an effective potential, the reaction coordinates x_{ts} and x_b becomes dependent on the control parameters of loading device. One can straightforwardly find the reaction coordinates $x_{ts}(\lambda)$ and $x_b(\lambda)$ from $\partial V_{eff}/\partial x = 0$.

$$\bar{x}_b(\bar{\lambda}) = \varepsilon - 0.5\sqrt{4\varepsilon^2 + 4\varepsilon(1-2\bar{\lambda})} + 1 \quad (2.6.a)$$

$$\bar{x}_b(\bar{\lambda}) = \varepsilon + 0.5\sqrt{4\varepsilon^2 + 4\varepsilon(1-2\bar{\lambda})} + 1 \quad (2.6.b)$$

Here, we have introduced the dimensionless parameters using normalizations such as $\bar{x}_b \equiv x_b/\Delta x_0$, $\bar{x}_{ts} \equiv x_{ts}/\Delta x_0$, $\bar{\lambda} = \lambda/\Delta x_0 \equiv vt/\Delta x_0$, and $\varepsilon = s_L(\Delta x_0)^2/12\Delta G_0$. Herein, $\bar{\lambda}$ is a dimensionless pulling rate, and ε is a non-dimensional force constant of loading device. For the slow pulling of a bond with very soft spring, the reaction coordinates $x_{ts}(\lambda)$ and $x_b(\lambda)$ asymptotically approaches to $x_{ts} \approx \varepsilon\Delta x_0 - 0.5\Delta x_0$ and $x_b \approx \varepsilon\Delta x_0 + 0.5\Delta x_0$. One can easily discover that, for slow pulling with very soft loading devices, the energy barrier width is independent of control parameters of a loading device and given as $\Delta x \equiv x_{ts} - x_b \approx \Delta x_0$. This indicates that Bell's model using the constant energy barrier width is the limiting case to the slow pulling with soft loading device. With reaction coordinates given by Eq. (2.6), the energy barrier under the mechanical stretching induced by a loading device is represented in the form of

$$\begin{aligned} \Delta \bar{V} &\equiv \frac{\Delta V}{\Delta G_0} = \frac{V_{eff}(x_{ts}; t) - V_{eff}(x_b; t)}{\Delta G_0} = [1 + 4\varepsilon^2 + 4\varepsilon(1 - \bar{\lambda})]^{3/2} \\ &\equiv [1 + 4\varepsilon^2 + 4\varepsilon - 4\dot{F}\tau]^{3/2}, \end{aligned} \quad (2.7)$$

where \dot{F} is the loading rate defined as $\dot{F} = s_{eff}v$, and τ is the normalized time-scale defined as $\tau = (1+2\varepsilon)t/2s_m\Delta x_0$. For slow pulling with soft loading device, it is shown that energy barrier asymptotically approaches to $\Delta V \approx \Delta G_0(1 - 12\varepsilon\bar{\lambda}) + O(\bar{\lambda}^2) = \Delta G_0 - s_L\lambda\Delta x_0 \equiv \Delta G_0 - (1 + \varepsilon)(\Delta x_0)\dot{F}t$. For the limiting

case of soft loading device, i.e. $\varepsilon \ll 1$, the energy barrier becomes $\Delta V \approx \Delta G_0 - (\Delta x_0) \dot{F}t$, which is consistent with Bell's model on bond rupture. This indicates that the limiting case is unable to capture the effect of loading device on the kinetics of bond rupture. With Kramers' theory dictated by Eq. (2.5), the kinetic rate for bond rupture driven by loading device is given by

$$\begin{aligned}\bar{k}(\dot{F}, \varepsilon) &= \bar{k}(t) = \frac{1}{\bar{T}} \sqrt{1 + \frac{1}{3} \varepsilon^2 + 4\varepsilon(1-2\bar{\lambda})} \exp\left[-\frac{\pi}{3\bar{T}} \{1 + 4\varepsilon^2 + 4\varepsilon(1-\bar{\lambda})\}^{3/2}\right] \\ &= \frac{1}{\bar{T}} \sqrt{1 + \frac{\varepsilon^2}{3} + 4\varepsilon - 8\dot{F}\tau} \exp\left[-\frac{\pi}{3\bar{T}} \{1 + 4\varepsilon^2 + 4\varepsilon - 4\dot{F}\tau\}^{3/2}\right],\end{aligned}\quad (2.8)$$

where $\bar{k}(\dot{F}, \varepsilon)$ is the normalized rate constant for bond rupture, defined as $\bar{k} = k(t) \cdot (\Delta x_0)^2 / D$, and \bar{T} is the dimensionless temperature defined as $\bar{T} = \pi k_B T / 3\Delta G_0$. As is described in Eq. (2.8), the kinetic rate for bond rupture is determined by two significant parameters \dot{F} (i.e. loading rate) and ε (i.e. stiffness of loading device). In case of soft loading device (i.e. $\varepsilon \ll 1$) and slow pulling rate (i.e. $\dot{F}\tau \ll 1$), the kinetic rate for bond rupture approaches to $k(t) \approx \bar{T}^{-1} \exp[-(\pi/3\bar{T})(\Delta G_0 - \dot{F}t\Delta x_0)]$, which is consistent with Bell's model where bond rupture kinetics is independent of force constant of a loading device.

Once the kinetic rate is explicitly obtained, we need to know the probability distribution of bond rupture force, since single-molecule experiments provide such probability distribution and its corresponding mean value of bond rupture force. With assumption that bond rupture is described as first-order phase transition, we can find the probability to have an intact bond at time t , $Q(t)$, from a relation of

$$\frac{dQ}{dt} = -k(t) \cdot Q(t) \quad (2.9)$$

It should be noticed that the force exerted by loading device at time t is given as $F(t) = s_L v t$. The probability $Q(F)$ is represented in the form of

$$Q(F) = \exp \left[-\frac{1}{s_L v} \int_0^F k(F') dF' \right] \quad (2.10)$$

Here, the rate constant k and the probability Q are expressed with respect to force $F(t)$ rather than time t . The probability distribution of bond rupture forces is given by

$$p(F) = -\frac{k(F)}{s_L v} \exp \left[-\frac{1}{s_L v} \int_0^F k(F') dF' \right] \quad (2.11)$$

The mean rupture force is, thus, calculated from a relation of

$$\langle F \rangle = \int_0^\infty F \cdot p(F) dF = \int_0^\infty -\frac{F \cdot k(F)}{s_L v} \exp \left[-\frac{1}{s_L v} \int_0^F k(F') dF' \right] dF \quad (2.12)$$

The mean rupture force depicted by Eq. (12) is well defined regardless of loading-device stiffness. For soft loading device, the asymptotic expression of mean rupture force is given in Ref. [142].

2.2.2. Numerical Method: Brownian dynamics

For simulation of bond rupture, we have employed the Brownian dynamics, which discards the inertia effect in the Langevin dynamics. The reaction coordinate $x(t)$ under the mechanical stretching is described as

$$x(t + \Delta t) = x(t) + \frac{\Delta t}{\gamma} \left[-\frac{\partial V_{\text{eff}}}{\partial x} + \xi(\Delta t) \right] \quad (2.13)$$

where Δt is the time step for numerical integration (here, we set $\Delta t = 100$ ps), γ is the friction coefficient arising from friction between a bond and environment, V_{eff} is an effective potential given by $V_{\text{eff}}(x) = U_0(x) + V_L(x)$ with $U_0(x)$ and $V_L(x)$ being the potential fields for a bond and a loading device (Eq. 1.12), respectively, and $\xi(\Delta t)$ is the Gaussian random force driven by thermal fluctuation. It should be noticed that the time step of 100 ps is acceptable based on stability criterion [143]. Herein, we have used the Morse potential to describe a chemical bond, i.e. $U_0(x) = U_0[\{1 - \exp(-2b(x - R_c)/R_c)\}^2 - 1]$, and we set $U_0 = 0.12$ nN nm, $b = 1.5$, $R_c = 0.24$ nm, $\gamma = 7.7 \times 10^{-6}$ kg/s, $T = 293$ K for validation [125].

2.3. Results

2.3.1. Theoretical Predictions on the Role of Loading Device in the Bond Rupture Mechanism

In order to theoretically understand the role of loading device on the single-molecule pulling experiment, we have taken into account a theoretical model based on a presumed free energy landscape such as linear-cubic shape and Kramers theory. As described in Supporting Information, with presumed linear-cubic potential for a chemical bond, the kinetic rate $k(t)$ for a bond rupture is given by Eq. (2.8) which explicitly shows that kinetic rate for bond rupture is

dependent on the stiffness of a loading device.

Fig. 2.1 (a) shows the free energy landscape (described by linear-cubic potential) that is perturbed by mechanical stretching using loading device with its different stiffness. It is shown that free energy landscape for mechanically stretched bond is governed by stiffness of loading device such that stiffer loading device induces the more perturbation in the free energy landscape. This implies that stiffer loading device drives the fast kinetics of bond rupture. The inset of Fig. 2.1 (a) depicts the normalized energy barrier, $\Delta\bar{V}$, as a function of dimensionless force constant of loading device, ε , and normalized pulling rate $\bar{\lambda}$. It is illustrated that energy barrier is decreasing when the stiffness of loading device increases. In other words, stiffer loading device triggers the faster bond rupture, indicating that energy barrier disappears fast when stiff loading device is employed for mechanical stretching. As shown Fig. 2.1 (b), we have theoretically suggested that the kinetic rate for bond rupture is strongly affected by force constant of loading device. This indicates that mechanical stretching of a bond undergoes the non-equilibrium process when stiff loading device is used. With model parameters such as $\Delta G_0 = 0.24 \text{ nN nm}$, $\Delta x_0 = 0.3 \text{ nm}$, $D = 538 \text{ nm}^2/\text{s}$, $T = 293 \text{ K}$, as presented in Fig. 2.1 (c) and (d), theoretical calculation based on Eqs. (2.10) and (2.11) provides the probability distribution of bond rupture forces at loading rate of $\dot{F} = 1 \text{ nm/s}$ and the mean rupture forces as a function of loading rate, \dot{F} , and force constant of loading device, s_L . It is comparable to the recent theoretical model for the effect of pulling device stiffness in the analyses of single-molecule force measurements. In this research, the relation of mean escape force and the loading device stiffness is validated with non-dimensional parameters [130]. It is shown that as long as the stiffness of loading device is in the range of 0.01 N/m to 0.1 N/m , the mean rupture force is almost independent of the stiffness of a loading device, whereas the stiff loading device (e.g. $s_L = 1$

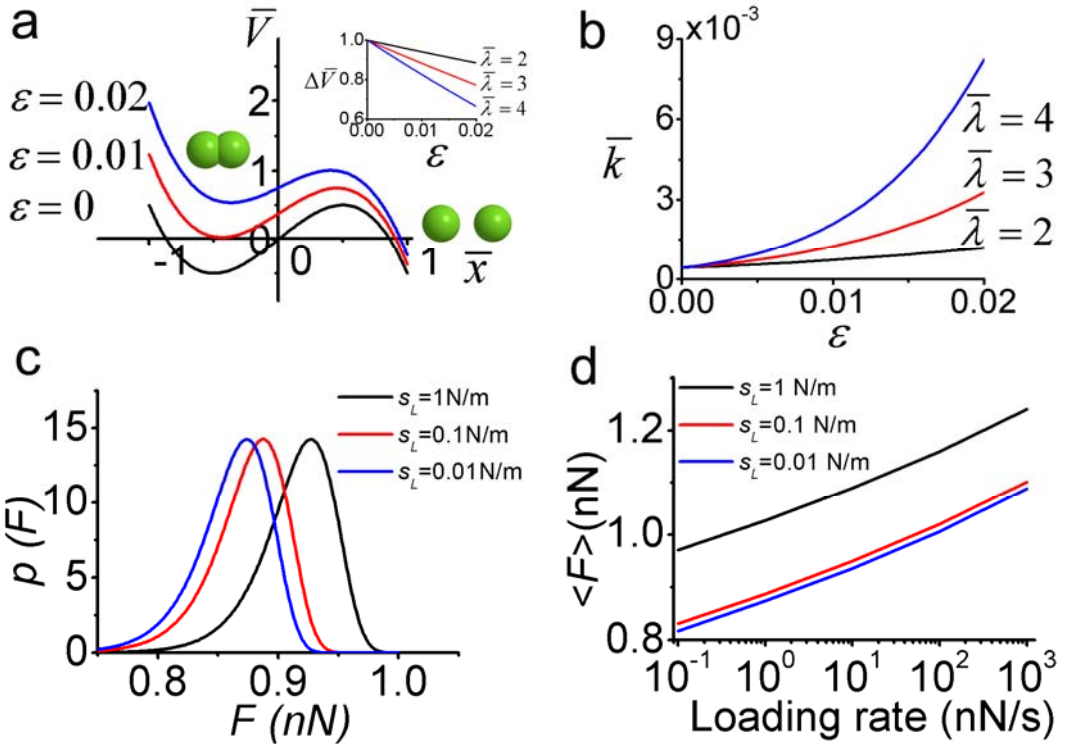


Fig. 2.1 (a) Dimensionless free energy landscape with mechanical perturbation by a loading device with different stiffness. Inset shows the free energy barriers with respect to dimensionless pulling rates $\bar{\lambda}$ and the dimensionless stiffness ε of loading device. (b) Normalized kinetic rate \bar{k} for bond rupture as a function of dimensionless pulling rate and the dimensionless stiffness of loading device. Here, the dimensionless temperature is given as $\bar{T} = 0.105$. (c) Probability distributions of bond rupture forces with respect to the stiffness s_L of a loading device. Here, the model parameters are described in the text. (d) Mean rupture forces as a function of loading rate as well as the stiffness of a loading device.

N/m) enhances the mean rupture force significantly.

2.3.2. Brownian Dynamics Simulations on Bond Ruptures: Loading-Device Stiffness vs. Rupture Forces

For insightful descriptions on the generic bond rupture mechanism, we have employed the Brownian dynamics simulation of bond rupture. It should be noticed that our theoretical calculations assume that free energy landscape is in the form of linear-cubic potential. However, in general, the free energy landscape for a chemical bond is not linear-cubic form but depends on the physical model of a bond. Moreover, in our simulation, it should be noted that Brownian dynamic simulation is valid for a case, where energy dissipation due to friction between environment and a chemical bond dominates the reaction process. That is, the inertia effect is assumed to be insignificant in the bond rupture process. Our simulation also presumes that the free energy landscape for a chemical bond is depicted by Morse potential, which is suitable to describe the chemical bond in biological system, e.g. hydrogen bond connecting two phosphates in double-stranded DNA [144]. Fig. 2.2(a) presents the force $F(t)$, which is exerted by a loading device, with respect to time t for a mechanically stretched chemical bond with a loading rate of $\dot{F} = 1 \text{ nN/s}$. Here, the loading rate is given by a relation of $\dot{F} = s_{\text{eff}}v$, where s_{eff} is an effective force constant, which is obtained as a slope of the force-extension curve (i.e. $s_{\text{eff}} = \partial F / \partial u$ with F and u being the force and the displacement, respectively, i.e. $u = vt$), and v is the pulling rate. This force curve is comparable to the result of bond rupture experiment by Evans group. They show the rupture of receptor-ligand bonds occurs after few milliseconds to tens of seconds when the mechanical loading is applied [145]. Also, the experiment using OT shows the force curve of bond rupture phenomenon between P-selectin and PSGL-1 [146]. The rebinding of a bond is observed for mechanical stretching

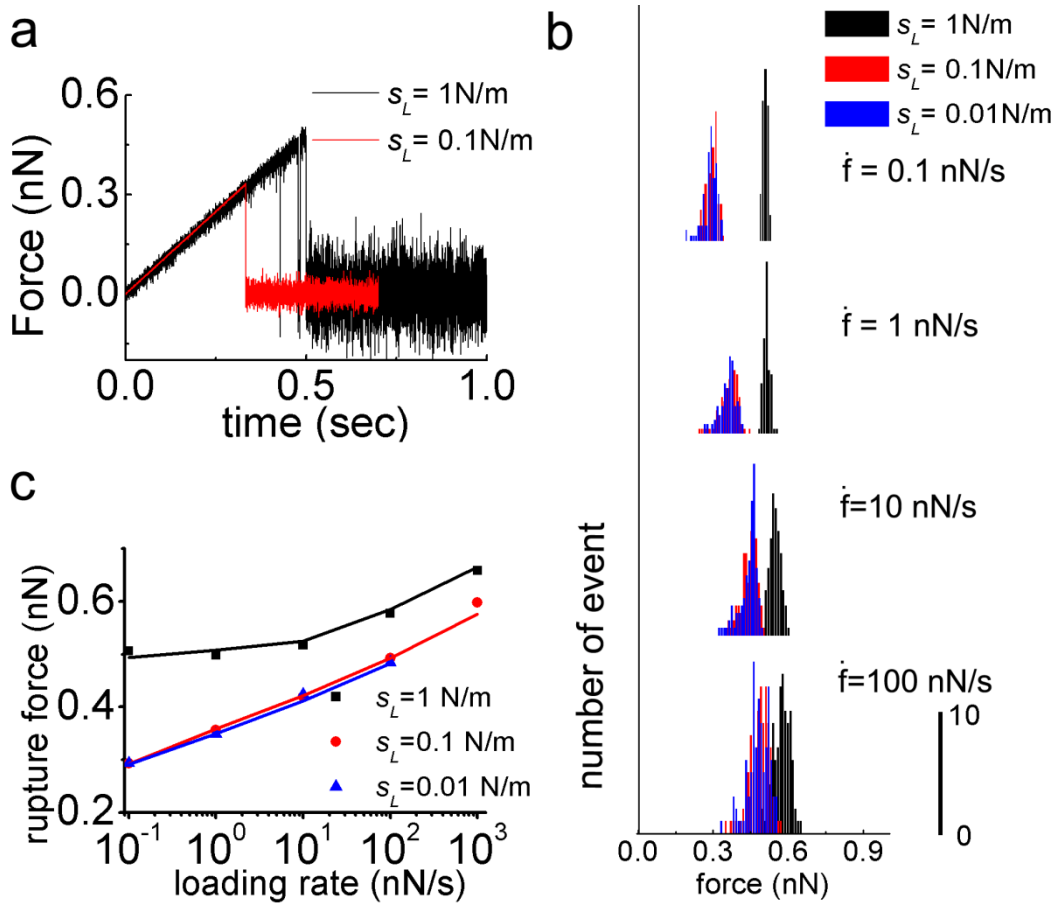


Fig. 2.2 (a) Force exerted by a loading device (with loading rate of $\dot{F} = 1 \text{ nN/s}$) is shown with respect to stiffness of loading device. (b) Probability distributions of bond rupture forces are presented as a function of loading rate and the stiffness of a loading device. (c) Mean bond rupture forces with respect to stiffness of loading device and loading rate. Here, solid line shows the fitting to the theoretical model.

using stiff loading device at loading rate in the range of 0.1 nN/s to 10 nN/s, whereas such rebinding is not found when a chemical bond is stretched by a soft loading device (see Fig. 2.2 (a) and 2.2 (c)). It is attributed to the fact that stiff loading device induces the smaller energy barrier ΔV (e.g. Fig. 2.1 (a)), which allows a chemical bond to undergo the phase transition between native state and denatured state easily via thermal fluctuation. However, energy barrier crossing by soft loading device is not as fast as that using stiff loading device, which may result in the irreversible bond rupture driven by soft loading device. As a consequence, the rebinding of denatured bond is not found when soft loading device is used for mechanical stretching. Fig. 2.2 (b) shows the probability distributions of bond rupture forces with respect to loading rate and the stiffness of a loading device. The distributions are obtained by 100 times Brownian dynamic simulations at each loading rate and loading device stiffness. In this result, the distribution of the rupture force increases with the increase of loading rate, and it is comparable to the result of experiment and simulation [125,145,146]. The rupture forces are few pico-Newtons when the loading device is OT, but the forces are up to hundreds of pico-Newtons when the device is AFM. It is comparable to the tendency of the Fig. 2.2 (b). The mean rupture forces as a function of loading rate and stiffness of loading device are depicted in Fig. 2.2 (c). It is found that mean rupture force is increased when a stiff loading apparatus is utilized. Moreover, it is shown that when a bond is extended using stiff loading device at relatively low loading rate (e.g. 0.1 N/s – 1 N/s), the mean rupture force is asymptotically close to ~ 0.5 nN due to the rebinding of a bond. This phenomenon found here is consistent with a theoretical prediction in recent studies [122,128]. Specifically, at near-equilibrium regime, the mean rupture force is given by $F_{eq} = (2s_L\Delta G_0)^{1/2}$ [133], which suggests the energy barrier of $\Delta G_0 = 0.125$ nN nm. This quantity is consistent with the energy barrier of Morse-

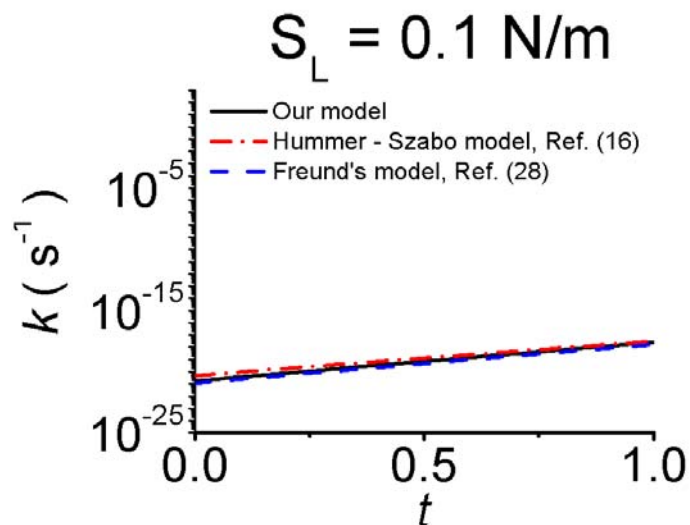
potential used in the simulation such as $\Delta G_0 = 0.12$ nN nm. The computational simulations of bond ruptures suggest that the stiffness of loading device has to be importantly taken into account when one attempts to extract the parameters for free energy landscape, e.g. energy barrier and/or energy barrier width, based on single-molecule pulling experiments.

In order to validate our theoretical model on bond rupture mechanism, we consider the simulations of chemical bond rupture and/or protein unfolding mechanics. Specifically, we fit our theoretical model to our simulation results on bond rupture and/or protein unfolding mechanics. As shown in Fig. 2.2 (c), the mean rupture forces as functions of loading rate and the stiffness of loading device were well fitted with our theoretical model, even though our model uses the linear-cubic potential to describe a bond whereas simulations employs the Morse potential to dictate the hydrogen bond. In particular, fitting parameters for chemical bond rupture are obtained as $k_0 \equiv \{D/(\Delta x_0)^2\}(3\Delta G_0/\pi k_B T) \exp(-\Delta G_0/k_B T) \approx 10^{-7} - 10^{-6}$ s⁻¹, $\Delta x_0 = 0.2 \pm 0.03$ nm, and $\Delta G_0 \approx 0.12 \pm 0.02$ nN nm, which is consistent with the model parameters used in the simulation.

2.3.3 Comparison of the theoretical model with others

For gaining insight into the robustness of our theoretical model, we have considered the theoretical models by Freund [134] and Hummer et al. [85]. Here, it should be noted that our theoretical model is essentially identical to that of Maitra et al. [130]. As shown in Fig. 2.3, for mechanical stretching of a bond using soft loading device, three models predict the identical kinetic rate for a bond rupture. However, for a mechanical extension of a bond using stiff loading device, our model and Freund's model predicts the higher kinetic rate for a bond rupture than that predicted by Hummer-Szabo model. This is attributed to the fact that the Hummer-Szabo model is appropriate to describe a bond rupture

a



b

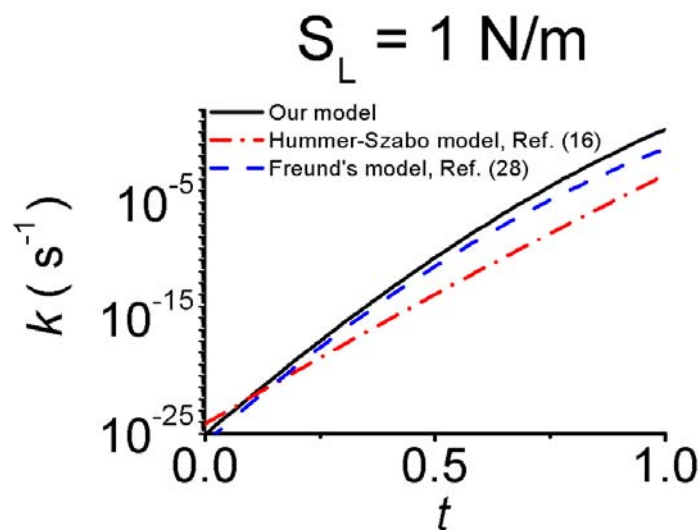


Fig. 2.3 Comparison between kinetic rates for bond ruptures predicted by our theoretical model, Hummer-Szabo model, and Freund's model as a function of the stiffness of a loading device: (a) $s_L = 0.1 \text{ N/m}$, and (b) $s_L = 1 \text{ N/m}$.

when the energy barrier is still large. That is, Hummer-Szabo model may be unable to describe a bond rupture event by a stiff loading device such that the energy barrier disappears relatively fast. On the other hand, our model based on linear-cubic potential predicts the kinetic rate for a bond rupture quantitatively comparable to that predicted by Freund's model. This indicates that the dependence of kinetic rate on the stiffness of a loading device is insensitive to the detailed shape of free energy landscape.

2.4. Summary

In this chapter, the role of loading device on the bond rupture mechanism is elucidated based on computational simulations with a theoretical model. The Brownian dynamic simulation is used to mimic single bond breaking, and the Kramer's model is applied for validation the simulation results. It is shown that rate constant for bond rupture is determined by two parameters such as loading rate and the stiffness of a loading device.

Chapter 3. Mechanical Behavior of Secondary Structure of Proteins

3.1. Introduction

In this chapter, the single molecule experiment of secondary structure of proteins such as α -helix, β -hairpin, and ubiquitin is studied with coarse-grained approach of unfolding simulation. The coarse-grained model is suitable to describe efficiently the protein unfolding mechanics using only the topology of protein (see section 1.2.2.D for details).

The α -helix is major elements of secondary structure of protein [6]. There are 3.6 residues per turn in an α -helix, which corresponds to 5.4 Å (1.5 Å per residue). All hydrogen bonds in an α -helix point in the same direction because the peptide units are aligned in the same orientation along the helical axis. The β -sheet is second important element of secondary structure in proteins. There are two types' configurations of β -sheet such as parallel and antiparallel, and especially the β -hairpin is antiparallel structure. The hydrogen bonds in β -sheets are aligned perpendicular with the direction of β -strand.

The ubiquitin is one of the elastomeric proteins which has a 76-amino-acid globular shape and consists of 3 α -helices and 4 β -strands. The ubiquitin is essential for the degradation of misfolded proteins in proteasome [147]. The unfolding characteristics of ubiquitin are introduced in many researches [83,93,148-155]. The ubiquitin is attached to so many other proteins with the form of linear chains such as N-C linked chains or linked between their C terminus and lysine residue such as Lys 11, Lys 29, Lys 48, or Lys63. Therefore the anisotropic characteristics of ubiquitin are investigated with AFM experiment and SMD simulation, for examples, that the unfolding force of N to C linked is larger than that of Lys48 to C [93].

The unfolding force can be affected by the loading device stiffness according to the reaction rate theory which is introduced in Chapter 2., but the loading device effect in protein unfolding is not reported. In this chapter, the loading device effect in single molecule experiment is studied with unfolding simulation of β -hairpin. Moreover, the unfolding characteristics of α -helix and β -hairpin are compared, and the unfolding pathway of ubiquitin is studied with the anisotropic characteristics.

3.2. Method: Gō Model

The governing equation for protein unfolding mechanics is spiritually identical to that for bond rupture simulation in Chapter 2.

$$\mathbf{r}_i(t + \Delta t) = \mathbf{r}_i(t) + \frac{\Delta t}{\gamma} \left[-\frac{\partial V_{\text{eff}}(\mathbf{r})}{\partial \mathbf{r}_i} + \mathbf{R}_i(\Delta t) \right]. \quad (3.1)$$

Here, \mathbf{r}_i is the position vector of i^{th} alpha carbon atom, \mathbf{r} indicates the coordinates of all residues, i.e. $\mathbf{r} = [\mathbf{r}_1, \dots, \mathbf{r}_N]$, where N is the total number of residues, $V_{\text{eff}}(\mathbf{r})$ is an effective potential defined as $V_{\text{eff}} = U_0 + V_L$ with U_0 and V_L being the potential energies for a protein and a loading device, respectively. When constant velocity pulling force is applied $V_L = k(vt - \mathbf{r}_i^0)/2$ where k is stiffness of loading device, t is time, and \mathbf{r}_i^0 is displacement of pulled atoms from origin in the protein. The constant force loading condition is $V_L = Ft$, where F is constant force applied to pulled atoms. In this simulation, both of N-turminus and C-turminus are pulled. $\mathbf{R}_i(t)$ is the Gaussian random force acting on residue i , whose mean is zero and the standard deviation is $\sqrt{2\gamma k_B T / \Delta t}$. We have employed the Gō potential to describe the protein structure [156].

$$U_0(\mathbf{r}) = \sum_{i=1}^{N-1} \sum_{j=i+1}^N \left[\left\{ \frac{k_1}{2} (d_{ij} - d_{ij}^0)^2 + \frac{k_2}{4} (d_{ij} - d_{ij}^0)^4 \right\} \delta_{j,i+1} + 4e_0 \left\{ \left(\frac{\sigma}{d_{ij}} \right)^{12} - \left(\frac{\sigma}{d_{ij}} \right)^6 \right\} (1 - \delta_{j,i+1}) \right], \quad (3.2)$$

where d_{ij} is the distance between two residues i and j , k_1 and k_2 are force constants for harmonic and quartic potentials, respectively, for a covalent bond, e_0 is the energy parameter for native contact, and σ is a length scale for native contact, δ_{ij} is the Kronecker delta, and superscript 0 indicates the equilibrium state. Herein, we have set $d_{ij}^0 = 3.8 \text{ \AA}$, $k_1 = e_0/\text{\AA}^2$, $k_2 = 100 e_0/\text{\AA}^2$, and $e_0 = 68 \text{ pN \cdot \AA}$ [157,158]. It should be noted that, before simulation of mechanical stretching, we have used the energy minimization to find the equilibrium conformation through steepest descent method. The 3 ~ 300 ns equilibration is performed with zero pulling force. The mechanical stretching of a protein is simulated from equation of motion, and then force-extension curve is obtained. The snapshots of conformations are generated using Visual Molecular Dynamics.

3.3. Results: Unfolding Mechanics

3.3.1. Case Study I: α -helix and β -hairpin

In Fig. 3.1, the structures of α -helix (PDB ID: 1akg, 17 residues) and β -hairpin (PDB ID: 1j4m, 14 residues) is presented. The unfolding simulation is performed by Brownian dynamic simulation with integration time step $\Delta t = 3 \text{ fs}$. In Fig. 3.2 (A), the force-extension curve of the stretching of α -helix with constant pulling speed is represented. The loading rate is $\dot{F} = 2.45 \times 10^{-1} \text{ N/s}$, and loading device stiffness is 0.04 N/m. Inset shows the carbon backbone structures corresponding

A



B

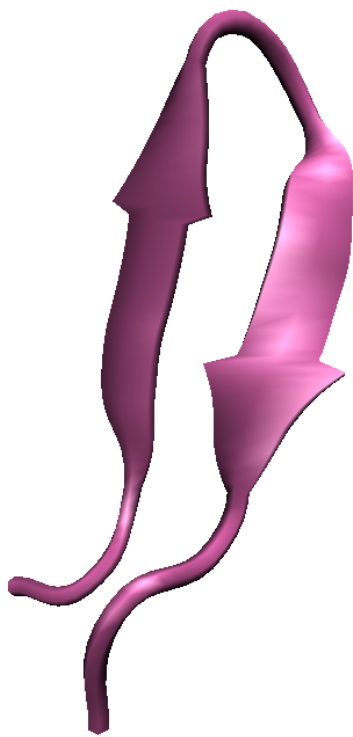


Fig. 3.1. The Cartoon of α -helix (A) and β -hairpin (B) which is generated by Visual Molecular Dynamics (VMD).

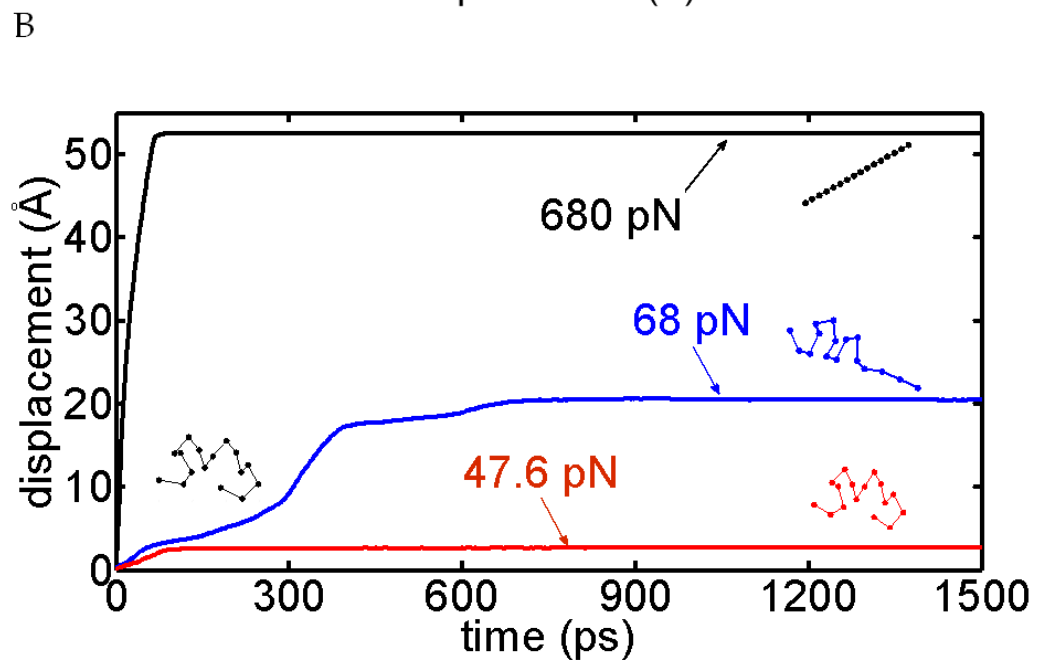
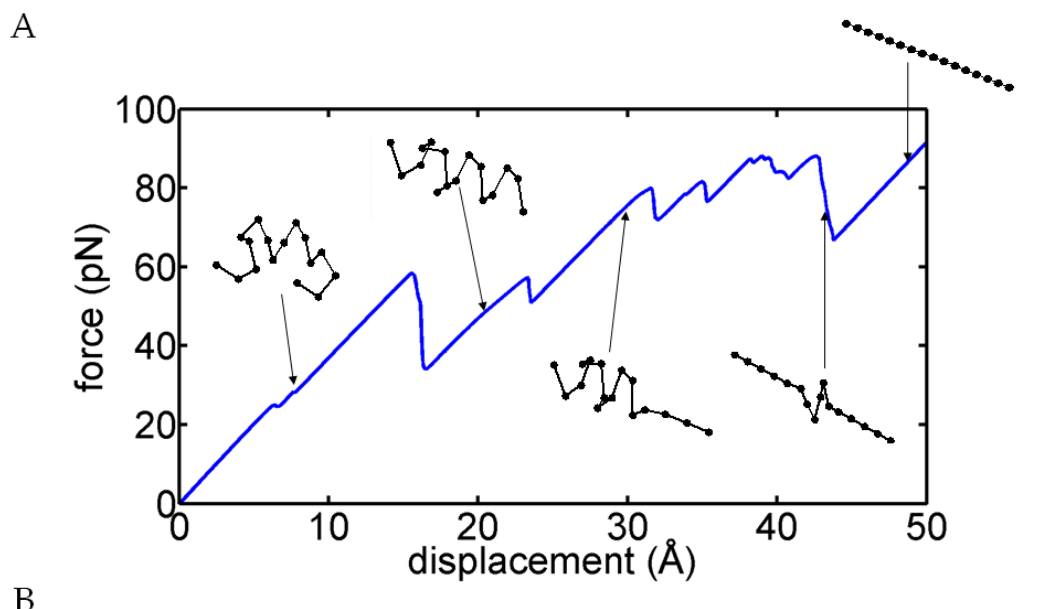


Fig 3.2. (A) The force-extension curve obtained by constant velocity pulling simulation. (B) The displacement-time curve obtained by constant force pulling simulation.

to force peaks. It is shown that force peak in saw tooth-like pattern indicates the rupture of hydrogen bonds in α -helix. Time-extension curve obtained from constant force (F) applied to both termini is in Fig. 3.2 (B). It is shown that, at very small force ($F = 47.6$ pN), the folding structure of alpha helix is unlikely to be unfolded. At $F = 68$ pN, the intermediate state of α -helix is observed at time 1500 ps, and no more unfolding occurs. At high force $F = 680$ pN, the fully unfolding has been observed for α -helix.

Fig. 3.3 (A) provides the representative curves for force vs. time for mechanical unfolding of β -hairpin. Furthermore, the snapshots in Fig. 3.3 (B) shows conformations for β -hairpin that is mechanically stretched with loading rate of $\dot{F} = 3 \times 10^{-3}$ N/s and different force constants (i.e. 0.01 N/m and 0.05 N/m) of loading device. Snapshots in Fig. 3.3 (B) provide that unfolding pathway is unaffected by force constant of loading device, which implies that different force-extension curves (i.e. Fig. 3.3 (A)) is not attributed to the unfolding pathway. That is, the unfolding pathway is purely determined by geometry of hydrogen bonds [159] but not by the loading device effect. It is interestingly found that force-extension relation is strongly dependent on force constant of loading device such that a force drop due to bond rupture is increasing when a stiff loading device is used, whereas force drop due to bond rupture is very small when a soft loading device is employed (see Fig. 3.3 (A)). This is ascribed to the hypothesis that mechanical stretching using very soft loading device is nearly equilibrium process. For protein unfolding using stiff loading device (i.e. force constant of 0.05 N/m), the significant force drops implies the noticeable energy dissipation, indicating that mechanical stretching using stiff device is under a non-equilibrium process.

In this stage, it is observed that the unfolding force of α -helix (~ 90 pN) is higher than that of β -hairpin (~ 80 pN), which is contrary to the existing

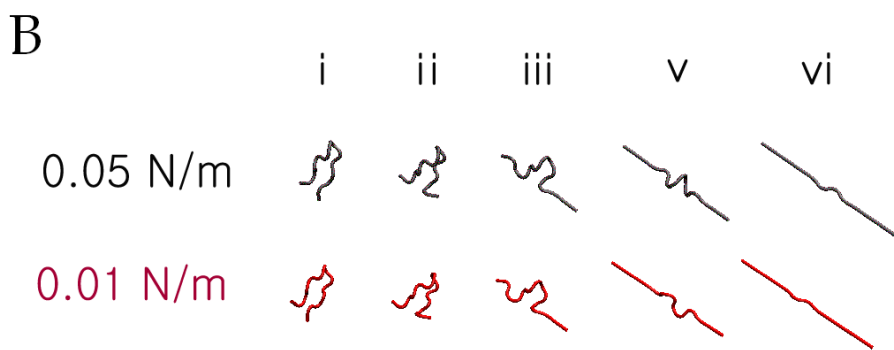
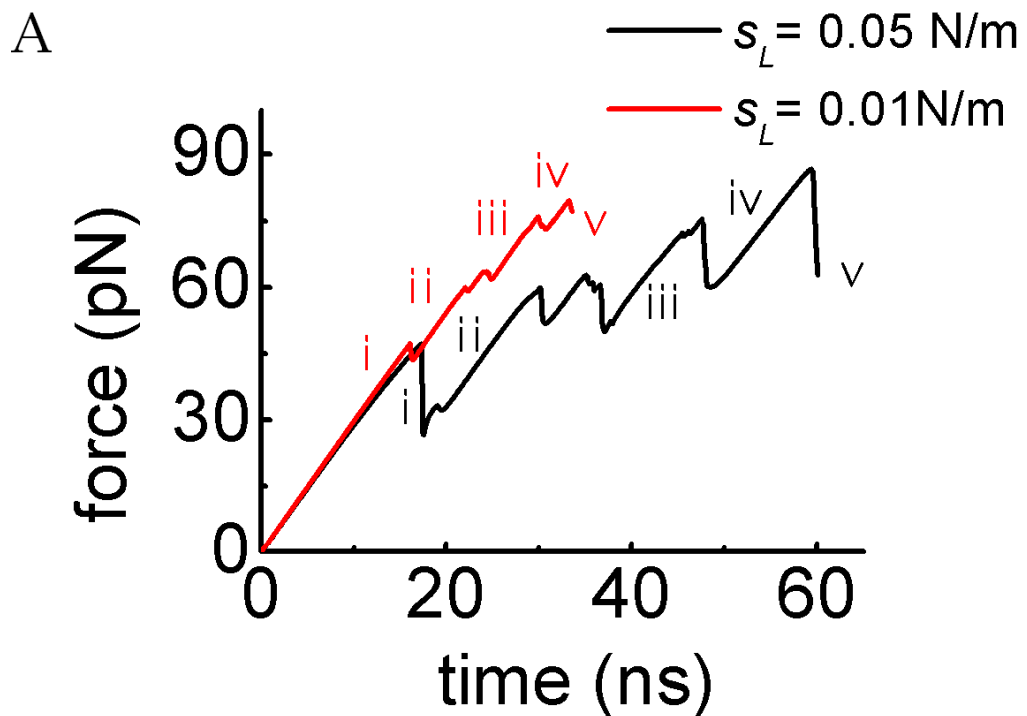


Fig. 3.3 (A) The force-extension curve of β -hairpin obtained by constant velocity pulling condition with two kinds of loading device stiffness. (B) The unfolding trajectory according the force-extension curve (The silver is $s_L = 0.05 \text{ N/m}$, and the red is $s_L = 0.01 \text{ N/m}$).

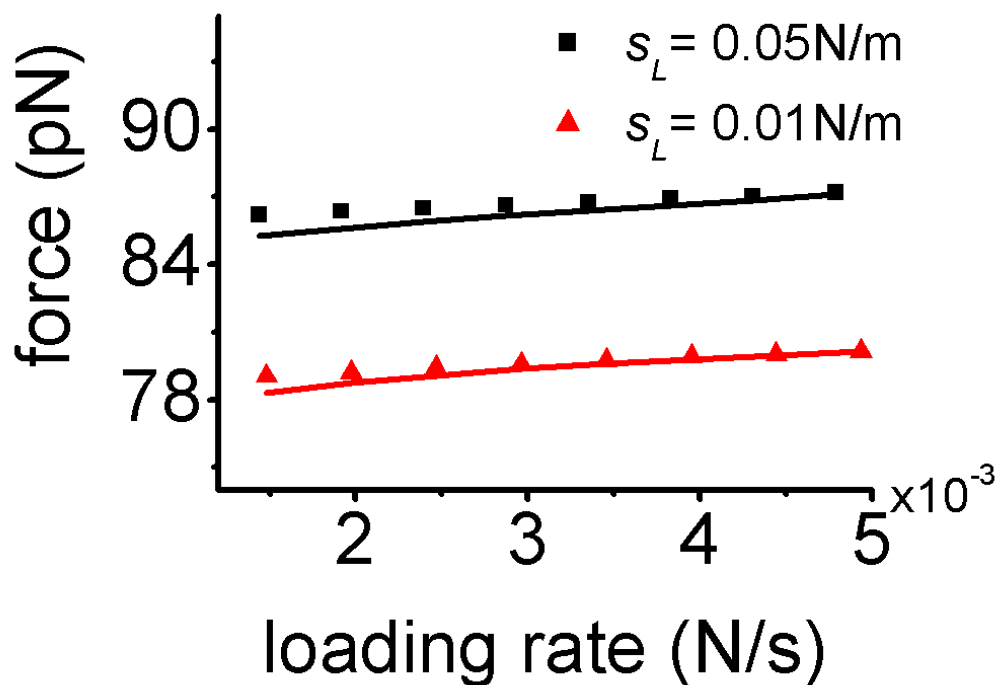


Fig 3.4. The unfolding forces with respect to loading rate and stiffness of loading device for β -hairpin unfolding. Here, solid line indicates the fitting to the theoretical model.

knowledge of the high mechanical strength of β -sheets. When the α -helix is unfolded in the direction of N-terminus to C-terminus, the hydrogen bonds experience tensile loading. But the hydrogen bond of β -sheet is perpendicular to the direction of β -strands, so the shear stress is applied to hydrogen bond in β -sheet when the N to C pulling is occurred in single molecule experiment [160]. Specifically, when the N to C pulling is applied to the β -hairpin, the hydrogen bonds experience the tensile stress like α -helix. And the structure of 1akg has disulfide bonds between the loop (C-terminus) and the end of α -helix (N-terminus) so the loops and the end of α -helix almost contact each other. Therefore it is one of the reasons for the higher mechanical strength of α -helix of 1akg than β -hairpin. Also, the loading rate for unfolding α -helix is larger than that of β -hairpin.

Moreover, Fig. 3.4 shows the unfolding forces of β -hairpin with respect to loading rate and force constant. Here, the unfolding force is measured as the peak force, at which a folded domain becomes to be fully denatured. It is found that loading device affects the unfolding force such that stiffer loading device increases the unfolding force. This is consistent with the theoretical anticipation based on simple two-state kinetic model using Kramers' theory with presumed one-dimensional free energy landscape introduced in section 2.2.1.C. The computational simulation results illustrate that protein unfolding mechanics is strongly dependent upon the stiffness of a loading device. The mean unfolding forces with respect to loading rate and the stiffness of loading device were well fitted to the theoretical model in Eq (2.8). Fig. 3.4 depicts the fitting parameters which are estimated as $k_0 \equiv \{D/(\Delta x_0)^2\}(3\Delta G_0/\pi k_B T) \exp(-\Delta G_0/k_B T) \approx 10^{-6} \text{ s}^{-1}$, $\Delta x_0 \approx 0.6 \pm 0.1 \text{ nm}$, and $\Delta G_0 \approx 0.08 \pm 0.01 \text{ nN nm}$. Unlike the rupture of chemical bond, the error in estimating the energy barrier ΔG_0 related to protein unfolding may

arise from the generic feature of free energy landscape such as its ruggedness.

3.3.2. Case Study II: Ubiquitin

The unfolding simulation of ubiquitin (PDB ID: 1ubq, 76 residues) is performed with integration time step $\Delta t = 300$ fs which satisfies the stability criterion of Brownian dynamics [143]. The harmonic spring is attached to both of N-terminus and C-terminus to mimic the AFM experimental condition (Fig. 3.5 (A)). In the Fig 3.5 (B), the unfolding force-displacement curve is presented, which exhibits saw-tooth patterns. The maximum unfolding peak (198 pN) happens at the displacement of 58.74 Å, and after that the unfolding forces diminish. At 160 Å of displacement, all native bonds ruptured. It can be verified by the unfolding trajectory (Fig. 3.6, 60 Å) that the blue and red β -strands rupture at the unfolding peak of 58.74 Å, which are parallel β -strands (See Fig 3.5 (A)). This unfolding pathway is comparable to the SMD simulational result for unfolding of ubiquitin [93]. But the unfolding force through SMD simulation is higher than the force with Brownian dynamics, because the pulling speed of SMD is higher than that of Brownian Dynamic simulation. After the rupture of parallel β -strands, the unfolding pathway is progressed to rupture between red and yellow β -strands which is parallel β -strands (Fig 3.6, 80 Å). The force peak and displacement can be confirmed at the force-displacement curve of Fig. 3.5 (B), 197 pN and 75 Å, respectively. In this stage, we can see the antiparallel β -configuration has higher mechanical stability than the parallel β -configuration. Finally, the α -helix (silver in Fig. 3.6) is unfolded at 110 Å, and the unfolding force is 175 pN which is lower than the rupture force of β -strands. Briefly, the order of mechanical stability can be identified by the unfolding force peak with unfolding pathway, that is antiparallel β -strands > parallel β -strands > α -helix.

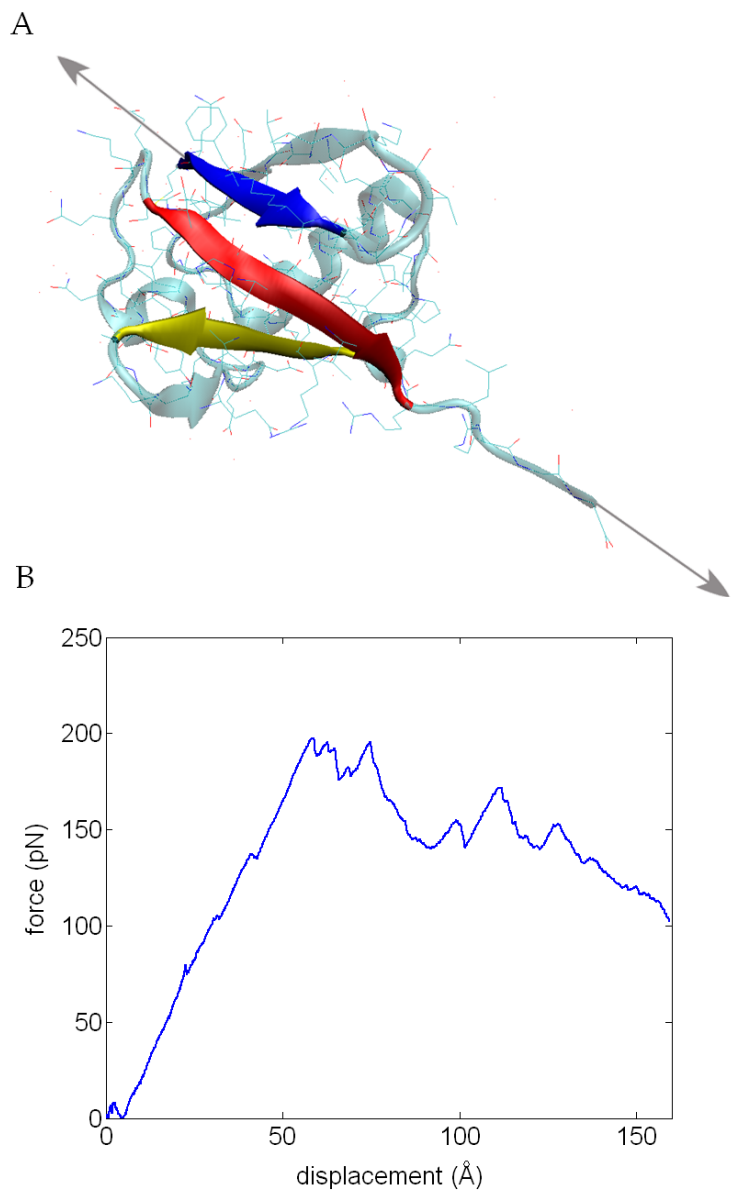


Fig 3.5 (A) N to C pulling condition for unfolding simulation of ubiquitin. The blue is $\beta 5$, red is $\beta 1$, and yellow is $\beta 3$ (B) The unfolding force-displacement curve of ubiquitin

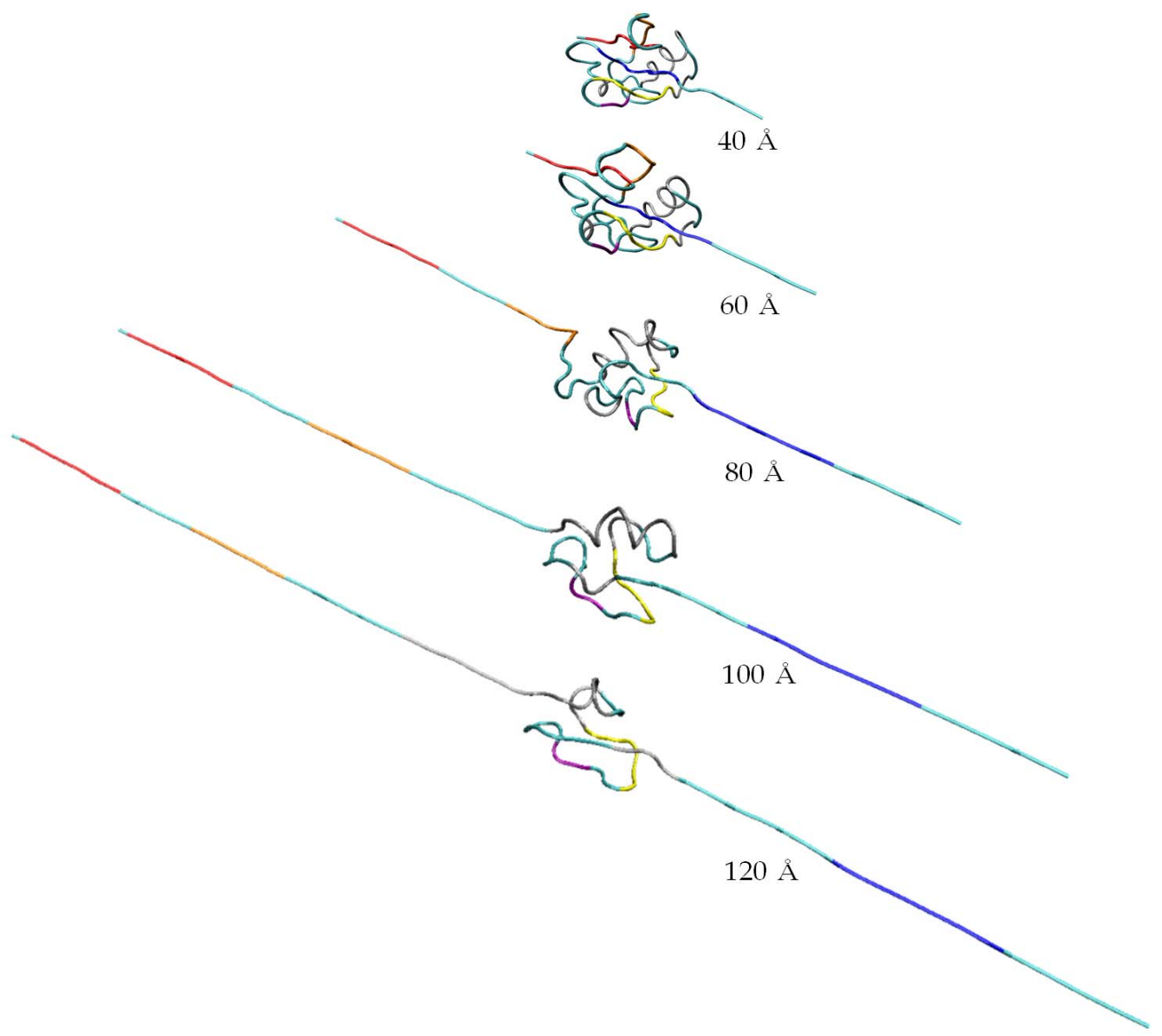


Fig 3.6 The unfolding pathway of ubiquitin corresponding to the force curve at Fig. 3.5 (B)

3.3.3. Anisotropic Unfolding Mechanics

To study the anisotropic mechanical characteristic of ubiquitin, 48-C pulling condition is applied. The unfolding peak occurs at the displacement of 60 Å of 171 pN where the native bonds between blue and yellow β -strands rupture. It is comparable to the SMD simulation result of unfolding pathway. Also, the unfolding force peak of 48 to C is lower than that of N-C (198 pN), which is similar to the result of AFM experiment and SMD [93]. The reason of lower unfolding force of 48-C pulling than N-C is that the parallel β -configuration ruptures first in the 48-C pulling. But the N-C pulling generates the native bond breaking of antiparallel β -configurations initially. After that, the antiparallel β -strands are ruptured at 70 Å. Moreover, there is no more native bond rupture after the displacement of 80 Å because all native bond are broken between 48th residue and C-terminus. The unfolding forces increase after 80 Å, because the non-breakable covalent chain is continuously stretched. At the force curve of N-C pulling for ubiquitin unfolding in Fig. 3.5 (B), the increasing unfolding force after all native bond breaking is trimmed after 160 Å of distance.

The unfolding pathway of ubiquitin is decided by the pulling residue; when the N-C pulling, the rupture sequence in the ubiquitin is antiparallel β -strands, parallel β -strands, and α -helix (See Fig. 3.6). The 48-C pulling condition generates the unfolding pathway; parallel β -strands and antiparallel strand (Fig. 3.8). Moreover, the rupture force of antiparallel β -strands is highest, that of parallel β -strands is next, and the unfolding force of α -helix is lowest. Because of random force characteristics of the Brownian dynamic simulation, the force curve is changed by iterative calculation, so it is needed to perform many times repetition of unfolding simulation to obtain the general unfolding pathway of ubiquitin.

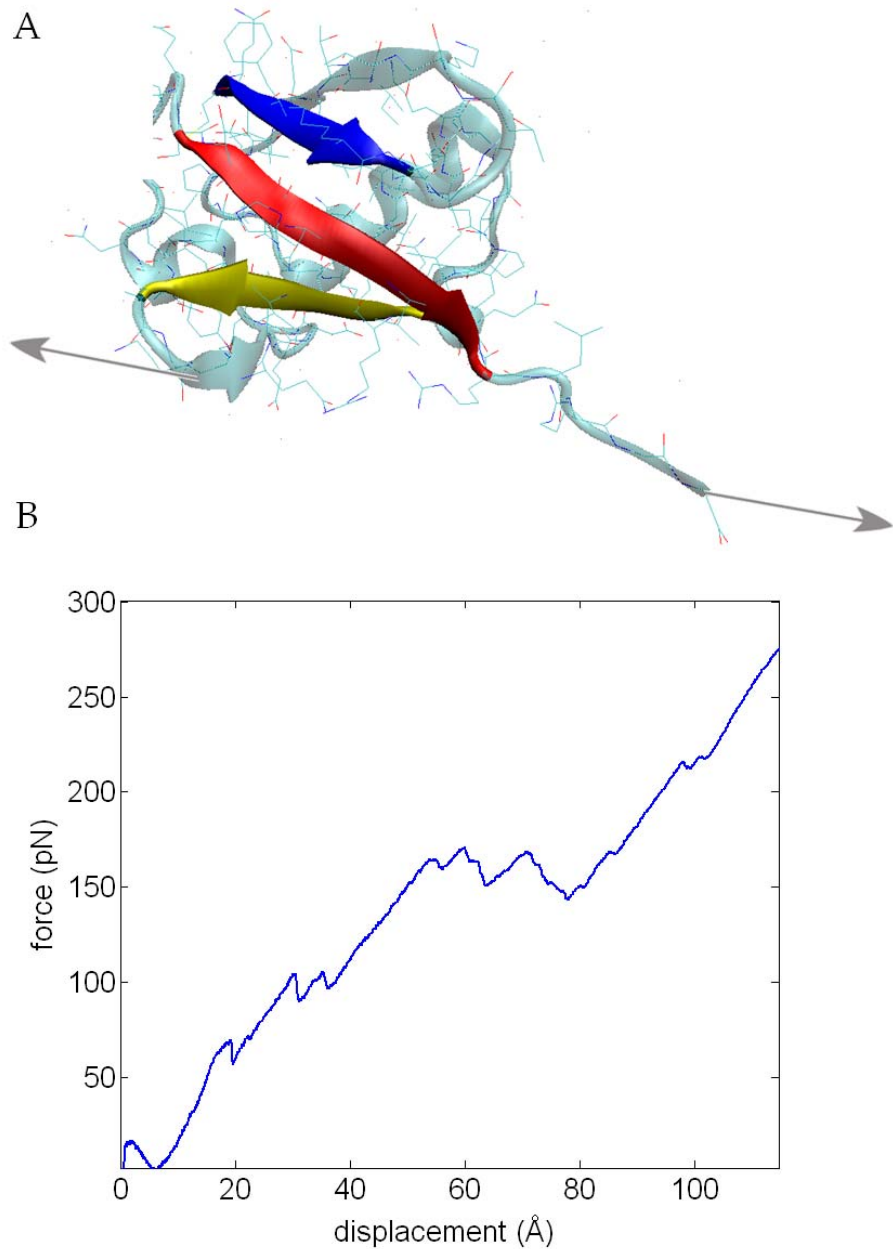


Fig 3.7 (A) 48 to C pulling condition for unfolding simulation of ubiquitin (B) The unfolding force-displacement curve of ubiquitin

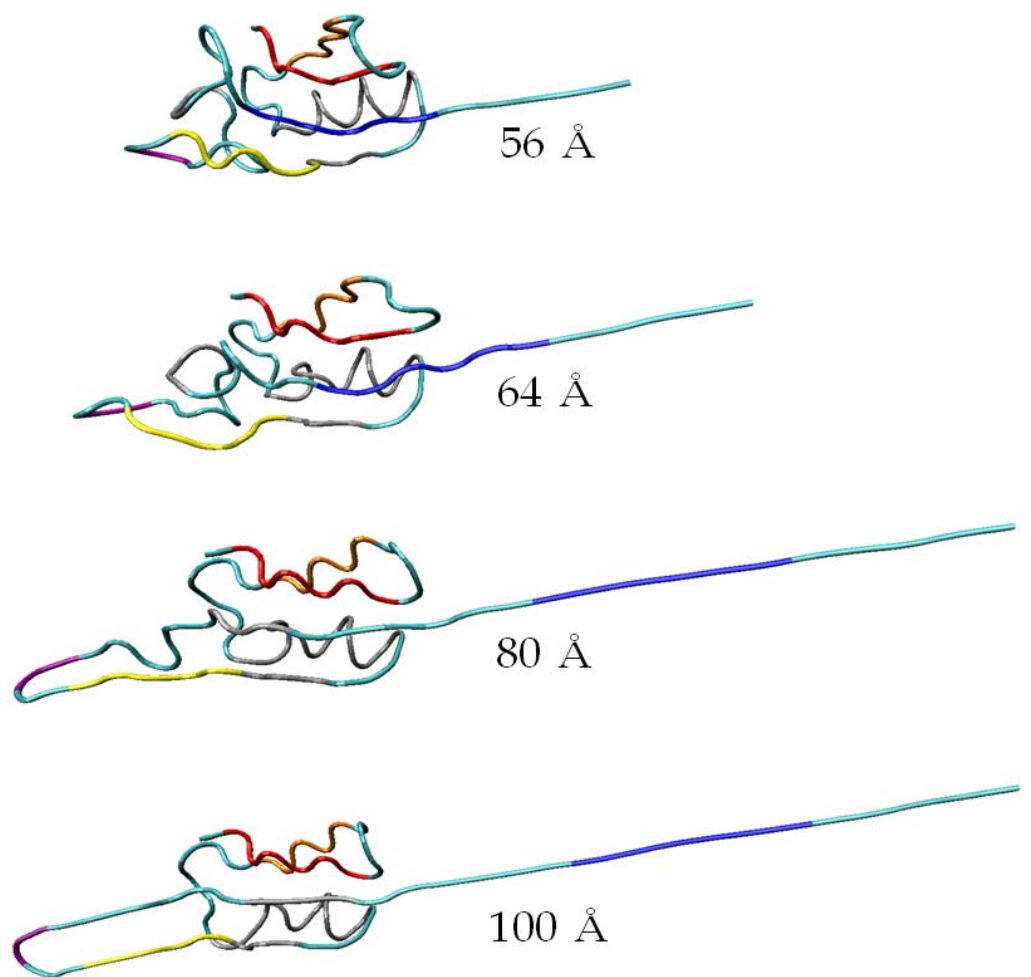


Fig 3.8 The unfolding pathway of ubiquitin corresponding to the force curve at Fig. 3.7 (B)

3.4. Summary

In this chapter, the unfolding of protein domains is studied using the Brownian dynamic simulation with Gō potential. The protein motif such as α -helix and β -hairpin is investigated to gain an insight to the origin of mechanical stability of protein. Especially, both of constant velocity and constant force pulling are applied to the unfolding of α -helix. In addition, the loading device effect in single molecule experiment is introduced with reaction rate theory in chapter 2 using unfolding force of β -hairpin. The unfolding force and pathway relationship of ubiquitin is elucidated. Finally, the anisotropic unfolding characteristic of ubiquitin is shown, which is comparable to the other results.

Chapter 4. Mechanical Properties of Protein Crystals

4.1. Introduction

The protein fibers which can be applied to the biomaterials such as spider silk fibers, exhibit over few μm length scales. There have been few literatures [88,161,162] on the characterization of macroscopic mechanical properties such as Young's modulus of biological materials such as protein crystals and fibers based on physical model such as atomistic model (e.g. molecular dynamics simulation) for protein crystal. Despite the ability of atomistic model to provide the macroscopic properties of protein crystals, the atomistic model has been very computationally restricted to small protein crystals. Although the molecular dynamic simulation is useful to characterize the mechanical properties of proteins, it cannot be used to analysis the large size's biomaterials for limitation of computation. The coarse-grained model with the Brownian dynamic simulation is not also suitable to be applied to demonstrate the mechanical behavior of protein fibers for a number of degree-of-freedoms.

In this chapter, the micromechanical model of protein fiber is introduced, which can represent efficiently the mechanical characteristics of protein materials. In this work, It is revisited that the Go model in order to characterize the macroscopic mechanical properties of biological protein materials composed of model protein crystals such as α -helix, β -sheet, α/β tubulin, titin Ig domain, etc. Specifically, the representative volume element (RVE) containing protein crystals in a given space group is applied for computing the atomic stress of RVE in response to applied microscopic constant strain. It is shown that the micromechanical model based on Go model has allowed for estimation of the microscopic mechanical properties such as Young's modulus for protein crystals,

quantitatively comparable with experimental results and/or atomistic simulation results. Moreover, the micromechanical model enables us to understand the structure–property relationship for protein crystals. The role of molecular structure on the microscopic mechanical properties for protein crystals has also been discussed. It is provided that, from our simulation, the native topology of protein structure is key factor to present the mechanical behaviors of protein crystals.

4.2. Methods

4.2.1. Micromechanics model

The mechanical behavior of protein fibrils can be presented by unitcell which allows the periodic boundary condition of crystallography in Fig. 4.1. The protein in the RVE obeys the specific space group at each case of protein. When the fibril experience the longitudinal deformation due to tensile loading, the RVE and/or unitcell is stretched as hydrostatic strain which is 3-axial strain refered to volumetric strain (e) of unitcell.

$$e = \frac{1}{3}(\varepsilon_{xx} + \varepsilon_{yy} + \varepsilon_{zz}), \quad (3.1)$$

where ε_{xx} , ε_{yy} , ε_{zz} is nominal strains in the direction of x, y, z respectively. The strain increases gradually from 0 to 0.2 in the step of $\Delta\varepsilon = 0.001$ for stretching the unitcell. For calculating the stress of deformed unitcell, the position of proteins after application of strain in the unitcell (\mathbf{r}^*) should be obtained,

$$\mathbf{r}^* = \mathbf{r} + \mathbf{u}(\mathbf{r}), \quad (3.2)$$

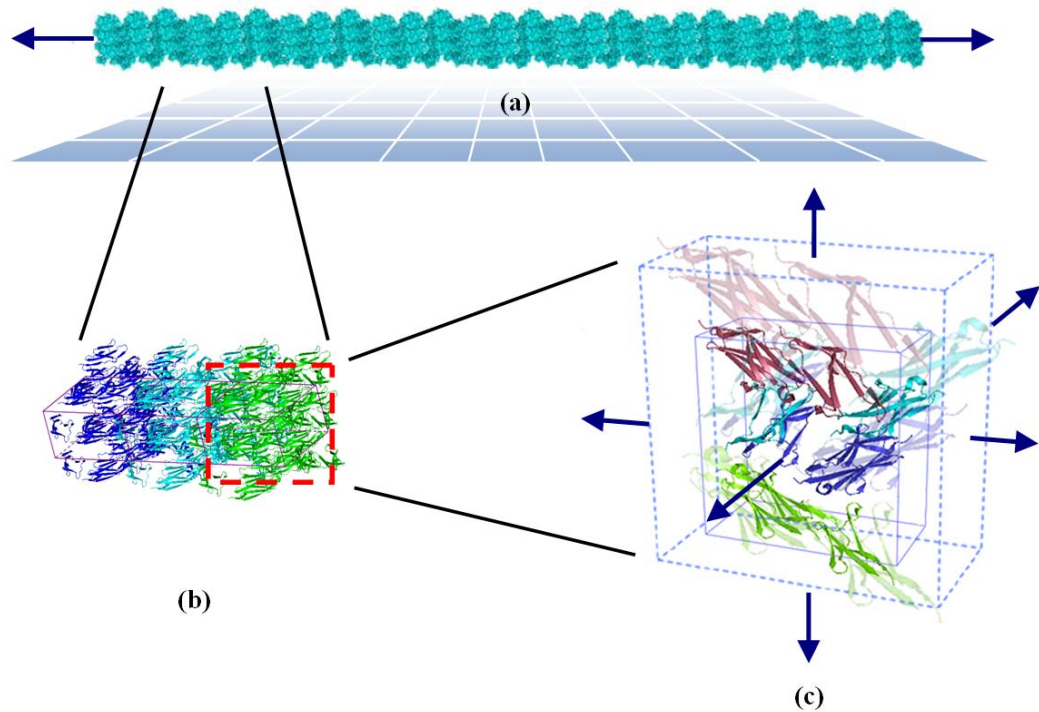


Fig. 4.1. The hierarchical structure of protein fibril represented periodically repeated unitcell. Figure reproduced with permission from Ref. [157], © 2008 Wiley Periodicals, Inc.

here, \mathbf{r} is position vector of proteins in unitcell, $\mathbf{u}(\mathbf{r})$ is the displacement vector due to strain $\Delta\epsilon$, $\mathbf{u}(\mathbf{r}) = \Delta\epsilon \cdot \mathbf{r}$.

In this research, the pulling speed of the fibril is too slow so the proteins maintain their equilibrium state, which regarded as a quasi-equilibrium pulling process. [159,163] To find the equilibrium position of proteins in unitcell, the energy minimization process is performed with steepest descent method,

$$\mathbf{r}_k = \mathbf{r}_{k-1} + \lambda_k \mathbf{s}_k. \quad (3.3)$$

Here, subscript k is iteration number, λ_k is step size, and \mathbf{s}_k is unit vector represents descent direction, $\mathbf{s}_k = \mathbf{F} / |\mathbf{F}|$ where \mathbf{F} is internal force of protein obtained by the negative gradient of the potential (V), $\mathbf{F} = -\nabla V$. The volumetric stress σ for a unitcell can be calculated by Virial stress theorem which presents the atomic stress [76,160,164],

$$\sigma = \frac{1}{V} \sum_{i=1}^N \sum_{j \neq i}^N \frac{1}{2} \mathbf{r}_{ij} \otimes \left(\mathbf{r}_{ij} \frac{\partial V(\mathbf{r}_{ij})}{\partial \mathbf{r}_{ij}} \frac{1}{r_{ij}} \right), \quad (3.4)$$

V is the volume of RVE, $\mathbf{r}_{ij} = \mathbf{r}_i - \mathbf{r}_j$ which \mathbf{r}_i , \mathbf{r}_j is position vector of i^{th} and j^{th} C_α atom, and \otimes is tensor product.

4.2.2. Inter-atomic potential

The potential field in this research is used to Gō potential (Eq. 3.2) which is introduced in section 3.2.

4.3. Results

4.3.1. Elastic properties of Protein Crystals

The stress-strain curve of several protein crystals is presented at Fig. 4.2. In general, the stress-strain relationship for polymer materials including protein materials obeys the nonlinear elastic behavior. The tangent modulus as the elastic modulus (E) is estimated such as $E = \partial\sigma / \partial e$ at zero strain [165,166]. First of all, the Young's modulus of tubulin (1tub, space group: P2₁) is obtained to 0.138 GPa which is comparable to the experimental result. The AFM bending experiments of microtubule results the Young's modulus $E = \sim 0.1$ GPa, which is affected by the temperature [101]. But another experimental result, $E = \sim 2.5$ GPa, which is obtained by nondestructive method, is different from the elastic modulus estimated by micromechanical model, because the fiber length can be related to the bending rigidity [167]. Moreover, the elastic modulus and maximum stress of β -sheet (2zona, P₁) is larger than those of α -helix (1akg, P2₁2₁2₁). It accords with the result of single molecule experiment of ubiquitin in chapter 3 shows the unfolding force of β -strands (197 - 198 pN) is larger than that of α -helix (175 pN) in Fig. 3.5 (B). The excellent mechanical property such as maximum stress (σ_{\max}) of β -sheet among other protein crystals agrees with previous studies which reported that β -sheet plays a vital role on the mechanical property of protein such as silk protein [7], muscle protein [8], and amyloid fibrils [39]. It is also compared the mechanical property of proximal Ig domain (1g1c, P2₁2₁2₁) and distal Ig domain (1waa, P2₁2₁2₁) of titin. In the experimental result using AFM suggest that the distal Ig domain exhibits higher unfolding force than proximal Ig domain [14], and the simulation result in this research shows similar results; Young's modulus of distal Ig domain (0.254 GPa) is larger than that of proximal Ig domain (0.187 GPa).

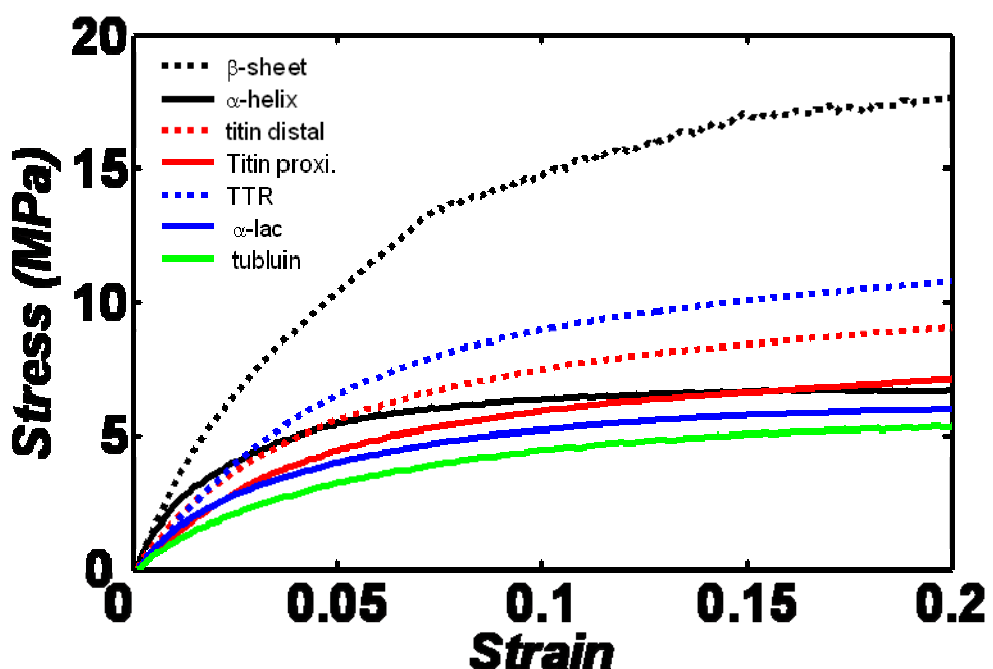


Fig. 4.2. The stress-strain relation of various protein crystals. Here, titin distal is distal Ig domain of titin, titin prox. is the proximal Ig domain of titin, TTR is transthyretin, and α -lac is α -lactalbumin. Figure reproduced with permission from Ref. [157], © 2008 Wiley Periodicals, Inc.

Table 4.1. Elastic property of protein crystals. Table reproduced with permission from Ref. [157], © 2008 Wiley Periodicals, Inc.

Protein (PDB ID)	Cell parameter			Elastic modulus		Maximum stress (MPa)	contact number (%)	Contact order (%)
	Space Group	No. of residue in unit cell	Unit cell volume (\AA^3)	<i>in silico</i>	<i>in vitro</i>			
α -helix (1akg)	P2 ₁ 2 ₁ 2 ₁	64	14.6×26.1×29.2	0.277	-	3.82	45.0	24.0
β -sheet (2zona)	P ₁	24	25.8×9.7×15.8	0.433	-	5.69	30.1	24.5
α -lactalbumin (1hfz)	P2 ₁	982	38.3×78.6×79.6	0.186	2	2.45	1.75	2.14
Transthyretin (2g5u)	P2 ₁ 2 ₁ 2	908	62.2×75.9×134.2	0.242	5	3.48	4.05	9.34
Titin								
proximal Ig (1g1c)	P2 ₁ 2 ₁ 2 ₁	640	58.6×60.1×77.1	0.187	-	2.36	5.13	10.26
Titin distal								
Ig (1waa)	P2 ₁ 2 ₁ 2 ₁	2208	43.2×85.8×64.7	0.254	-	10.8	1.61	4.44
Tubulin (1tub)	P2 ₁	1734	80×92×90	0.138	0.1~2.5	1.87	1.13	3.99
f-Actin								
rabbit								
skeletal muscle (1rfq)	P4 ₃	2888	101.5×101.5×104.2	0.166	2.2	2.19	1.26	3.86

Con't

β -lactoglobulin (1BEB)	P ₁	312	37.8×49.5×56.6	0.166	5	2.37	2.90	7.41
Lysozyme (194L)	P ₄₃₂₁₂	1032	78.65×78.65×37.76	0.143	5	7.21	6.77	9.16
Collagen (1k6f)	P ₂₁₂₁₂₁	696	26.91×26.36×182.50		~2		6.06	15.5
Fn3 (a) (1fnα)	P ₂₁	182	30.70×35.10×37.70	0.294	-	3.90	9.21	17.5
Fn3 (b) (1fnf)	P ₂₁	1472	64.05×60.67×58.44	0.239	-	3.36	2.43	5.10
Fn3 (c) (1fnh)	I2 2 2	2152	68.58×86.29×142.80	0.189	-	2.68	3.33	7.07
FN3 (d) 1ten	P ₄₃₂₁₂	712	49.78×49.78×71.04	0.307	-	4.12	8.81	18.6
Titin N-ter (2a38)	P1	582	55.41×56.29×74.41	0.177	-	2.40	1.54	4.05
Equine cyt c (1hrc)	P ₄₃	416	58.40×58.40×42.09	0.365	-	4.87	7.47	10.8
Ubiquitin (1ubq)	P ₂₁₂₁₂₁	304	50.84×42.77×28.95	0.532	-	7.1	10.2	16.6
CspB (1csp)	P ₃₂₂₁	402	58.94×58.94×46.45	0.315	-	4.2	11.5	17.6

4.3.2. Role of Folding Topology in Mechanical Properties of Protein Crystals

For understand the relation of mechanical property and the topology of protein, the dimensionless quantity Q (degree-of-fold) is introduced,

$$Q = \frac{N_c}{N_m}, \quad (3.5)$$

here, N_c is the number of native contacts exist in the cut-off distance (7.5 \AA), and maximum possible number of native contacts $N_m = N(N-1)/2$ where N is the number of residues in an unitcell. The degree-of-fold is almost identical to contact order which is typically used to represent the folding of protein [168]. The Fig. 4.3 shows the high correlation of Q and E of 20 kinds of model proteins; E increases when Q increases except α -helix and β -sheet for so much of Q (30 for β -sheet and 45 for α -helix). N of α -helix and β -sheet are 64 and 24, respectively which is too small to compare with other protein crystals (N are from 300 to 3000) in the aspect of Q . Moreover, the relation between Q and σ_{\max} (maximum stress) is shown in Fig. 4.4. Alike the relation of Q and E , σ_{\max} increases with increment of Q under 20 %. σ_{\max} of all kinds of protein crystals are not over 10 MPa except that of distal Ig domain of titin. In this stage, it can be verified that titin Ig domain is designed to perform the mechanical function in muscle for its excellent mechanical property.

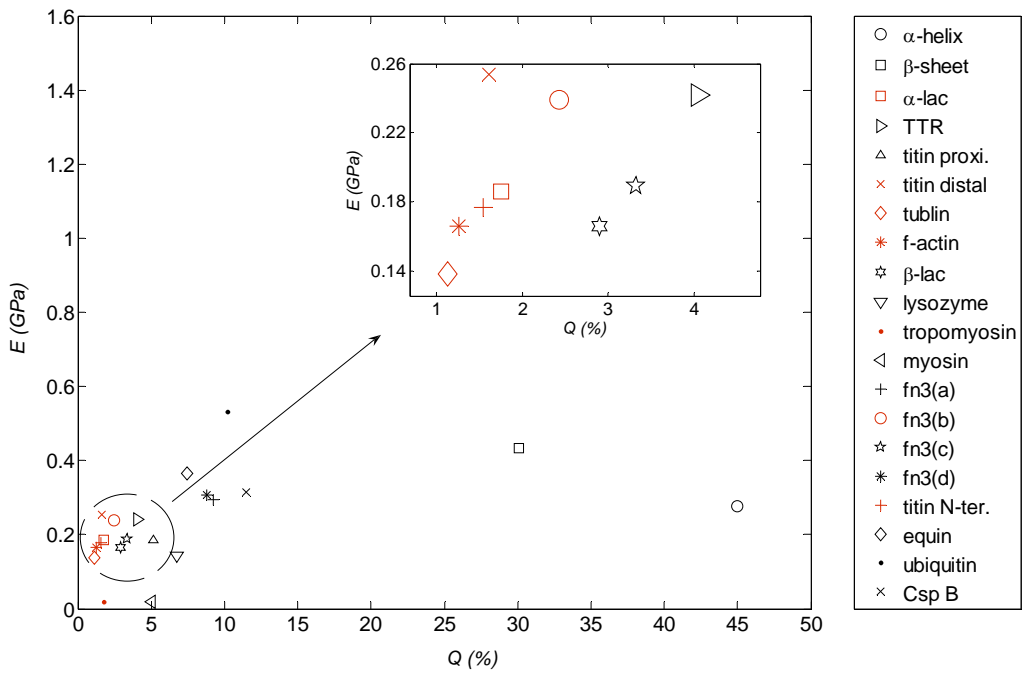


Fig. 4.3. Relationship between Young's modulus of biological protein materials and degree-of-fold Q. Figure reproduced with permission from Ref. [157], © 2008 Wiley Periodicals, Inc.

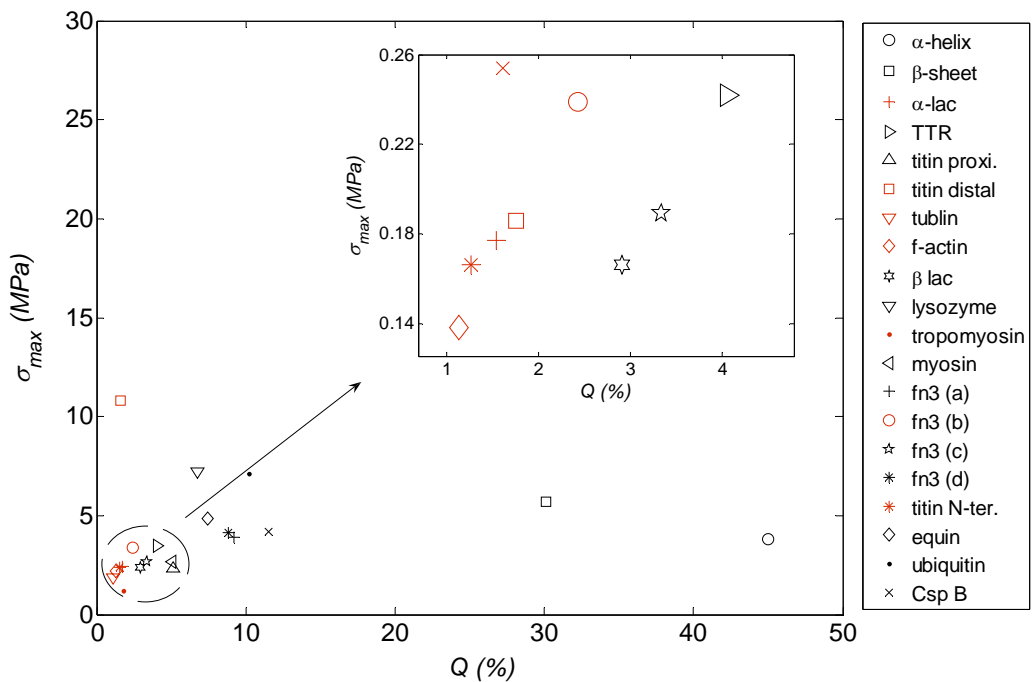


Fig. 4.4. Relationship between maximum hydrostatic stress of protein materials and degree-of-fold Q . Figure reproduced with permission from Ref. [157], © 2008 Wiley Periodicals, Inc.

4.4. Summary

In this chapter, the microscopic model of biological protein materials made of protein crystals is suggested based on Go model with virial stress theory. The stress-strain relation of many kinds of model proteins is presented. It is shown that this model enables the quantitative predictions of the mechanical properties (e.g. Young's modulus) for biological protein materials, quantitatively and/or qualitatively comparable with AFM experimental result. More remarkably, the structure-property relation for protein materials is observed by degree-of-fold, Q , which is represented that the folding topology plays a vital role on both Young's modulus and maximum stress. The native topology of protein is important factor to represent the mechanical behavior of protein materials.

Chapter 5. Mechanical Characterization of Disease-Related Protein Fibers

5.1. Introduction

Denatured proteins in the tissues of human body can cause fatal diseases such as Alzheimer's disease, Parkinson's disease and so on [28,47]. The Alzheimer's amyloid β peptide forms long and highly aggregated fibrils that results from self-assembly and self-propagation of degenerated proteins in the human brain [48]. The amyloid fibril is also founded at the pancreas of the type II diabetes, called human islet amyloid polypeptide (hIAPP), which is crucial factor of insulin-secreting inhibition [169]. Especially, the hIAPP₂₀₋₂₉ (SNNFGAILS) is believed that forms part of the amyloidogenic core for assemblies of fibrils replacing insulin-secreting β -cells at the islet of pancreas. In recently years, the supramolecular structure of the NFGAILS section of the hIAPP₂₀₋₂₉ fibrils is presented by solid-state NMR, which is long and helical amyloid fibrils consist multi-layers' ladder-shape assembled β -strands, called cross- β amyloid [32].

Structural characteristics of amyloid fibril have been investigated in decades for elucidating aggregation mechanism of proteins [53,170]. Recently, hierarchical helical structure of amyloid fibrils is imaged by atomic force microscopy for β -lactoglobulin fibrils [41], which has the linear relationship between helical periodicity or fibril length, and number of filaments or fibril thickness. Alzheimer's A β ₁₋₄₀ has twofold and threefold fibrillar morphologies about the fibril growth axis are suggested by molecular modeling compared with TEM images [31]. The X-ray diffraction patterns obtained from amyloid fibrils can show diverse architecture of cross- β amyloid [55,171], which can be varied

though they consist same sequences. For instance, $\text{A}\beta_{1-40}$ forms parallel β -sheet but $\text{A}\beta_{34-42}$ does antiparallel β -sheet, the fibril of Sup35 (Q- and N- rich peptide) is parallel structure but antiparallel fibril is suggested for thermodynamic stability and *de novo* designed structure [58]. Also, hIAPP₂₀₋₂₉ is antiparallel hetero fibril but in another experimental condition, parallel homo fibril is found [57].

Mechanical characterization for single molecules shed light on the structural and functional relation of biological molecule in biological system, as well as remarkable mechanical properties of protein materials [172-174]. The superelasticity and high fracture toughness of spider silk fibril is observed by mechanical stretching experiment using atomic force microscopy (AFM) [3]. Also, bending test of insulin amyloid fibril by AFM can show the Young's modulus of few GPa comparable to that of silk [99] and the bending rigidity of diverse types of amyloid fibril is studied by AFM images of shape fluctuation, from 10^{-25} Nm^2 to 10^{-24} Nm^2 [37]. But mechanical characterization of hIAPP has not been performed yet though the pathological importance in diabates. Also, detail deformation mechanism of biological fibrils can be observed by molecular dynamic (MD) simulation for stretching and bending test [7,175]. Especially, normal mode analysis (NMA) is powerful method for characterization of all possible structural deformation modes such as bending, twisting and stretching mode. However, it is hard to analysis full length scale (hundreds nanometers) amyloid fibril for limitation of computational cost of MD.

Elastic network model (ENM) is coarse-grained approach for computational efficiency to describe dynamic behavior of low frequency collective motion of proteins, first suggested by Tirion and later by several groups, regards the protein structure as a harmonic spring network [176-178]. Large protein's dynamic behavior such as conformational changes of molecular chaperonin, GroEL/GroES can be estimated by ENM [20]. Also, ENM can describe the

mechanical behavior for biological molecule, the atomic stress-strain relation for protein crystals are introduced [157] and full length scale of microtubules' [179], A β amyloid fibrils' mechanical properties are proposed by ENM, which is comparable to AFM experimental data [39].

In this work, we revisit the ENM in order to characterize the mechanical properties of amyloid fibril of hIAPP and describe dynamic behavior and fibril morphology relationship for gain insight of protein aggregations. Especially, the possible four classes of cross- β amyloid of hIAPP is considered, parallel/homo(and/or face-to-face), parallel/hetero(and/or face-to-back), antiparallel/homo and antiparallel/hetero. (See Fig. 6.1) NMA is performed for obtain dominant deformation modes and the bending rigidity, shear modulus and Young's modulus is calculated by applying continuum model.

5.2. Theory and Methods

5.2.1. Continuum Mechanics Model

5.2.1.A. Euler-Bernoulli Beam Model

The mechanical property of the fibril can be obtained by continuum model [180]. Euler-Bernoulli beam model is flexural vibration model of beam. The equation of motion is

$$\frac{\partial^2 w(x,t)}{\partial t^2} + c_b^2 \frac{\partial^4 w(x,t)}{\partial x^4} = 0, \quad c_b = \sqrt{\frac{EI}{\rho A}}. \quad (5.1)$$

Here, time is t , position along the fibril is x , w is transverse displacement of the fibril, EI is bending rigidity and ρA is atomic mass density per fibril length L . The

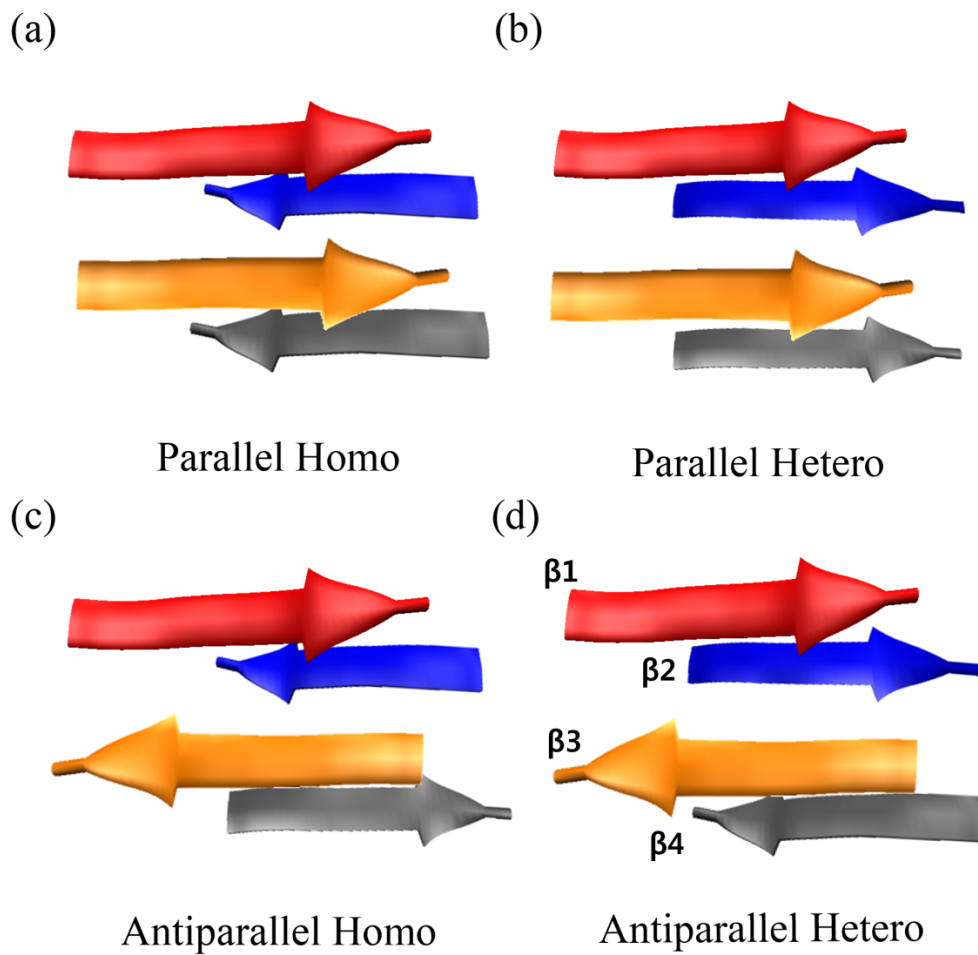


Fig. 5.1. Four cases of cross- β hIAPP fibril. Figure reproduced with permission from Ref. [181], © 2011 Wiley Periodicals, Inc.

natural frequency (ω_n^b) and mode shape (W_n) can be derived by free end-free end boundary condition, that is bending moment and shear force is zero at each end, $EI\partial^2w/\partial x^2 = 0$ and $\partial [EI\partial^2w/\partial x^2]/\partial x = 0$

$$\omega_n^b = \beta_n^2 \sqrt{\frac{EI}{\rho A}}, \quad (5.2a)$$

$$W_n(x) = \cosh \beta_n x + \cos \beta_n x - \sigma_n (\sinh \beta_n x + \sin \beta_n x), \quad (5.2b)$$

where $\beta_n L = 4.37$, $\sigma_n = 0.98$, at $n = 1$ (fundamental mode).

Torsional vibration of bar is

$$\frac{\partial^2 \theta(x,t)}{\partial t^2} - c_t \frac{\partial^2 \theta(x,t)}{\partial x^2} = 0, \quad c_t = \sqrt{\frac{G}{\rho}}. \quad (5.3)$$

Here, θ is torsional angle, G is shear modulus, ρ is density. The torsional natural frequency (ω_n^t) and mode shape (Θ_n) is

$$\omega_n^t = \frac{n\pi c_t}{L}, \quad (5.4a)$$

$$\Theta_n(x) = \cos \frac{n\pi x}{L}, \quad (5.4b)$$

when torque is zero at each end, $GJ\partial\theta/\partial x = 0$, J is polar moment of inertia $J = bh(b^2+h^2)/12$, b and h is width and height of cross-section of the fibril, respectively.

The equation of motion of longitudinal vibration of rod is

$$\frac{\partial^2 y(x,t)}{\partial t^2} + c_s^2 \frac{\partial^2 y(x,t)}{\partial x^2} = 0, \quad c_s = \sqrt{\frac{E}{\rho}}. \quad (5.5)$$

Here, y is longitudinal displacement of rod, E is young's modulus. The stretching natural frequency (ω_n^s) and mode shape (Y_n) is

$$\omega_n^s = \frac{n\pi c_s}{L}, \quad (5.6a)$$

$$Y_n(x) = \cos \frac{n\pi x}{L}, \quad (5.6b)$$

when zero stress boundary condition at each end, $EA\partial y / \partial x = 0$, A is cross-section area of the fibril.

5.2.1.B. Timoshenko Beam Model

The Timoshenko beam model can be applied to the bending deformation of amyloid fibrils that the theoretical model of bending deflection of beam when the beam is simply supported and applied concentrated load P at the center for study of shear effect in bending. The deformation of the beam at the center is [98]

$$\delta = \delta_b + \delta_s = \frac{PL^3}{48EI} \left(1 + \frac{12\alpha_s EI}{GAL^2} \right) \quad (5.7)$$

Here, δ_b is bending deformation and δ_s is shear deformation, α_s is shear coefficient, $\alpha_s=3/2$ at the rectangular cross section of the beam, EI is bending rigidity when the shear effect is considered, G is shear modulus for bending deformation. The second term in Eq. (5.7) is the effect of shear effect ($\varphi_s = 12\alpha_s EI / (GAL^2)$) in

bending deflection, the effect of shear reduced with square of beam length (L^2). If the shear effect ignored, the bending deformation is $\delta = PL^3 / 48EI$. To obtain the relation of bending rigidity and the length of beam, substitute this equation to Eq. (5.7),

$$EI = \bar{EI} \left(1 + \frac{12\alpha_s \bar{EI}}{\bar{G}AL^2} \right)^{-1}. \quad (5.8)$$

5.2.2. Coarse-Grained Model

5.2.2.A. Structure Model of Protein Fibers

The structural information of hIAPP₂₀₋₂₉ (NFGAILS) fibril is deposited in PDB (ID: 2KIB) which is identified by standard 2D NMR spectra. It is antiparallel hetero configuration (Fig. 6.1 (d)), so the other three configurations, such as parallel homo, parallel hetero and antiparallel homo, should be derived from symmetry of β strand in the 2kib. That is, the sequence of the β strand is changed from NFGAILS to SLIAGFN. For example, the antiparallel homo configuration can be obtained by sequence change of β 2 and β 4 shown in Fig. 6.1 (c). The distance between two β -strand along fibril axis is 4.87 Å and perpendicular to fibril axis is 10.52 Å can be obtained from 2kib. The hIAPP₂₀₋₂₉ fibril has twisted structure along fibril axis, its helical pitch is 25.811 nm and there are 72 β -strands in one helical pitch of the fibril [32]. In this information, the full length fibril can be constructed by twisting and repeating of the initial configurations which are constructed above. First, the initial β -strands configuration rotated 20° round fibril axis and then, it is pasted below the initial β -strands configuration and these processes are repeated until one pitch fibril is finished. The full length fibril can be obtained by repeat of the one pitch fibril.

5.2.2.B. Elastic Network Model

The stiffness matrix for normal mode analysis shows the vibration characteristics can be obtained by the elastic network model (ENM). ENM assumes that residue is represented by an atom, and residues in neighbor are connected with harmonic spring with equal force constant. Despite its simplicity, ENM is very robust with calculating protein fluctuation, because ENM is sufficient with describing protein topology which plays important role in protein dynamics. The potential field V for ENM is given by,

$$V = \frac{\gamma}{2} \sum_{i=1}^N \sum_{j \neq i}^N \left[|\mathbf{r}_i - \mathbf{r}_j| - |\mathbf{r}_i^0 - \mathbf{r}_j^0| \right]^2 \cdot H(r_c - |\mathbf{r}_i^0 - \mathbf{r}_j^0|) , \quad (5.10)$$

where γ is a force constant of a harmonic spring, N is the total number of residues, \mathbf{r}_i is the coordinates of i^{th} residue (alpha carbon atom), r_c is a cut-off distance, $H(x)$ is the Heaviside unit step function defined as $H(x) = 0$ if $x < 0$; otherwise $H(x) = 1$, and superscript 0 indicates the equilibrium conformational state. Here, $\gamma = 100$ kcal mol⁻¹Å⁻², $r_c = 12$ Å is applied to construct ENM.

For implementation of NMA, the stiffness matrix has to be computed from a potential field given by Eq. (5.10). The stiffness matrix \mathbf{K} is composed of 3×3 block matrices \mathbf{K}_{ij} given as

$$\mathbf{K}_{ij} = - \left[\gamma H(r_c - |\mathbf{r}_i^0 - \mathbf{r}_j^0|) \frac{(\mathbf{r}_i^0 - \mathbf{r}_j^0)^T (\mathbf{r}_i^0 - \mathbf{r}_j^0)}{|\mathbf{r}_i^0 - \mathbf{r}_j^0|^2} \right] \times (1 - \delta_{ij}) - \delta_{ij} \sum_{r \neq i}^N \mathbf{K}_{ir} . \quad (5.11)$$

Here, δ_{ij} is the Kronecker delta defined as $\delta_{ij} = 1$ if $i = j$; otherwise $\delta_{ij} = 0$,

and $(\cdot)^T$ represents the transpose of vector.

NMA assumes that protein motion is described by harmonic motion near equilibrium state. Equation of motion for protein dynamics is given as $\mathbf{M}(\ddot{\mathbf{x}}) + \mathbf{K}\mathbf{x} = 0$, where \mathbf{M} is mass matrix (i.e., diagonal matrix) and \mathbf{K} is the stiffness matrix given by $\mathbf{K} = \partial_x \partial_x V$, where ∂_x is the gradient with respect to coordinates x . Atomic coordinates can be assumed as $\mathbf{x} = \mathbf{u} \exp[i\omega t]$ with natural frequency ω and its corresponding normal mode \mathbf{u} . The equation of motion can be described by an eigen-value problem as follows : $\mathbf{K}\mathbf{u} = \omega^2 \mathbf{M}\mathbf{u} = \lambda \mathbf{u}$, where λ is the eigenvalue.

The three dominant modes, bending, twisting and stretching mode, can be identified by mode shape \mathbf{x}_u^b and \mathbf{x}_u^t and \mathbf{x}_u^s of the fibril excluding six rigid body modes. Here $\mathbf{x}_u^b = \mathbf{x} + a\mathbf{u}^b$, $\mathbf{x}_u^t = \mathbf{x} + a\mathbf{u}^t$, $\mathbf{x}_u^s = \mathbf{x} + a\mathbf{u}^s$ and a is a constant when RMSD of the fibril is 1 nm.

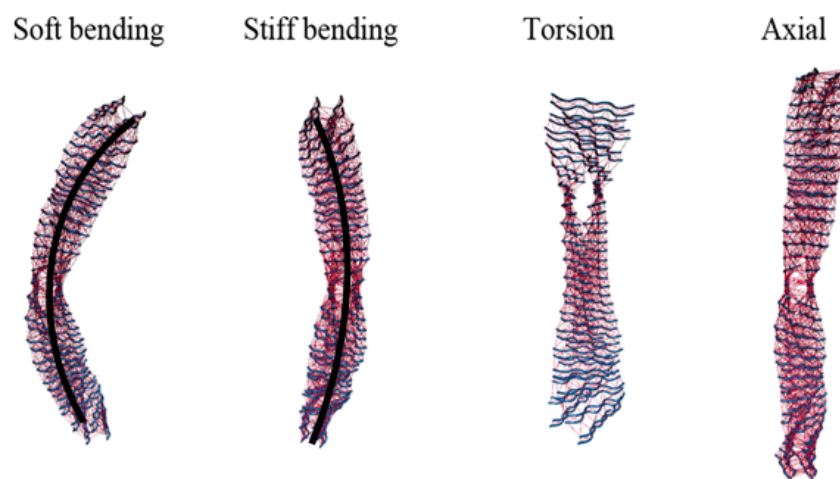
5.3. Results

5.3.1. Vibration Characteristic of Protein Fibrils

Structural properties of hIAPP fibril can be inferred from free vibration modes and the fundamental modes, except six rigid body modes, are dominant for dynamic behavior of fibril. In Fig. 5.2 (a), the four dominant modes are presented such as soft bending, stiff bending, torsion and stretching modes, the reason for double cases of bending mode is rectangular cross-section of fibril. The mode index is the order of natural frequencies of each vibration modes, which means contribution to dynamic behavior of fibril. The bending mode is low frequency motion (Fig. 5.2 (b)) that is slower than other modes, therefore bending mode is dominant deformation mode of fibril. In the contrary, the high frequency

(a)

L=17.045nm



(b)

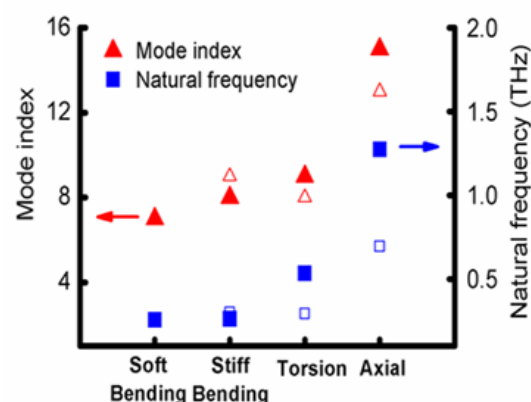


Fig. 5.2. (a) Four fundamental deformation modes of hIAPP fibril when the cross- β structure is antiparallel/hetero and one pitch length. Soft bending, stiff bending, twisting and stretching mode from left. (b) The mode indices (left axis) and natural frequencies (right axis) of the fibril. Figure reproduced with permission from Ref. [181], © 2011 Wiley Periodicals, Inc.

stretching mode has lower contribution than other modes. There are coupled deformation modes among dominant three modes, however it is disregarded for problem simplicity.

5.3.2. Mechanical Properties of Protein Fibrils

The mechanical properties of hIAPP fibril can be obtained by the relation of natural frequency and mechanical property of continuum theory. In the fig. 5.3, the elastic modulus for bending (E), shear modulus (G) and axial elastic modulus (Υ) of the antiparallel hetero fibril is shown varying the fibril length to 280.025 nm. First of all, the E and G of the fibril is few TPa range comparable to the modulus of single-wall carbon nanotube, higher than the experimental value of other kinds of amyloid fibril (about 10~100 GPa) [37]. It can be interpreted that the difference of the geometric information of the fibril used in the experiment and our simulation exists, the moment of inertia of the fibril is obtained by atomic distance in our simulation ($I \approx 10^{-37} \text{ m}^4$) but in the experiment, average height in AFM topography of the fibrils is used ($I \approx 10^{-34} \sim 10^{-36} \text{ m}^4$). It can be confirmed by the bending rigidity (EI) of the fibril, EI in our simulation ($EI \approx 10^{-24} \text{ N m}^2$, see Fig 5.3 (b)) is comparable to the diverse amyloid fibrils' EI in that experiments. The E of stiff bending is highest, the following is Υ , E of soft bending and G is lowest at all fibril length. Also, the mode index of bending is always 7 (soft) and 8 (stiff) at all fibril length, but that of torsion and axial becomes lower when the fibril length increases. (Fig 5.3. (c)) It means that the torsion and axial mode is less important when fibril grows, however, the bending is dominant mode in mechanical behavior of the fibril at all fibril length. The E of soft bending is 0.4 to 0.8 TPa, varying with the fibril length. When the fibril length is shorter than 70 nm, the elastic modulus increases with the fibril length vibration. is increase, converges to 0.8 TPa when the fibril length is longer than 70

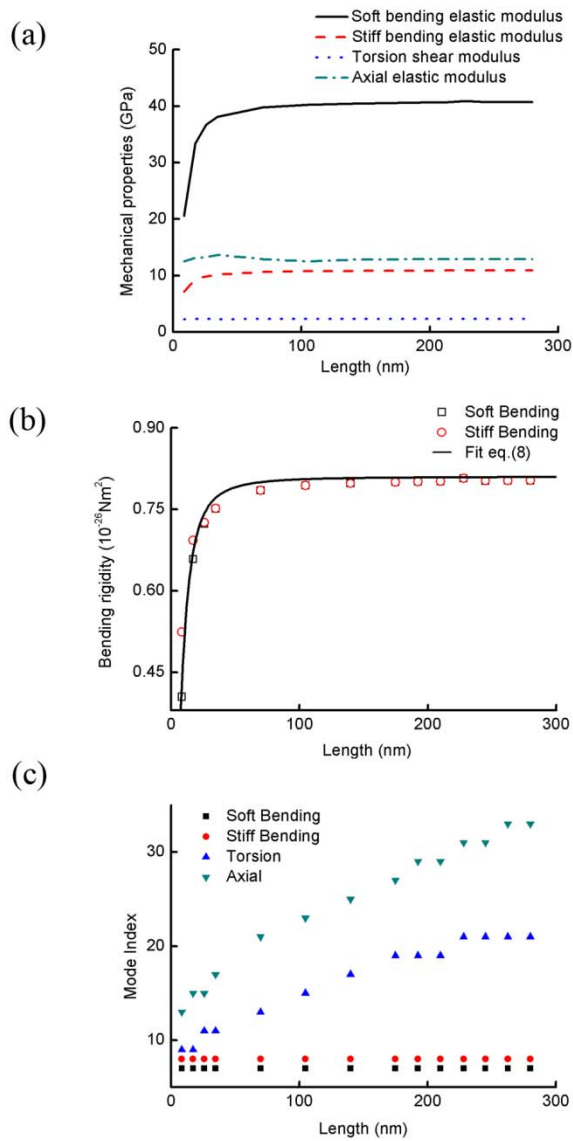


Fig. 5.3. (a) Soft bending elastic modulus, stiff bending elastic modulus, torsional shear modulus and axial elastic modulus of the antiparallel hetero fibril varying fibril length (L) to 280 nm. (b) The bending rigidity of the fibril varying fibril length (L) (c) Mode index of soft bending, stiff bending, torsion and axial. Figure reproduced with permission from Ref. [181], © 2011 Wiley Periodicals, Inc.

Table 5.1. Comparison the elastic modulus among the result from different method. Table reproduced with permission from Ref. [181], © 2011 Wiley Periodicals, Inc.

Method (material)	Bending modulus (GPa)	Torsional modulus (GPa)	Axial stiffness (GPa)
NMA based on ENM (hIAPP) [§]	7~40	2.28~2.34	12.5~13.7
NMA based on ENM (A β ₁₋₄₀) [¶]	10~50	4.3	31.0
MD (A β ₁₋₄₀) [*]	-	-	12.43 (compression) 18.05 (tension)
Experiment (A β ₁₇₋₄₂) ^{**}	11.7	-	-

[§] The result of this simulation. Here, the antiparallel hetero hIAPP fibril is considered.

[¶] Result from Xu *et al.* [39] In this table, two-fold A β amyloid fibril is presented.

^{*} Result from Paparcone *et al.* [182] In this paper, the mechanical propertied of two-fold symmetric A β amyloid fibril is obtained by compression and tensile loading based on molecular dynamic simulation.

^{**} Result from Knowles *et al.* [37]

nm. The reason that elastic modulus vary with the fibril length when the length is short is that the shear deformation is not considered in continuum theory. Especially, the Euler-Bernoulli beam model (or classical beam model) assumes that the beam has high aspect ratio that shear deformation is much smaller than beam deflection, so the shear deformation can be ignored. But when the beam becomes shorter, the effect of shear deformation becomes evident, Timoshenko beam model can be considered. To evaluate the shear effect in the bending deformation of the fibril, simple problem of the bending deflection of beam is proposed. The Eq. 5.9 is well fit to the result of bending rigidity with the fibril length at Fig. 5.3 (b) (solid line), the bending rigidity when shear effect is considered and shear modulus for bending can be obtained to $\bar{EI} = 0.8 \times 10^{-26}$ Nm², $\bar{G} = 1.1$ GPa. Now, the shear effect in the bending of the hIAPP fibril can be calculated by substituting \bar{EI} and \bar{G} to φ_s (shear effect, $\varphi_s = 12a_sEI/(GAL^2)$), when the fibril length is 10 nm, $\varphi_s = 0.583$ and $L = 70$ nm, $\varphi_s = 0.012$ and $L = 300$ nm, $\varphi_s = 0.000647$. Namely, the shear deflection is more than 50% when the fibril length is 10 nm, when the fibril length is above 70 nm, the shear effect reduce less than 1%, the shear effect is almost zero at the full length of the fibril. As a result, the shear effect in the bending deformation is diminished when the fibril grows, when the fibril length is above 70 nm, the shear effect is reduced remarkably.

5.3.3. Bending Vs. Torsion

The twist/bend ratio is bending rigidity divided by torsional rigidity (EI/GJ), that of bacterial flagellar hook and filament is less than 1. [183] The structure that $EI/GJ < 1$ is that bend relatively more easily than they twist. In fig. 5.4, EI/GJ of antiparallel hetero hIAPP fibril is presented, that is more than 1 whether the fibril is long or not. It means that the fibril prefers twist rather than bend like solid

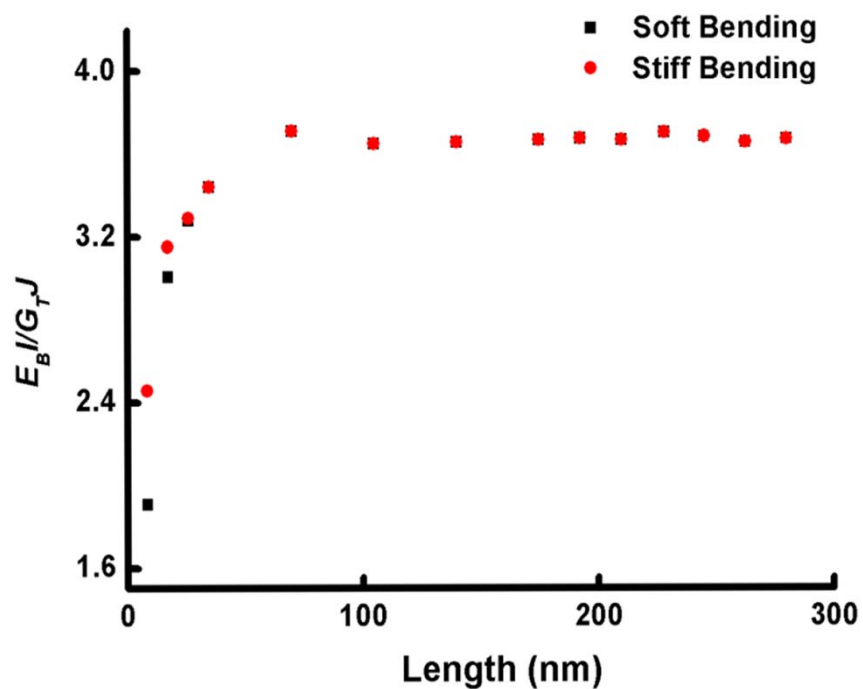


Fig. 5.4. Twist/bend ratio of antiparallel hetero hIAPP fibril about fibril length.
Figure reproduced with permission from Ref. [181], © 2011 Wiley Periodicals,
Inc.

steel circular cylinder which has a value of about 1.3 [184] and that guarantees the stability of the fibril. Because the bending mode is dominant for dynamics of the fibril than twisting mode (see Fig. 6.3. (c), Mode indices of bending are lower than those of twisting.) but the fibril is not flexible for bending mode, the dynamic behaviors of the fibril are disturbed. On the other hand, although the fibril is flexible for twisting mode, twisting mode is less important for dynamic behavior of the fibril, it cannot affect to dynamic behavior of the fibril.

5.3.4. Effect of Polymorphism in Mechanical Properties

In Fig. 5.5, EI , G and Y of possible four kinds of hIAPP fibril are presented for investigation of relationship between cross- β configuration and stability of the fibril. The elastic modulus of all kinds of the fibril increases when the fibril is short and converges when the fibril length is above 70 nm because the shear effect is ignored. The difference of elastic modulus among the 4 kinds of the fibril is about hundreds GPa level, the study of relationship between cross- β configuration and elastic modulus is important. In Fig.5.5 (a) and (b), EI of the antiparallel homo fibril is highest but that of parallel hetero is lowest. In this trend, the antiparallel homo fibril is stiffer than parallel hetero one. Also, Fig.5.5 (c) shows the trend more certainly, G of antiparallel homo fibril is highest and the following is antiparallel hetero, parallel homo and G of parallel hetero one is lowest. Here, the antiparallel fibril is stiffer than parallel one and homo fibril is stiffer than hetero one. Moreover, the antiparallel homo fibril has two kinds of antiparallel cross- β configuration, one is along fibril axis and the other is cross the fibril axis and the parallel hetero fibril has two parallel cross- β configurations along and cross the fibril axis. Namely, the elastic modulus of the fibril consists many antiparallel cross- β configuration is higher than that of parallel cross- β configuration. It is interesting that the spider silk protein consists the antiparallel

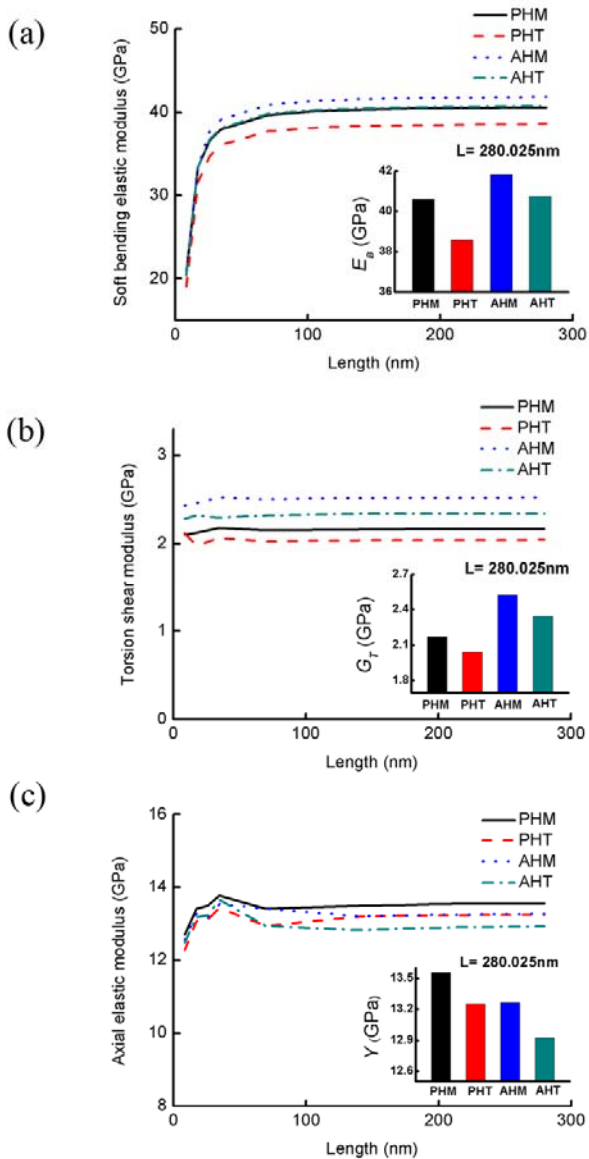


Fig. 5.5. Mechanical properties of four cross- β configuration of the hIAPP fibril varying fibril length. (a) The soft bending elastic modulus (b) The stiff bending elastic modulus (c) The torsional shear modulus (d) The axial elastic modulus. Figure reproduced with permission from Ref. [181], © 2011 Wiley Periodicals, Inc.

cross- β configuration [7], which bears the remarkable mechanical properties such as super-elasticity and high fracture toughness [2,3]. On the other hand, the Young's modulus for stretching mode of four kinds of the fibril has different tendency in Fig. 5(d), it is not considered in this interpretation that stretching mode is less dominant than other bending and twisting mode in the dynamic behavior of the fibril. In this result, it is carefully proposed that cross- β structure may influence the stability of amyloid fibril. The stability of amyloid fibril can be affect to the toxicity of the amyloid in the physiological condition. The toxicity of amyloid fibril can be varied by type of amyloid, cellular environment and so on, related to changes in aggregation properties, and studied to reveal the aggregation mechanism of amyloid. [185]

5.3.5. Geometric Effects on Mechanical Properties: Role of Twisted Structure

The hIAPP fibril is periodically twisted structure along the fibril axis, if the fibril is untwisted, the fibril has anisotropic characteristics for its rectangular cross section area. In Fig 6.6, the EI of the untwisted antiparallel hetero hIAPP fibril along soft ($EI = 0.7 \times 10^{-26} \text{ Nm}^2$) and stiff axis ($EI = 1.1 \times 10^{-26} \text{ Nm}^2$) is highly different at full length of the fibril, it means that the untwisted fibril has two kinds of bending stiffness in direction of height (10.52 Å) and width (20.33 Å) of cross section area. In other words, the fibril is strong at direction of width but weak at direction of height, this weak direction can diminish the mechanical stability of the fibril. On the other side, EI of twisted antiparallel hetero hIAPP fibril along soft and stiff axis is almost same ($EI = 0.8 \times 10^{-26} \text{ Nm}^2$, see Fig 5.3 (b)) at full length of fibril, so the twisted fibril has single bending stiffness. Unlike the untwisted fibril, the twisted one has not weak direction of bending, the mechanical stability of the twisted fibril is better than the untwisted one.

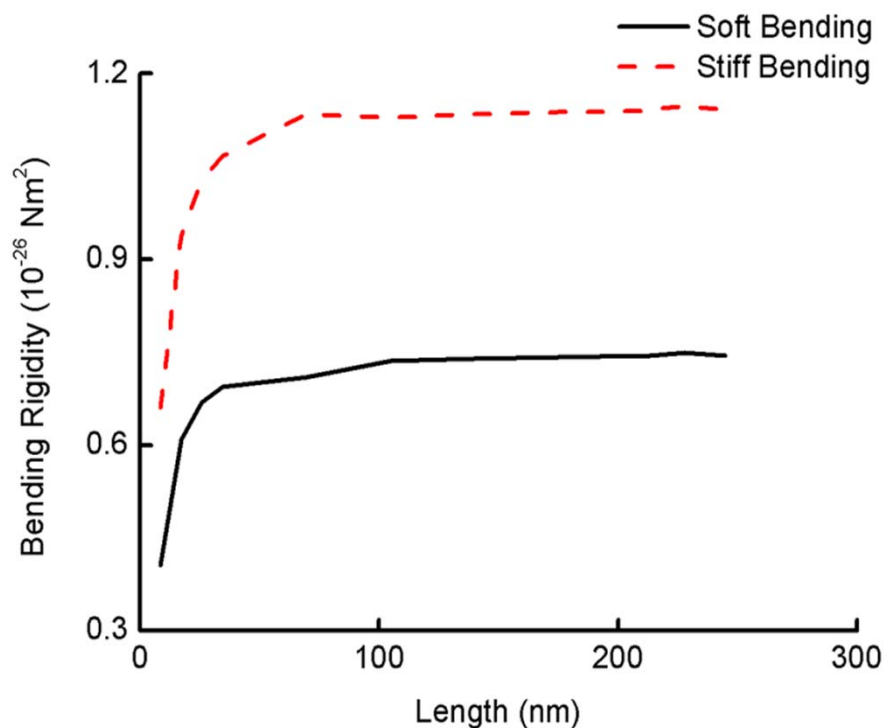


Fig. 5.6. Soft and stiff bending rigidity of untwisted hIAPP fibril (Antiparallel hetero, $L = 17.045 \text{ nm}$) about fibril length. Figure reproduced with permission from Ref. [181], © 2011 Wiley Periodicals, Inc.

5.4. Discussion: Limitation of the Model

The mechanical property differences varying the cross- β structure of hIAPP fibril is studied in the section 5.3.4, where 4 kinds of cross- β structure such as parallel homo, parallel hetero, antiparallel homo, antiparallel hetero are considered. However, there are more possible cross- β structures in the configuration of amyloid fibrils which are classified by correlation with the direction of fibril-axis of front and back β -sheet in the hIAPP fibril. In the Fig. 1.4 (B), 8 kinds of possible cross- β structure are presented. It can be verified that possible cross- β structures considered in this chapter is co-aligned structure, which shows the direction of front and back β -sheets correlate with the fibril axis. The anti-aligned cross- β structures, the direction of front β -sheets correlate with the fibril axis but that of the back β -sheets anti-correlate with the fibril axis, should be contemplated, however the coarse-grained model cannot represent the direction of amyloid fibril. For the improvement of this model in order to capture the anti-aligned cross- β structure, the coarse-grained model has to be appropriately modified by consideration of all atoms (or more refined coarse-grained beads) with chemical bond dependent force constants (e.g., mixed-resolution elastic network model), which may enable to consider the direction of side-chain of the amino acids, and consequently the direction of the β -sheets in amyloid fibrils.

5.5. Summary

In this chapter, the structure-property relationship of the amyloid fibrils is investigated with prediction of possible deformation mode with coarse-grained model. It is studied that the mechanical characteristics of the hIAPP fibril, which depend on the fibril length, cross- β configuration and twisted structure. The NMA with ENM of the possible four cases cross- β structure of the fibril is

performed to find possible deformation mode such as bending, torsion and axial deformation. The continuum theoretical models are applied for obtaining mechanical properties such as bending elastic modulus, torsion shear modulus and axial elastic modulus, the shear effect in the bending of the fibril is discussed with the theory of static deflection of bending.

Chapter 6. Conclusion

This dissertation successfully presented the mechanical characteristics of protein materials for gaining fundamental insights into the structure-property-function relationship of protein materials. In this dissertation, we have provided the underlying mechanisms in the mechanical behavior of biological structures at multiple scales ranging from a single bond (at atomic resolution), a secondary structures (*e.g.* α -helix, and β -sheet), protein domain (at single-molecule resolution), even to protein filament such as amyloid fibrils (at micron length scale). Chapter 1 overviews not only current understanding of the mechanical behavior of protein materials but also the current state-of-arts in mechanical characterization of protein materials using experimental and computational techniques. In Chapter 2, we have described the mechanical behavior of a single chemical bond in response to application of mechanical loads. Moreover, in Chapter 3, we have studied the mechanical behavior of a protein domain in response to mechanical loading. It is shown that the mechanical response of a chemical bond and/or protein domain is critically dependent on the force constant of a loading device. This indicates the importance of loading device in the mechanical characterization of proteins, which has not been well taken into account in the recent single-molecule experiments. Chapter 4 has presented the mesoscopic model of protein crystals for understanding the mechanical properties (*e.g.* elastic modulus and yield strength) of protein materials. It is found that the native topology of a protein crystal determines the mechanical properties of protein materials, which sheds light on the importance of the atomistic structure of proteins in the mechanical behavior of proteins. In Chapter 5, we have studied the mechanical behavior of protein fibrils, particularly

amyloid fibril (at micron length scale), using coarse-grained model. We have found that the mechanical properties of amyloid fibrils are significantly dependent on the molecular architecture (*i.e.* polymorphism) of amyloid fibrils. Furthermore, it is shown that the bending behavior of amyloid fibrils is dependent on their length, and that this length-dependent bending behavior is attributed to shear effect.

This dissertation may be regarded as an effort that has been made to develop the theoretical/computational frameworks that enable the fundamental insights into the structure-property-function relationship of protein materials at multiple length scales. To the best of our knowledge, the mechanical properties of protein materials at multiple length scales have not been well understood yet. Despite this dissertation that describes the mechanical properties of proteins at disparate length scales, it is still remained how the hierarchical structures at multiple length scales are interconnected with the mechanical properties of proteins at each length scale. Our dissertation may provide an insight into how to understand the correlation between atomic interactions at disparate length scales, which determines the mechanical properties of protein materials. We believe that there are still many rooms for researchers to make contribution to the development of theoretical/computational frameworks that endow the fundamental understanding of origin for the remarkable mechanical function of proteins at multiple length scales.

References

- [1] J. M. Gosline, P. A. Guerette, C. S. Ortlepp, K. N. savage. The Mechanical Design of Spider Silk: From Fibroin Sequence to Mechanical Function. *The Journal of Experimental Biology* **202**, 3295–3303, (1999).
- [2] S. Kubik. High-Performance Fibers from Spider Silk13. *Angew. Chem. Int. Ed.* **41**, 2721-2723, (2002).
- [3] N. Becker, E. Oroudjev, S. Mutz, J. P. Cleveland, P. K. Hansma, C. Y. Hayashi, D. E. Makarov, H. G. Hansma. Molecular nanosprings in spider capture-silk threads. *Nat. Mat.* **2**, 278, (2003).
- [4] N. Du, Z. Yang, X. Y. Liu, Y. Li, H. Y. Xu. Structural Origin of the Strain-Hardening of Spider Silk. *Advanced Functional Materials* **21**, 772-778, (2011).
- [5] R. Phillips. *Crystals, Defects and Microstructures : Modeling Across Scales*. (Cambridge University Press, 2001).
- [6] J. T. Carl Branden. *Introduction to Protein Structure*(2nd ed). (Garland Publishing, Inc., 1999).
- [7] S. Keten, Z. Xu, B. Ihle, M. J. Buehler. Nanoconfinement controls stiffness, strength and mechanical toughness of beta-sheet crystals in silk. *Nat. Mater.* **9**, 359, (2010).
- [8] J. Hsin, J. Strümpfer, E. H. Lee, K. Schulten. Molecular Origin of the Hierarchical Elasticity of Titin: Simulation, Experiment, and Theory. *Annual Review of Biophysics* **40**, 187-203, (2011).
- [9] M. A. Geeves, K. C. Holmes. Structure Mechanicsm of Muscle Contraction. *Annu. Rev. Biochem* **68**, 687-728, (1999).
- [10] J. C. Phillips, R. Braun, W. Wang, J. Gumbart, E. Tajkhorshid, E. Villa, C. Chipot, R. D. Skeel, L. Kalé, K. Schulten. Scalable molecular dynamics with NAMD. *J. Comput. Chem.* **26**, 1781-1802, (2005).
- [11] C. Hyeon, J. N. Onuchic. Mechanical control of the directional stepping dynamics of the kinesin motor. *Proc. Natl. Acad. Sci. U.S.A.* **104**, 17382-17387, (2007).

- [12] E. H. Lee, J. Hsin, E. von Castelmur, O. Mayans, K. Schulten. Tertiary and Secondary Structure Elasticity of a Six-Ig Titin Chain. *Biophys. J.* **98**, 1085-1095, (2010).
- [13] M. Rief, M. Gautel, F. Oesterhelt, J. M. Fernandez, H. E. Gaub. Reversible Unfolding of Individual Titin Immunoglobulin Domains by AFM. *Science* **276**, 1109-1112, (1997).
- [14] H. Li, W. A. Linke, A. F. Oberhauser, M. Carrion-Vazquez, J. G. Kerkvliet, H. Lu, P. E. Marszalek, J. M. Fernandez. Reverse engineering of the giant muscle protein titin. *Nature* **418**, 998-1002, (2002).
- [15] S. Lv, D. M. Dudek, Y. Cao, M. M. Balamurali, J. Gosline, H. Li. Designed biomaterials to mimic the mechanical properties of muscles. *Nature* **465**, 69-73, (2010).
- [16] The Inner Life of the Cell. *Bio Visions at Harvard University*, (<http://multimedia.mcb.harvard.edu/>).
- [17] D. T. Mirijanian, G. A. Voth. Unique elastic properties of the spectrin tetramer as revealed by multiscale coarse-grained modeling. *Proc. Natl. Acad. Sci. U.S.A.* **105**, 1204-1208, (2008).
- [18] M. Sotomayor, K. Schulten. Single-Molecule Experiments in Vitro and in Silico. *Science* **316**, 1144-1148, (2007).
- [19] V. Bormuth, V. Varga, J. Howard, E. Schaffer. Protein Friction Limits Diffusive and Directed Movements of Kinesin Motors on Microtubules. *Science* **325**, 870-873, (2009).
- [20] Z. Yang, P. Majek, I. Bahar. Allosteric Transitions of Supramolecular Systems Explored by Network Models: Application to Chaperonin GroEL. *PLoS. Comput. Biol.* **5**, e1000360, (2009).
- [21] R. P. McEver, C. Zhu. Rolling Cell Adhesion. *Annual Review of Cell and Developmental Biology* **26**, (2010).
- [22] J. Christof, M. Gebhardt, M. Rief. Force Signaling in Biology. *Science* **324**, 1278-1280, (2009).
- [23] E. Oroudjev, J. Soares, S. Arcidiacono, J. B. Thompson, S. A. Fossey, H. G. Hansma. Segmented nanofibers of spider dragline silk: Atomic force

- microscopy and single-molecule force spectroscopy. *Proc. Natl. Acad. Sci. U.S.A.* **99**, 6460-6465, (2002).
- [24] Z. Shao, F. Vollrath. Materials: Surprising strength of silkworm silk. *Nature* **418**, 741-741, (2002).
- [25] S.-M. Lee, E. Pippel, U. Gösele, C. Dresbach, Y. Qin, C. V. Chandran, T. Bräuniger, G. Hause, M. Knez. Greatly Increased Toughness of Infiltrated Spider Silk. *Science* **324**, 488-492, (2009).
- [26] R. Silvers, F. Buhr, H. Schwalbe. The Molecular Mechanism of Spider-Silk Formation. *Angew. Chem. Int. Ed.* **49**, 5410-5412, (2010).
- [27] M. Heim, D. Keerl, T. Scheibel. Spider Silk: From Soluble Protein to Extraordinary Fiber. *Angew. Chem. Int. Ed.* **48**, 3584-3596, (2009).
- [28] F. Chiti, C. M. Dobson. Protein Misfolding, Functional Amyloid, and Human Disease. *Annu. Rev. Biochem* **75**, 333, (2006).
- [29] R. Nelson, M. R. Sawaya, M. Balbirnie, A. O. Madsen, C. Riek, R. Grothe, D. Eisenberg. Structure of the cross- β spine of amyloid-like fibrils. *Nature* **435**, 773, (2005).
- [30] G. Merlini, V. Bellotti. Molecular Mechanisms of Amyloidosis. *New Eng. J. Med.* **349**, 583-596, (2003).
- [31] A. K. Paravastu, R. D. Leapman, W.-M. Yau, R. Tycko. Molecular structural basis for polymorphism in Alzheimer's beta-amyloid fibrils. *Proc. Natl. Acad. Sci. U.S.A.* **105**, 18349-18354, (2008).
- [32] J. T. Nielsen, B. Morten, J. Martin D, R. O. Pedersen, P. Jan M, H. Kim L, V. Thomas, S. Troels, D. E. Otzen, N. C. Nielsen. Unique Identification of Supramolecular Structures in Amyloid Fibrils by Solid-State NMR Spectroscopy13. *Angew. Chem. Int. Ed.* **48**, 2118, (2009).
- [33] S. Meehan, Y. Berry, B. Luisi, C. M. Dobson, J. A. Carver, C. E. MacPhee. Amyloid Fibril Formation by Lens Crystallin Proteins and Its Implications for Cataract Formation. *Journal of Biological Chemistry* **279**, 3413-3419, (2004).
- [34] C. Rapezzi, C. C. Quarta, L. Riva, S. Longhi, I. Gallelli, M. Lorenzini, P. Ciliberti, E. Biagini, F. Salvi, A. Branzi. Transthyretin-related amyloidoses

- and the heart: a clinical overview. *Nat Rev Cardiol* **7**, 398-408, (2010).
- [35] M. J. Buehler. Nanomaterials: Strength in numbers. *Nat. Nanotechnol.* **5**, 172-174, (2010).
 - [36] L. Esposito, C. Pedone, L. Vitagliano. Molecular dynamics analyses of cross- β -spine steric zipper models: β -Sheet twisting and aggregation. *Proc. Natl. Acad. Sci. U.S.A.* **103**, 11533-11538, (2006).
 - [37] T. P. Knowles, A. W. Fitzpatrick, S. Meehan, H. R. Mott, M. Vendruscolo, C. M. Dobson, M. E. Welland. Role of Intermolecular Forces in Defining Material Properties of Protein Nanofibrils. *Science* **318**, 1900, (2007).
 - [38] R. Paparcone, M. J. Buehler. Failure of Ab(1-40) amyloid fibrils under tensile loading. *Biomaterials* **32**, 3367-3374, (2011).
 - [39] Z. Xu, R. Paparcone, M. J. Buehler. Alzheimer's A-beta Amyloid Fibrils Feature Size-Dependent Mechanical Properties. *Biophys. J.* **98**, 2053, (2010).
 - [40] J. Adamcik, A. Berquand, R. Mezzenga. Single-step direct measurement of amyloid fibrils stiffness by peak force quantitative nanomechanical atomic force microscopy. *Appl. Phys. Lett.* **98**, 193701, (2011).
 - [41] J. Adamcik, J.-M. Jung, J. Flakowski, P. D. L. Rios, G. Dietler, R. Mezzenga. Understanding amyloid aggregation by statistical analysis of atomic force microscopy images. *Nat. Nanotechnol.* **5**, 423, (2010).
 - [42] T. P. J. Knowles, T. W. Oppenheim, A. K. Buell, D. Y. Chirgadze, M. E. Welland. Nanostructured films from hierarchical self-assembly of amyloidogenic proteins. *Nat. Nanotechnol.* **5**, 204-207, (2010).
 - [43] T. P. J. Knowles, M. J. Buehler. Nanomechanics of functional and pathological amyloid materials. *Nat. Nanotechnol.* **6**, 469-479, (2011).
 - [44] A. Gautieri, S. Vesentini, A. Redaelli, M. J. Buehler. Hierarchical Structure and Nanomechanics of Collagen Microfibrils from the Atomistic Scale Up. *Nano Letters* **11**, 757-766, (2011).
 - [45] H. Li, Y. Cao. Protein Mechanics: From Single Molecules to Functional Biomaterials. *Accounts Chem. Res.* **43**, 1331-1341, (2010).
 - [46] C. Soto. Unfolding the role of protein misfolding in neurodegenerative diseases. *Nat Rev Neurosci* **4**, 49-60, (2003).

- [47] L. M. Luheshi, D. C. Crowther, C. M. Dobson. Protein misfolding and disease: from the test tube to the organism. *Curr. Opin. Chem. Biol.* **12**, 25, (2008).
- [48] A. T. Petkova, Y. Ishii, J. J. Balbach, O. N. Antzutkin, R. D. Leapman, F. Delaglio, R. Tycko. A structural model for Alzheimer's beta-amyloid fibrils based on experimental constraints from solid state NMR. *Proc. Natl. Acad. Sci. U.S.A.* **99**, 16742, (2002).
- [49] M. J. Buehler, Y. C. Yung. Deformation and failure of protein materials in physiologically extreme conditions and disease. *Nat. Mater.* **8**, 175, (2009).
- [50] F. Meersman, R. Q. Cabrera, P. F. McMillan, V. Dmitriev. Structural and Mechanical Properties of TTR105-115 Amyloid Fibrils from Compression Experiments. *Biophys. J.* **100**, 193-197, (2011).
- [51] R. Tycko. Solid-State NMR Studies of Amyloid Fibril Structure. *Annu. Rev. Phys. Chem.* **62**, 279-299, (2011).
- [52] B. H. Toyama, J. S. Weissman. Amyloid Structure: Conformational Diversity and Consequences. *Annu. Rev. Biochem* **80**, 557-585, (2011).
- [53] Y. Miller, B. Ma, R. Nussinov. Polymorphism in Alzheimer Abeta Amyloid Organization Reflects Conformational Selection in a Rugged Energy Landscape. *Chem. Rev.* **110**, 4820, (2010).
- [54] J. E. Straub, D. Thirumalai. Toward a Molecular Theory of Early and Late Events in Monomer to Amyloid Fibril Formation. *Annu. Rev. Phys. Chem.* **62**, 437-463, (2011).
- [55] M. R. Sawaya, S. Sambashivan, R. Nelson, M. I. Ivanova, S. A. Sievers, M. I. Apostol, M. J. Thompson, M. Balbirnie, J. J. W. Wiltzius, H. T. McFarlane, A. O. Madsen, C. Riek, D. Eisenberg. Atomic structures of amyloid cross-beta spines reveal varied steric zippers. *Nature* **447**, 453, (2007).
- [56] R. Paparcone, M. J. Buehler. Microscale structural model of Alzheimer Ab(1-40) amyloid fibril. *Appl. Phys. Lett.* **94**, 243904, (2009).
- [57] J. Madine, E. Jack, P. G. Stockley, S. E. Radford, L. C. Serpell, D. A. Middleton. Structural Insights into the Polymorphism of Amyloid-Like Fibrils Formed by Region 20-29 of Amylin Revealed by Solid-State NMR

- and X-ray Fiber Diffraction. *J. Am. Chem. Soc.* **130**, 14990, (2008).
- [58] J. T. Berryman, S. E. Radford, S. A. Harris. Thermodynamic Description of Polymorphism in Q- and N-Rich Peptide Aggregates Revealed by Atomistic Simulation. *Biophys. J.* **97**, 1, (2009).
- [59] Joshua T. Berryman, Sheena E. Radford, Sarah A. Harris. Systematic Examination of Polymorphism in Amyloid Fibrils by Molecular-Dynamics Simulation. *Biophys. J.* **100**, 2234-2242, (2011).
- [60] S. E. Cross, Y.-S. Jin, J. Rao, J. K. Gimzewski. Nanomechanical analysis of cells from cancer patients. *Nat. Nanotechnol.* **2**, 780-783, (2007).
- [61] S. Suresh. Biomechanics and biophysics of cancer cells. *Acta Biomaterialia* **3**, 413-438, (2007).
- [62] J. G. Lombardino, J. A. Lowe. The role of the medicinal chemist in drug discovery - then and now. *Nat Rev Drug Discov* **3**, 853-862, (2004).
- [63] F. J. Cohen. Macro trends in pharmaceutical innovation. *Nat Rev Drug Discov* **4**, 78-84, (2005).
- [64] G. Kar, O. Keskin, A. Gursoy, R. Nussinov. Allostery and population shift in drug discovery. *Current Opinion in Pharmacology* **10**, 715-722, (2010).
- [65] G. Schneider, U. Fechner. Computer-based de novo design of drug-like molecules. *Nat Rev Drug Discov* **4**, 649-663, (2005).
- [66] T. Mura. *Micromechanics of Defects in Solids*. 2nd edn, (Springer, 1987).
- [67] L. J. Gibson, M. F. Ashby. *Cellular Solids structure and properties*. second edn, (Cambridge University Press, 1997).
- [68] G. Binnig, C. F. Quate, C. Gerber. Atomic Force Microscope. *Phys. Rev. Lett.* **56**, 930, (1986).
- [69] K. C. Neuman, T. Lionnet, J.-F. Allemand. Single-Molecule Micromanipulation Techniques. *Annual Review of Materials Research* **37**, 33-67, (2007).
- [70] D. J. Müller, M. Krieg, D. Alsteens, Y. F. Dufrêne. New frontiers in atomic force microscopy: analyzing interactions from single-molecules to cells. *Current Opinion in Biotechnology* **20**, 4-13, (2009).
- [71] K. Eom, J. Yang, J. Park, G. Yoon, Y. S. Sohn, S. Park, D. S. Yoon, S. Na, T.

- Kwon. Experimental and Computational Characterization of Biological Liquid Crystals: A Review of Single-Molecule Bioassays. *International Journal of Molecular Science* **10**, 4009-4032., (2009).
- [72] D. J. Muller, Y. F. Dufrene. Atomic force microscopy as a multifunctional molecular toolbox in nanobiotechnology. *Nat. Nanotechnol.* **3**, 261-269, (2008).
- [73] T. R. Strick, et al. Stretching of macromolecules and proteins. *Reports on Progress in Physics* **66**, 1, (2003).
- [74] S. Kumar, M. S. Li. Biomolecules under mechanical force. *Physics Reports* **486**, 1-74, (2010).
- [75] P. A. Wiggins, T. van der Heijden, F. Moreno-Herrero, A. Spakowitz, R. Phillips, J. Widom, C. Dekker, P. C. Nelson. High flexibility of DNA on short length scales probed by atomic force microscopy. *Nat. Nanotechnol.* **1**, 137, (2006).
- [76] J. H. Weiner. *Statistical Mechanics of Elasticity (2nd Edition)*. (DOVER PUBLICATIONS, INC. Mineola, NewYork, 2002).
- [77] P. J. Flory. *Principles of Polymer Chemistry*. (Cornell University Press, 1953).
- [78] T. E. Fisher, P. E. Marszalek, J. M. Fernandez. Stretching single molecules into novel conformations using the atomic force microscope. *Nature Structural Biology* **7**, 719, (2000).
- [79] A. Borgia, P. M. Williams, J. Clarke. Single-Molecule Studies of Protein Folding. *Annu. Rev. Biochem* **77**, 101-125, (2008).
- [80] G. Hummer, A. Szabo. Free Energy Surfaces from Single-Molecule Force Spectroscopy. *Accounts Chem. Res* **38**, 504-513, (2005).
- [81] C. Bustamante, J. F. Marko, E. D. Siggia, S. Smith. Entropic Elasticity of lambda-Phage DNA. *Science* **265**, 1599, (1994).
- [82] D. L. Nelson, M. M. Cox. *Lehninger Principles of Biochemistry*. fourth edn, (Freeman, 2005).
- [83] J. M. Fernandez, H. Li. Force-Clamp Spectroscopy Monitors the Folding Trajectory of a Single Protein. *Science* **303**, 1674-1678, (2004).
- [84] E. Evans, K. Ritchie. Dynamic strength of molecular adhesion bonds. *Biophys.*

J. **72**, 1541-1555, (1997).

- [85] G. Hummer, A. Szabo. Kinetics from Nonequilibrium Single-Molecule Pulling Experiments. *Biophys. J.* **85**, 5-15, (2003).
- [86] O. K. Dudko, G. Hummer, A. Szabo. Intrinsic Rates and Activation Free Energies from Single-Molecule Pulling Experiments. *Phys. Rev. Lett.* **96**, 108101, (2006).
- [87] G. I. Bell. Models for the Specific Adhesion of Cells to Cells. *Science* **200**, 618-627, (1978).
- [88] M. J. Buehler, T. Ackbarow. Fracture mechanics of protein materials. *Materials Today* **10**, 46-58, (2007).
- [89] M. Carrion-Vazquez, A. F. Oberhauser, S. B. Fowler, P. E. Marszalek, S. E. Broedel, J. Clarke, J. M. Fernandez. Mechanical and chemical unfolding of a single protein: A comparison. *Proc. Natl. Acad. Sci. U.S.A.* **96**, 3694-3699, (1999).
- [90] P. M. Williams, S. B. Fowler, R. B. Best, J. Luis Toca-Herrera, K. A. Scott, A. Steward, J. Clarke. Hidden complexity in the mechanical properties of titin. *Nature* **422**, 446-449, (2003).
- [91] H. Li, M. Carrion-Vazquez, A. F. Oberhauser, P. E. Marszalek, J. M. Fernandez. Point mutations alter the mechanical stability of immunoglobulin modules. *nature structural biology* **7**, 1117, (2000).
- [92] P. E. Marszalek, H. Lu, H. Li, M. Carrion-Vazquez, A. F. Oberhauser, K. Schulten, J. M. Fernandez. Mechanical unfolding intermediates in titin modules. *Nature* **402**, 100-103, (1999).
- [93] M. Carrion-Vazquez, H. Li, H. Lu, P. E. Marszalek, A. F. Oberhauser, J. M. Fernandez. The mechanical stability of ubiquitin is linkage dependent. *Nat Struct Mol Biol* **10**, 738-743, (2003).
- [94] Y. Suzuki, O. K. Dudko. Biomolecules under mechanical stress: A simple mechanism of complex behavior. *J. Chem. Phys.* **134**, 065102, (2011).
- [95] K. C. Neuman, A. Nagy. Single-molecule force spectroscopy: optical tweezers, magnetic tweezers and atomic force microscopy. *Nat Meth* **5**, 491-505, (2008).

- [96] J. Kim, C.-Z. Zhang, X. Zhang, T. A. Springer. A mechanically stabilized receptor-ligand flex-bond important in the vasculature. *Nature* **466**, 992-995, (2010).
- [97] J. C. M. Gebhardt, T. Bornschlogl, M. Rief. Full distance-resolved folding energy landscape of one single protein molecule. *Proc. Natl. Acad. Sci. U.S.A.* **107**, 2013-2018, (2010).
- [98] J. M. Gere, S. Timoshenko. *Mechanics of Materials*. (Brooks/Cole Engineering Division, 1984).
- [99] J. F. Smith, T. P. J. Knowles, C. M. Dobson, C. E. MacPhee, M. E. Welland. Characterization of the nanoscale properties of individual amyloid fibrils. *Proc. Natl. Acad. Sci. U.S.A.* **103**, 15806, (2006).
- [100] L. Yang, K. O. van der Werf, C. F. C. Fitié, M. L. Bennink, P. J. Dijkstra, J. Feijen. Mechanical Properties of Native and Cross-linked Type I Collagen Fibrils. *Biophys. J.* **94**, 2204-2211, (2008).
- [101] A. Kis, S. Kasas, B. Babic, A. J. Kulik, W. Benoit, G. A. D. Briggs, C. Schonenberger, S. Catsicas, L. Forro. Nanomechanics of Microtubules. *Phys. Rev. Lett.* **89**, 248101, (2002).
- [102] W. H. Roos, R. Bruinsma, G. J. L. Wuite. Physical virology. *Nat. Phys.* **6**, 733, (2010).
- [103] K. L. Johnson. (Cambridge University Press, 1985).
- [104] S. Guo, B. B. Akhremitchev. Packing Density and Structural Heterogeneity of Insulin Amyloid Fibrils Measured by AFM Nanoindentation. *Biomacromolecules* **7**, 1630-1636, (2006).
- [105] P. J. de Pablo, I. A. T. Schaap, F. C. MacKintosh, C. F. Schmidt. Deformation and Collapse of Microtubules on the Nanometer Scale. *Phys. Rev. Lett.* **91**, 098101, (2003).
- [106] K. Eom. *Simulations in Nanobiotechnology* (CRC Press, Boca Raton, 2011).
- [107] B. R. Brooks, R. E. Brucolieri, D. J. Olafson, D. J. States, S. Swaminathan, M. Karplus. CHARMM: A Program for Macromolecular Energy, Minimization, and Dynamics Calculations. *J. Comput. Chem.* **4**, 187-217, (1983).

- [108] J. A. D. MacKerell, D. Bashford, M. Bellott, J. R. L. Dunbrack, J. D. Evanseck, M. J. Field, S. Fischer, J. Gao, H. Guo, S. Ha, D. Joseph-McCarthy, L. Kuchnir, K. Kuczera, F. T. K. Lau, C. Mattos, S. Michnick, T. Ngo, D. T. Nguyen, B. Prodhom, I. W. E. Reiher, B. Roux, M. Schlenkrich, J. C. Smith, R. Stote, J. Straub, M. Watanabe, J. Wiórkiewicz-Kuczera, D. Yin, M. Karplus. All-Atom Empirical Potential for Molecular Modeling and Dynamics Studies of Proteins. *J. Phys. Chem. B* **102**, 3586-3616, (1998).
- [109] P. K. Weiner, P. A. Kollman. AMBER: Assisted model building with energy refinement. A general program for modeling molecules and their interactions. *J. Comput. Chem.* **2**, 287-303, (1981).
- [110] H. Lu, B. Isralewitz, A. Krammer, V. Vogel, K. Schulten. Unfolding of Titin Immunoglobulin Domains by Steered Molecular Dynamics Simulation. *Biophys. J.* **75**, 662-671, (1998).
- [111] B. Brooks, M. Karplus. Harmonic dynamics of proteins: normal modes and fluctuations in bovine pancreatic trypsin inhibitor. *Proc. Natl. Acad. Sci. U.S.A.* **80**, 6571-6575, (1983).
- [112] A. Amadei, A. B. M. Linssen, H. J. C. Berendsen. Essential dynamics of proteins. *Proteins: Struct., Funct., Bioinfo.* **17**, 412-425, (1993).
- [113] D. A. Case. Normal mode analysis of protein dynamics. *Curr. Opin. Struct. Biol.* **4**, 285-290, (1994).
- [114] D. J. Bernard R. Brooks, zcaron, ccaron, M. Karplus. Harmonic analysis of large systems. I. Methodology. *J. Comput. Chem.* **16**, 1522-1542, (1995).
- [115] S. Hayward, N. Go. Collective Variable Description of Native Protein Dynamics. *Annu. Rev. Phys. Chem.* **46**, 223-250, (1995).
- [116] E. M. Puchner, H. E. Gaub. Force and function: probing proteins with AFM-based force spectroscopy. *Curr. Opin. Struct. Biol.* **19**, 605-614, (2009).
- [117] F. Oesterhelt, D. Oesterhelt, M. Pfeiffer, A. Engel, H. E. Gaub, D. J. Müller. Unfolding Pathways of Individual Bacteriorhodopsins. *Science* **288**, 143-146, (2000).
- [118] C. Bustamante, Z. Bryant, S. B. Smith. Ten years of tension: single-molecule DNA mechanics. *Nature* **421**, 423-427, (2003).

- [119] J. Liphardt, S. Dumont, S. B. Smith, I. Tinoco, Jr., C. Bustamante. Equilibrium Information from Nonequilibrium Measurements in an Experimental Test of Jarzynski's Equality. *Science* **296**, 1832-1835, (2002).
- [120] C. Cecconi, E. A. Shank, C. Bustamante, S. Marqusee. Direct Observation of the Three-State Folding of a Single Protein Molecule. *Science* **309**, 2057-2060, (2005).
- [121] K. Eom, D. E. Makarov, G. J. Rodin. Theoretical studies of the kinetics of mechanical unfolding of cross-linked polymer chains and their implications for single-molecule pulling experiments. *Phys. Rev. E* **71**, 021904, (2005).
- [122] E. Evans. Probing the relation between force-life time and chemistry in single molecular bonds. *Annu. Rev. Biophys. Biom.* **30**, 105-128, (2001).
- [123] H. Changbong, D. Thirumalai. Measuring the energy landscape roughness and the transition state location of biomolecules using single molecule mechanical unfolding experiments. *Journal of Physics: Condensed Matter* **19**, 113101, (2007).
- [124] H.A.Kramers. Brownian motion in a field of force and the diffusion model of chemical reactions. *Physica* **7**, 284, (1940).
- [125] O. K. Dudko, A. E. Filippov, J. Klafter, M. Urbakh. Beyond the conventional description of dynamic force spectroscopy of adhesion bonds. *Proc. Natl. Acad. Sci. U.S.A.* **100**, 11378-11381, (2003).
- [126] A. Garg. Escape-field distribution for escape from a metastable potential well subject to a steadily increasing bias field. *Phys. Rev. B* **51**, 15592, (1995).
- [127] C. Jarzynski. Nonequilibrium Equality for Free Energy Differences. *Phys. Rev. Lett.* **78**, 2690, (1997).
- [128] G. E. Crooks. Entropy production fluctuation theorem and the nonequilibrium work relation for free energy differences. *Phys. Rev. E* **60**, 2721, (1999).
- [129] D. Collin, F. Ritort, C. Jarzynski, S. B. Smith, I. Tinoco, C. Bustamante. Verification of the Crooks fluctuation theorem and recovery of RNA

- folding free energies. *Nature* **437**, 231-234, (2005).
- [130] A. Maitra, G. Arya. Model Accounting for the Effects of Pulling-Device Stiffness in the Analyses of Single-Molecule Force Measurements. *Phys. Rev. Lett.* **104**, 108301, (2010).
 - [131] W. F. Raymond. Unified Model of Dynamic Forced Barrier Crossing in Single Molecules. *Phys. Rev. Lett.* **100**, 138302, (2008).
 - [132] P. Hinterdorfer, Y. F. Dufrene. Detection and localization of single molecular recognition events using atomic force microscopy. *Nat Meth* **3**, 347-355, (2006).
 - [133] R. W. Friddle, P. Podsiadlo, A. B. Artyukhin, A. Noy. Near-Equilibrium Chemical Force Microscopy. *J. Phys. Chem. C* **112**, 4986-4990, (2008).
 - [134] L. B. Freund. Characterizing the resistance generated by a molecular bond as it is forcibly separated. *Proc. Natl. Acad. Sci. U.S.A.* **106**, 8818-8823, (2009).
 - [135] Z. Tshiprut, J. Klafter, M. Urbakh. Single-Molecule Pulling Experiments: When the Stiffness of the Pulling Device Matters. *Biophys. J.* **95**, L42-44, (2008).
 - [136] E. B. Walton, S. Lee, K. J. Van Vliet. Extending Bell's Model: How Force Transducer Stiffness Alters Measured Unbinding Forces and Kinetics of Molecular Complexes. *Biophys. J.* **94**, 2621-2630, (2008).
 - [137] G. Hummer, A. Szabo. Kinetics from Nonequilibrium Single-Molecule Pulling Experiments. *Biophys. J.* **85**, 5-15, (2003).
 - [138] D. B. Staple, S. H. Payne, A. L. C. Reddin, H. J. Kreuzer. Model for Stretching and Unfolding the Giant Multidomain Muscle Protein Using Single-Molecule Force Spectroscopy. *Phys. Rev. Lett.* **101**, 248301, (2008).
 - [139] H. A. Kramers. Brownian motion in a field of force and the diffusion model of chemical reactions. *Physica* **7**, 284, (1940).
 - [140] G. I. Bell. Models for the specific adhesion of cells to cell. *Science* **200**, 618-627, (1978).
 - [141] O. K. Dudko, A. E. Filippov, J. Klafter, M. Urbakh. Beyond the conventional description of dynamic force spectroscopy of adhesion bonds. *Proc. Natl.*

Acad. Sci. USA. **100**, 11378-11381, (2003).

- [142] R. W. Friddle. Unified Model of Dynamic Forced Barrier Crossing in Single Molecules. *Phys. Rev. Lett.* **100**, 138302, (2008).
- [143] H.-J. Lin, Y.-J. Sheng, H.-Y. Chen, H.-K. Tsao. Influences of Linkage Stiffness on Rupture Rate in Single-Molecule Pulling Experiments. *J. Phys. Chem. B* **111**, 6493-6500, (2007).
- [144] T. Dauxois, M. Peyrard. Entropy-driven transition in a one-dimensional system. *Phys. Rev. E* **51**, 4027, (1995).
- [145] R. Merkel, P. Nassoy, A. Leung, K. Ritchie, E. Evans. Energy landscapes of receptor-ligand bonds explored with dynamic force spectroscopy. *Nature* **397**, 50-53, (1999).
- [146] Y. Zhang, G. Sun, L. Shouqin, N. Li, M. Long. Low Spring Constant Regulates P-Selectin-PSGL-1 Bond Rupture. *Biophys. J.* **95**, 5439-5448, (2008).
- [147] A. M. Weissman. Themes and variations on ubiquitylation. *Nat Rev Mol Cell Biol* **2**, 169-178, (2001).
- [148] C.-L. Chyan, F.-C. Lin, H. Peng, J.-M. Yuan, C.-H. Chang, S.-H. Lin, G. Yang. Reversible Mechanical Unfolding of Single Ubiquitin Molecules. *Biophys. J.* **87**, 3995-4006, (2004).
- [149] M. Cieplak, P. E. Marszalek. Mechanical unfolding of ubiquitin molecules. *J. Chem. Phys.* **123**, 194903, (2005).
- [150] A. Irback, S. Mitternacht, S. Mohanty. Dissecting the mechanical unfolding of ubiquitin. *Proc. Natl. Acad. Sci. U.S.A.* **102**, 13427-13432, (2005).
- [151] M. S. Li, M. Kouza, C.-K. Hu. Refolding upon Force Quench and Pathways of Mechanical and Thermal Unfolding of Ubiquitin. *Biophys. J.* **92**, 547-561, (2007).
- [152] A. Imparato, A. Pelizzola. Mechanical Unfolding and Refolding Pathways of Ubiquitin. *Phys. Rev. Lett.* **100**, 158104-158104, (2008).
- [153] P. Szymczak, H. Janovjak. Periodic Forces Trigger a Complex Mechanical Response in Ubiquitin. *J. Mol. Biol.* **390**, 443-456, (2009).
- [154] D. L. Pincus, D. Thirumalai. Crowding Effects on the Mechanical Stability

- and Unfolding Pathways of Ubiquitin. *J. Phys. Chem. B* **113**, 359-368, (2009).
- [155] J. Li, J. M. Fernandez, B. J. Berne. Water's role in the force-induced unfolding of ubiquitin. *Proc. Natl. Acad. Sci. U.S.A.* **107**, 19284-19289, (2010).
- [156] Marek Cieplak, T. X. Hoang, M. O. Robbins. Thermal folding and mechanical unfolding pathways of protein secondary structures. *PROTEINS: Structure, Function, and Genetics* **49**, 104-113, (2002).
- [157] G. Yoon, H.-J. Park, S. Na, K. Eom. Mesoscopic model for mechanical characterization of biological protein materials. *J. Comput. Chem.* **30**, 873, (2009).
- [158] P. A. K. Scott J. Weiner, David A. Case, U. Chandra Singh, Caterina Ghio, Giuliano Alagona, Salvatore Profeta, and Paul Weiner. A new force field for molecular mechanical simulation of nucleic acids and proteins. *J. Am. Chem. Soc.* **106**, 765 - 784, (1984).
- [159] K. Eom, P.-C. Li, D. E. Makarov, G. J. Rodin. Relationship between the Mechanical Properties and Topology of Cross-Linked Polymer Molecules: Parallel Strands Maximize the Strength of Model Polymers and Protein Domains. *J. Phys. Chem. B* **107**, 8730, (2003).
- [160] T. Ackbarow, X. Chen, S. Keten, M. J. Buehler. From the Cover: Hierarchies, multiple energy barriers, and robustness govern the fracture mechanics of {alpha}-helical and beta-sheet protein domains. *Proc. Natl. Acad. Sci. U.S.A.* **104**, 16410-16415, (2007).
- [161] M. J. Buehler. Mechanics of Protein Crystals: Atomistic Modeling of elasticity and Fracture. *J. Comput. Theor. Nanos.* **3**, 670-683, (2006).
- [162] M. J. Buehler. Large-Scale Hierarchical Molecular Modeling of Nanostructured Biological Materials *J. Comput. Theor. Nanos.* **3**, 603-623, (2006).
- [163] E. M. Dmitrii, K. H. Paul, M. Horia. Kinetic Monte Carlo simulation of titin unfolding. *J. Chem. Phys.* **114**, 9663-9673, (2001).
- [164] M. Zhou. A new look at the atomic level virial stress: on continuum-molecular system equivalence. *proceedings of royal society of london A* **459**,

- 2347, (2003).
- [165] S. P. G. Timoshenko, J. N. *Theory of elasticity.* (McGraw-Hill, 1970).
 - [166] L. D. Landau, E. M. Lifshitz. *Theory of Elasticity.* 2 edn, Vol. 7 (Pergamon press, 1975).
 - [167] O. Wagner, J. Zinke, P. Dancker, W. Grill, J. Bereiter-Hahn. Viscoelastic Properties of f-actin, Microtubules, f-actin/alpha -actinin, and f-actin/Hexokinase Determined in Microliter Volumes with a Novel Nondestructive Method. *Biophys. J.* **76**, 2784-2796, (1999).
 - [168] K. W. Plaxco, K. T. Simons, D. Baker. Contact order, transition state placement and the refolding rates of single domain proteins. *J. Mol. Biol.* **277**, 985, (1998).
 - [169] A. Clark, J. Moffitt. in *Protein Misfolding, Aggregation, and Conformational Diseases* Vol. 6 *Protein Reviews* (eds Vladimir N. Uversky & Anthony L. Fink) 199-216 (Springer US, 2007).
 - [170] N. L. Fawzi, E.-H. Yap, Y. Okabe, K. L. Kohlstedt, S. P. Brown, T. Head-Gordon. Contrasting Disease and Nondisease Protein Aggregation by Molecular Simulation. *Accounts Chem. Res.* **41**, 1037-1047, (2008).
 - [171] T. R. Jahn, O. S. Makin, K. L. Morris, K. E. Marshall, P. Tian, P. Sikorski, L. C. Serpell. The Common Architecture of Cross-beta Amyloid. *J. Mol. Biol.* **395**, 717, (2010).
 - [172] E. M. Puchner, A. Alexandrovich, A. L. Kho, U. Hensen, L. V. Schafer, B. Brandmeier, F. Grater, H. Grubmuller, H. E. Gaub, M. Gautel. Mechanoenzymatics of titin kinase. *Proc. Natl. Acad. Sci. U.S.A.* **105**, 13385-13390, (2008).
 - [173] A. del Rio, R. Perez-Jimenez, R. Liu, P. Roca-Cusachs, J. M. Fernandez, M. P. Sheetz. Stretching Single Talin Rod Molecules Activates Vinculin Binding. *Science* **323**, 638-641, (2009).
 - [174] M. Sotomayor, K. Schulten. The Allosteric Role of the Ca²⁺ Switch in Adhesion and Elasticity of C-Cadherin. *Biophys. J.* **94**, 4621-4633, (2008).
 - [175] J. Golji, R. Collins, M. R. K. Mofrad. Molecular Mechanics of the α -Actinin Rod Domain: Bending, Torsional, and Extensional Behavior. *PLoS.*

Comput. Biol. **5**, e1000389, (2009).

- [176] M. M. Tirion. Large Amplitude Elastic Motions in Proteins from a Single-Parameter, Atomic Analysis. *Phys. Rev. Lett.* **77**, 1905, (1996).
- [177] T. Haliloglu, I. Bahar, B. Erman. Gaussian Dynamics of Folded Proteins. *Phys. Rev. Lett.* **79**, 3090, (1997).
- [178] K. Eom, S.-C. Baek, J.-H. Ahn, S. Na. Coarse-graining of protein structures for the normal mode studies. *J. Comput. Chem.* **28**, 1400, (2007).
- [179] M. A. Deriu, M. Soncini, M. Orsi, M. Patel, J. W. Essex, F. M. Montevercchi, A. Redaelli. Anisotropic Elastic Network Modeling of Entire Microtubules. *Biophys. J.* **99**, 2190, (2010).
- [180] L. Meirovitch. *Fundamentals of Vibrations*. (Mc Graw Hill, 2001).
- [181] G. Yoon, J. Kwak, J. I. Kim, S. Na, K. Eom. Mechanical Characterization of Amyloid Fibrils Using Coarse-Grained Normal Mode Analysis. *Advanced Functional Materials* **21**, 3454-3463, (2011).
- [182] R. Paparcone, S. Keten, M. J. Buehler. Atomistic simulation of nanomechanical properties of Alzheimer's A[β](1-40) amyloid fibrils under compressive and tensile loading. *J. Biomech.* **43**, 1196, (2010).
- [183] T. C. Flynn, J. Ma. Theoretical Analysis of Twist/Bend Ratio and Mechanical Moduli of Bacterial Flagellar Hook and Filament. *Biophys. J.* **86**, 3204, (2004).
- [184] S. Vogel. Twist-to-Bend Ratios and Cross-Sectional Shapes of Petioles and Stems. *J. Exp. Bot.* **43**, 1527, (1992).
- [185] K. Berthelot, F. Immel, J. Gean, S. Lecomte, R. Oda, B. Kauffmann, C. Cullin. Driving amyloid toxicity in a yeast model by structural changes: a molecular approach. *FASEB J.* **23**, 2254-2263, (2009).